A DESCRIPTION OF THE SEASONALITY AND ITS VARIABILITY IN A NUMERICAL OCEAN MODEL OF THE SOUTHERN BENGUELA REGION

Presented by Selwyn Bergman

2004

Supervised by: Professor Frank Shillington
Doctor Claude Roy

A dissertation submitted in fulfilment of the requirements for the degree of Master of Science in Physical Oceanography at the University of Cape Town

University of Cape Town
Department of Oceanography

Abstract

The Southern Benguela has, for various reasons, been a focal point for research particularly during recent years. One of the most notable reasons for this interest can be found in the presence of economically viable fish species and their relationship to the process of upwelling.

A numerical model of the entire Southern Benguela Region has previously been set up in order to assist further studies in the region. This dissertation presents the use of the model in an investigation on the seasonality and the interannual variability in temperature, salinity and general circulation in the region.

Hovmuller Plots of the climatology and the associated anomalies were calculated in order to determine the characteristics of the seasonal cycle. It also became possible to deduce a vertical structure of upwelling.

The results give a good view of the seasonal patterns observed in the temperature, salinity and also the overall circulation at the surface and at 200m below the surface from modelled data. A circulation pattern for the summer and winter seasons is presented for the surface and 200m deep layer.

Acknowledgements

This work would not have been made possible without the valuable assistance of a large number of people and organisations. I would like to express my utmost gratitude towards them for their assistance they have rendered. They are: Frank Shillington, Claude Roy, Pierrick Penven, Bruno Blanke and Eric Machu for their tuition throughout the phases of this work; The NRF, the IRD and the VIBES project for providing the necessary funding, hardware, software and the numerical model used in the study; and Thales Geosolutions for its assistance in printing the final document.

Their unselfish assistance has been noted, and I will always remember and respect is as such.

Table of Contents

List of Figures

List of Tables

1 INTRODUCTION

The Benguela Region, which forms the area off the western coast of southern Africa, is a vital reservoir of living marine resources. It forms part of only a handful of areas that, although only occupying 0.1% of the total sea surface, provide ~30% of the total marine fish catch (Durand et al, 1998).

An understanding of the many aspects of this region has significantly gained momentum during recent years, which in turn paved the way for new and innovative methods of analysis. This dissertation adds to this by making use of a previously configured numerical ocean model.

In the following section an overall description of the topography, atmospheric forcing, and waters of the area is given and objectives that will enhance our understanding of the region, are identified. Certain aspects of the literature review are not directly related to the study, but are nonetheless provided for the sake of completeness. It is followed by a description of the overall configuration of the numerical model and of the method that the model output was used to accomplish the objectives. The results of the data processing are then presented, and discussed separately in a subsequent section.

2 THE BENGUELA REGION

2.1 TOPOGRAPHY

2.1.1 OVERALL NATURE OF THE CONTINENTAL MARGIN OFF SOUTH WESTERN AFRICA.

Though the true nature of the Continental Margin varies extensively throughout the Benguela Region, its general nature follows a distinct pattern and thus allows it to be categorized.
Birch et al (1973) categorized the Continental Margin into 3 zones as follows (see Figure 1):

1. An essentially sediment-free rocky platform, called the Nearshore Platform
2. a gently sloping shelf of latitudinally-varying width, termed the "Continental Shelf" which can be between 56km – 240km in width, and
3. the Continental Slope, which is characterised by a steeper seaward gradient than the Continental Shelf.

The rapid change in gradient between the Continental Shelf and the Continental Slope is called the Shelf Break, and occurs in depths ranging from 140m – 400m.

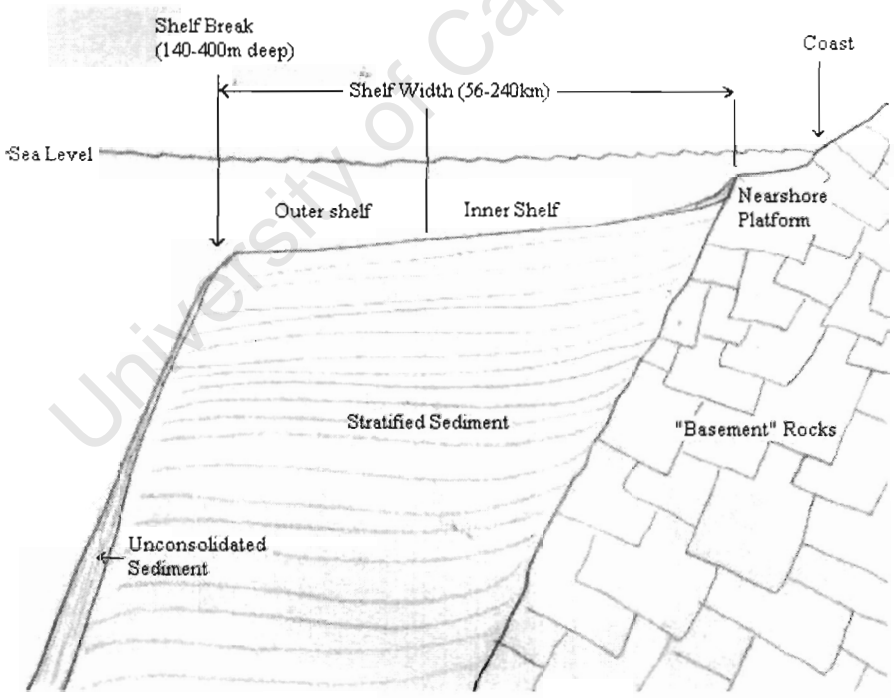

Figure 1: *Idealised shelf-slope profile* [*]

[*] From BIRCH G *et al.* (1973) *S.Afr Shipping News and Fishing Industry Review*, A. Thomson Publication

In addition to this general description double Shelf Breaks are frequently found off the west coast (Siesser et al., 1974). An inner shelf break (~140m deep) and an outer shelf break (~400m deep) have been identified at Walvis Bay (23°S). Further south, at Cape Columbine (33°S), an inner shelf break (between 200-380m deep) and an outer shelf break (~500m deep) which merge south of 33°S to form a single deep shelf break has been identified (Shannon, 1985).

2.1.2 MACROSCALE TOPOGRAPHICAL FEATURES OF THE BENGUELA SYSTEM

The Continental Shelf, defined roughly by the 200m isobath, varies in width from 10km at prominent capes to 150km near Port Nolloth. North of Luderitz the shelf is quite regular and tapers gradually from 90km at Walvis Bay to 40km at Cape Frio. South of Luderitz, at the mouth of the Orange River, a sedimentary cone broadens the shelf to its broadest point (~150km). South of this cone lies the Child's Bank, which rises to a depth of 193m.
The Cape and Angola Basins, which comprise the abyssal plain in the Southeast Atlantic Ocean, are separated by the Walvis Ridge. This ridge runs in a southwesterly direction from the Continental Shelf at ~20°S, for about 2500km towards the Atlantic Central Ridge. It forms a barrier to the flow of water below 3000m. Leakage of Antarctic Bottom Water, does however occur through a gap in this ridge at about 7.5°E.

The Cape Basin, which lies south of the Walvis Ridge, is bound by the Agulhas Ridge on its southern edge. This ridge runs from the Agulhas Plateau in a direction parallel to the Walvis Ridge. Prominent features of the Cape Basin are the numerous volcanic seamounts of which the Discovery and Vema are two well-known examples. Several submarine canyons cut into the shelf, of which the most prominent is the Cape Canyon, that runs in a southwesterly direction from ~60km west of Cape Columbine.
Figure 2 illustrates the major topographical features found in the Southern Benguela Region, as described above.

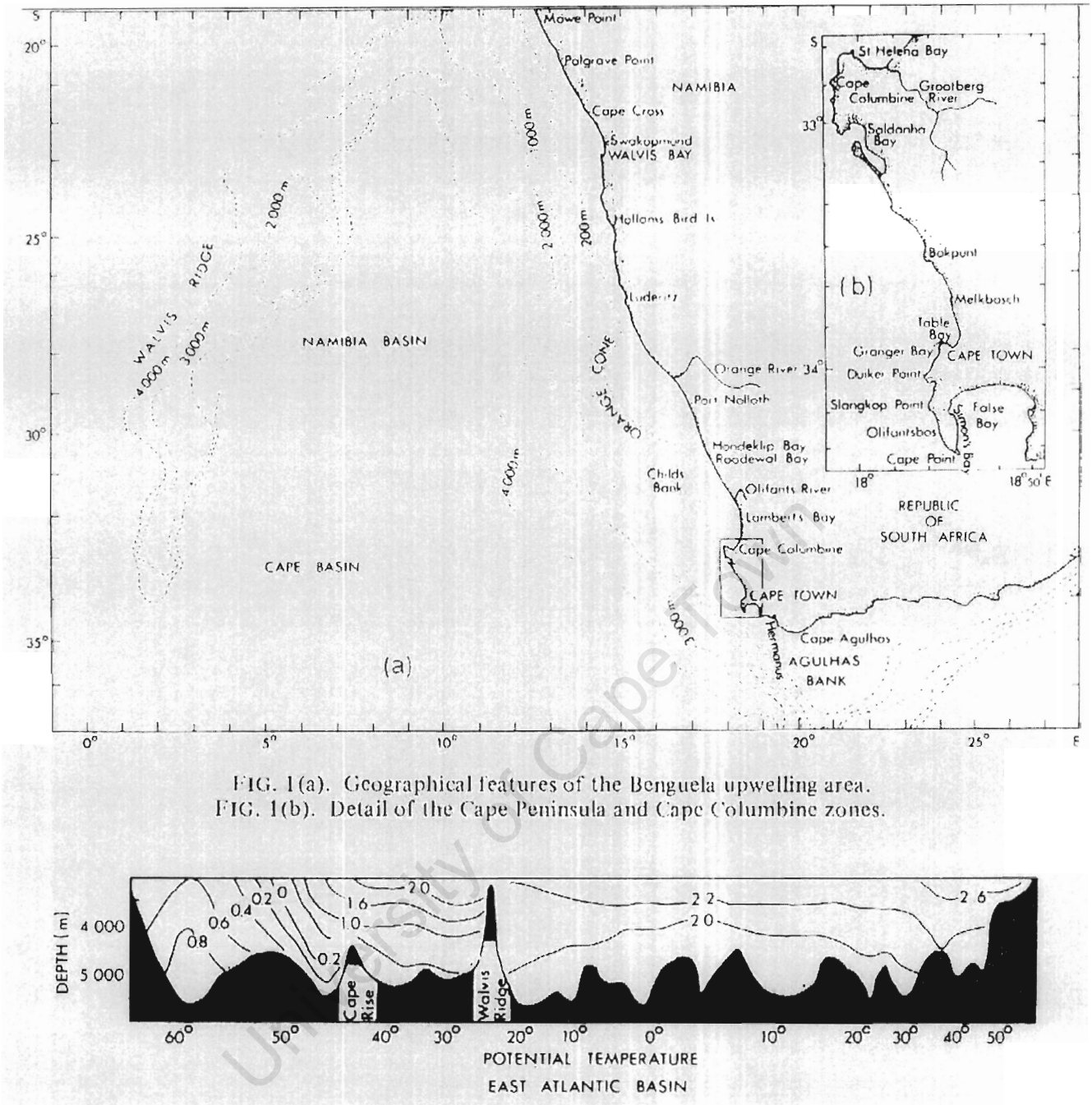

FIG. 1(a). Geographical features of the Benguela upwelling area.
FIG. 1(b). Detail of the Cape Peninsula and Cape Columbine zones.

Figure 2: *Macroscale topographical features of the Benguela Region.* [*]

[*] Taken from NELSON and HUTCHINGS (1983) *Progress in Oceanography.* Pergamon Press

2.2 ATMOSPHERIC FORCING IN THE BENGUELA AREA

Winds in the Benguela area are primarily driven by three dominant phenomena. These are:

1. The South Atlantic High Pressure System,
2. the seasonal low pressure field over the subcontinent, and
3. eastward-moving cyclones south of the subcontinent (Shannon and Nelson, 1996).

The numerical model used in this study if forced by seasonally averaged wind fields. Thus a review of the longer-term atmospheric phenomena important to the area is needed.

2.2.1 THE SOUTH ATLANTIC HIGH PRESSURE SYSTEM

The South Atlantic High Pressure System forms part of a discontinuous belt of high pressure systems that encircle the subtropical hemisphere. This system is maintained throughout the year though its intensity and position varies seasonally. The latitudinal variation is on the order of 6°, reaching a northward extremity in May and a southern extremity in February. The longitudinal variation is on the order of 13° with a westward extremity being reached in August. The pressure variation is on the order of 3 - 4mb (Tyson 1996).

2.2.2 THE SEASONAL LOW PRESSURE FIELD OVER THE SUBCONTINENT

Over the continent, seasonality in the pressure gradients is set up as a result of the latitudinal shifting of the Inter Tropical Convergence Zone (ITCZ) and the Continental Heat Low. The atmospheric pressures over the continent change from well-developed lows during summer, to weak highs during the winter months. A relatively strong interior thermal barrier, set up by desert-like conditions over the coastal plain, steers the curved anticyclonic flow associated with the South Atlantic High, along the West Coast (Nelson and Hutchings 1983).

2.2.3 WIND STRESS AND WIND STRESS CURL

Bakun and Nelson (1991) also considered seasonal fluctuations in the wind stress as well as the wind stress curl. The results of this study are highlighted in Figure 3.

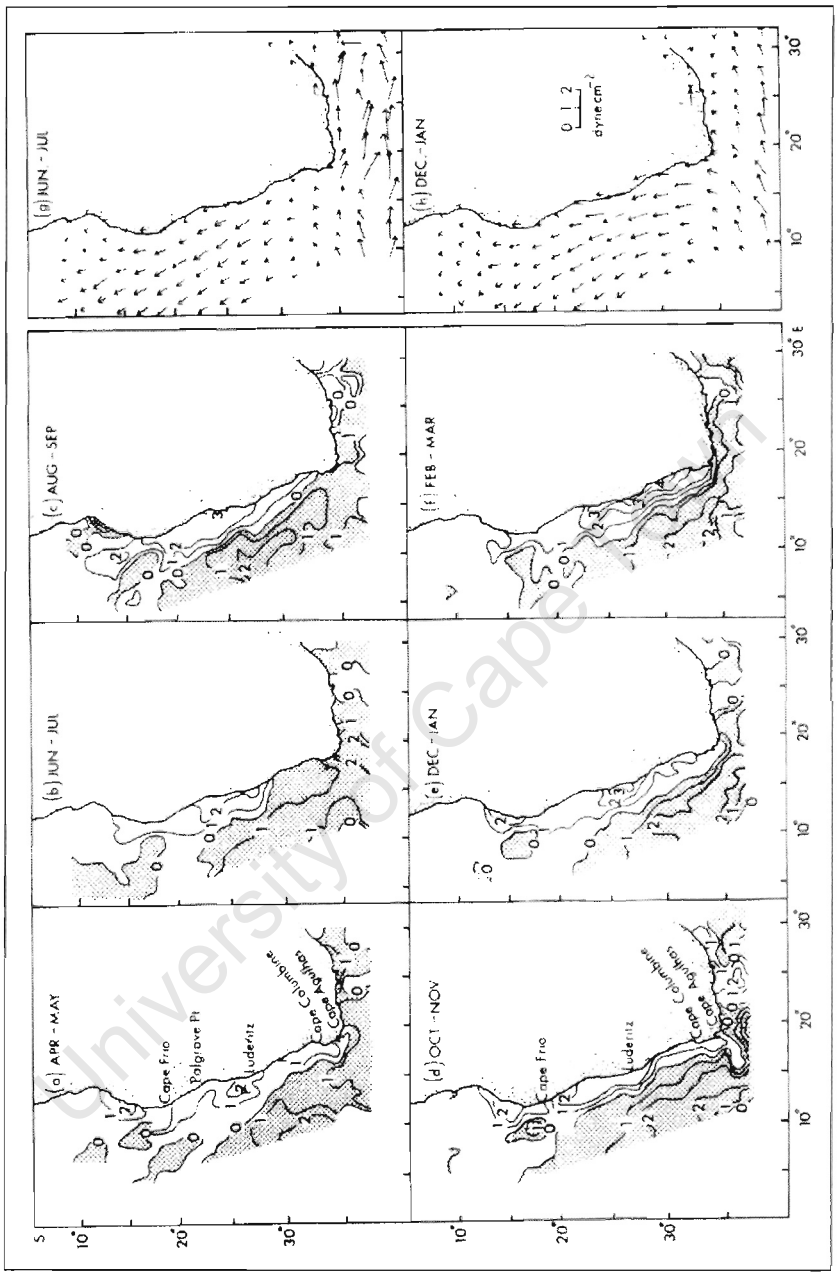

Figure 3: *Wind-stress curl (10^{-8} dyn.cm^{-3}) in the Benguela region (a-f) and surface winds (g-h) (modified from Bakun and Nelson 1991). Regions of anticyclonic wind-stress curl are shaded.*[1]

[1] From Shannon and Nelson, 1996.

They found that the area of strongest longshore wind lies just south of 25°S. This coincides with the approximate latitude of the coastal wedge-shaped area of strongest wind stress curl. This wedge is about 200km wide and can be found at its northern extremity in June, while in late spring and then again in early autumn, extends past Cape Columbine and around the Cape Peninsula. Other locations of cyclonic wind stress are north of Cape Frio (~15°S) during April-May, and October-January and at the South Coast (~25°S) throughout the year.

These locations mark the approximate boundaries of the Benguela Upwelling System.
Offshore, the regions are influenced by anticyclonic wind stress curl as a result of the South Atlantic High Pressure System. South of Africa, perennial westerly zonal winds occur with a seasonal fluctuation that reaches a maximum in the austral winter and a minimum in summer. Along the West Coast, the winds are consistent and aligned in the longshore direction during summer, while they are weaker and more variable in winter.
Boyd (1987) investigated the longshore and seasonal differences in wind stress. These results are summarised by Figure 4.

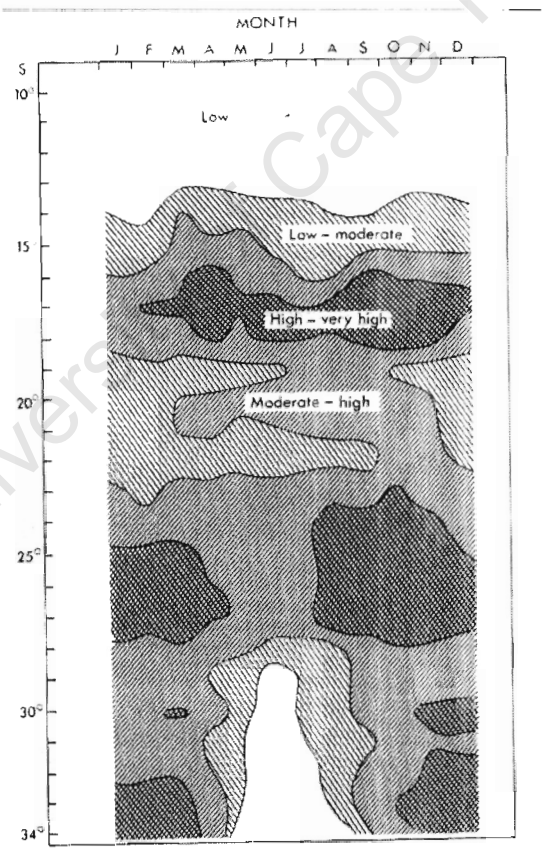

Figure 4: *Monthly Wind stress along the West Coast. This image is centred 40nm offshore after Boyd (1987). Shading (dyn.cm^{-2}): Low <0.2; low-moderate 0.2 – 0.4; moderate – high 0.4 – 0.8; high-very high >0.8*

The major centre for upwelling favourable winds lies near Luderitz (27°S) and a secondary centre occurs near Cape Frio (18°S). Both of these centres occur just to the south of a coastal cyclonic wind stress curl maxima.

2.3 WATER MASSES AND CIRCULATION

Shannon (1985) and Chapman & Shannon (1985) reviewed the main characteristics of the water masses found in the Benguela Region. This section highlights some aspects of those articles and provides a description of the water masses that can be expected through the water column.

The water column in the Benguela Region is comprised of numerous water masses. These include Tropical waters, Subtropical Waters, Thermocline Waters, Antarctic Intermediate Water, North Atlantic Deep Water and Antarctic Bottom Water. The Thermocline Waters are in turn comprised of South Atlantic Central Water, South Indian Central Water and Tropical Atlantic Water. The most dominant water masses and the core characteristics are shown in the θS diagram labelled as Figure 5.

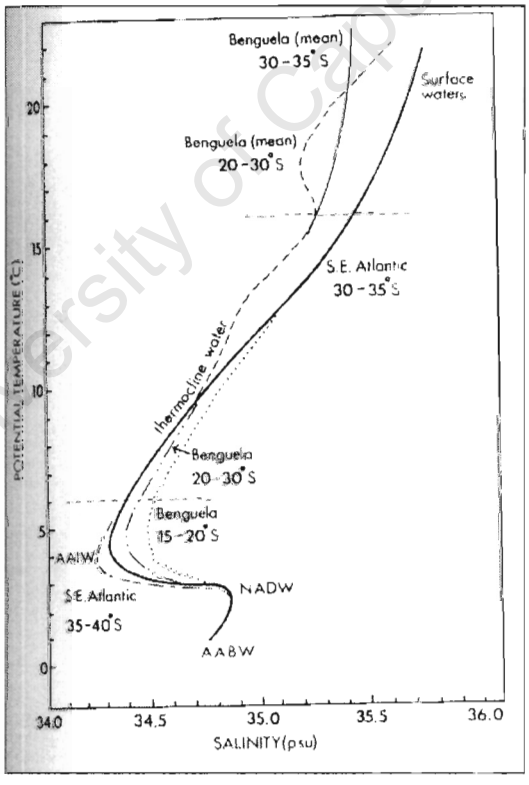

Figure 5: *A θS curve showing the most dominant water masses in the South-East Atlantic and Benguela Systems*

2.3.1 THERMOCLINE WATERS

This water mass makes up the thermocline at the upper end of the water column and is seen as the linear part of the θS curve (at ~6°C; 34.5psu to ~16°C; 35.5psu). It is often referred to as Central Water. This is the water mass that is upwelled along the coast and it is made up of, though sometimes highly modified, the shelf waters of the Benguela. Being in contact with the atmospheric and in the location of shallow water processes, its characteristics can vary significantly both temporally and spatially. Figure 5 shows the difference between the central waters found nearer to the coast (marked Benguela) from the true South Atlantic Central Water and other surface waters. It can be seen here that the water warmer than 10°C in the strata associated with the Benguela is generally about 0.2psu fresher for other waters over much of the range. In the portion of the thermocline that is less than 10°C, both the more saline tropical Atlantic Central Water and the fresher South Atlantic Central Water can be found. At the core of the stratum (10°C - 12°C) it is extremely difficult to distinguish these central waters from those advected from the Indian Ocean into the South-East Atlantic via Agulhas rings and filaments. High-density CTD data, nutrient analyses and CFC data are particularly helpful in distinguishing the source of these waters (Shannon & Nelson, 1996). Gordon et al (1992) has demonstrated the method of using CFC data to distinguish between the origins of the Thermocline Water.

2.3.2 ANTARCTIC INTERMEDIATE WATER (AAIW)

This water mass occurs below the Thermocline Water and displays typical values of salinities in the range of 34.2 – 34.5psu, potential temperatures of 4 – 5°C, and an average core depth of about 700-800m in the South-East Atlantic. In the South-Indian Ocean it is found slightly deeper at around 1100m (Shannon & Nelson, 1996). Valentine et al (1993) have estimated on a volumetric basis, that the AAIW accounts for approximately 52% of the water masses present above 1500m off southern Africa. As described by Shannon & Hunter (1988), the AAIW originating from the Indian Ocean, which enters the domain largely via the Agulhas Current, is more saline (S > 34.45psu) than the AAIW that is dominant in the South-East Atlantic. The AAIW that is of tropical Atlantic origin is also more saline than the AAIW of the South-East Atlantic. The exchanges between the AAIW and the lower thermocline waters are an important consideration for mixing processes. It was demonstrated by Gordon et al (1992) that about 50% of the AAIW in the Benguela region is of Indian Ocean origin. The circulation of the AAIW is similar to that of the overlying thermocline waters, with the Agulhas Current and its retroflection, the South Atlantic Current, the Benguela Current and the poleward flow situated just west of the shelf break being present (Shannon and Nelson, 1996).

2.3.3 NORTH ATLANTIC DEEP WATER (NADW)

The core of the NADW has a potential temperature of <3°C and a salinity >34.8psu (Shannon and Nelson, 1996). Sandwiched between the AAIW and the Antarctic Bottom Water (AABW), it comprises a layer between the 1000m and 3500m depths (Reid, 1989). This water mass originates in the North Atlantic and spreads southwards from there. While input into the Cape Basin is possible via the South Atlantic Current, the flow along the continental margin is generally polewards (Shannon and Nelson, 1996).

2.3.4 ANTARCTIC BOTTOM WATER (AABW)

This high density water mass has a core temperature < 1.4°C and a core salinity < 34.82 psu, as recorded in the Cape Basin. It lies below the NADW and at depths in excess of 3800m it fills the bottom of the water column. The Walvis Ridge acts as a barrier to the equatorward flow of the AABW in this region, but leakages through the ridge have been documented by Shannon & Nelson (1996). The general circulation of the AABW in the Cape Basin is cyclonic, with a poleward flow occurring along the continental margin. (Reid, 1994; Nelson, 1989).

2.3.5 GENERAL CIRCULATION IN THE BENGUELA REGION

Since Shannon & Chapman (1985) and Shannon (1985), addressed various aspects of the surface and thermocline water circulation, numerous articles have been written that contribute greatly to an improved understanding of the largescale circulation processes in this region. Several cruises have also been undertaken in this endeavour. During recent years, there have been major impacts from four of the related aspects that improved the understanding of the circulation, namely:

- Improved quantification of the sources and volume fluxes in the system.
- quantification, and a general acknowledgement of the influence of the Agulhas Current on the system. In particular, the effect that Agulhas Rings have on the heat and salt budgets of the area, have been documented.
- Documentation of the poleward undercurrent on the Benguela Shelf.
- Quantification of shelf circulation at the continental margin as a consequence of the extensive current measurements. (Shannon and Nelson, 1996).

Geostrophic calculations suggest that an equatorward transport of thermocline water by the Benguela Current at 32°S was on the order of 21Sv, and on the order of 18Sv further north at 28°S. Beneath this, a flux of about 4-5Sv of AAIW occurred (Stramma & Peterson, 1989). The end result is a total upper water column equatorward flux of approximately 25Sv. This

value is higher than the previous estimates of Garzoli et al (1984), which are on the order of 15Sv. Shannon and Nelson (1996) acknowledge however that the value of 25Sv may be an overestimate. Estimates made by Gordon et al (1992) come in close agreement with this value as well.

Of the equatorward flow, approximately 7Sv originates in the Indian Ocean and is transported into the system via Agulhas Rings (Van Ballegooyen et al, 1994). The rings also entrain about 5Sv of Atlantic water (Gordon et al., 1987). They translate at a typical rate of between 5 – 8 cm/s providing an important mechanism for injecting heat and salt into the region (Olson and Evans, 1986; Gordon and Haxby, 1990). The rings appear to not generally have a direct impact on the Benguela shelf, with instances of these occurrences as described by Shannon et al (1990). Shillington et al (1990) and Duncombe Rae et al (1992) being the exception rather than the rule (Shannon and Nelson, 1996).

The Northern Benguela is largely influenced by the Angola Current and South Equatorial Current / Undercurrent systems. Though the poleward flow from the Angola Current is small when compared to the equatorward flow by the Agulhas Current, it has been found that the tropical Atlantic is a major source of Thermocline Water in the region (Shannon and Nelson, 1996). A general circulation for the Northern Benguela has been formulated by Moroshkin et al (1970) and can be seen in Figure 6. It shows that Thermocline Water and AAIW is advected from the tropics in a poleward direction into the Benguela Region as far south as 27°S. A poleward transport at 27°S of 1.6Sv with an equatorward transport of upwelled water of 0.7Sv has been estimated (Gordon et al., 1995). The balance (of 0.9Sv) should feed the shelf upwelling further south with a net offshore flux of upwelled water there (Shannon and Nelson, 1996). Bearing in mind that, according to Ekman Theory, the surface shelf waters are more responsive to the wind, Shillington et al (1990) have shown that there is a westward flow of about 30cm/s associated with the Lüderitz upwelling cell at 27°S.

The total poleward subsurface flow over the Benguela Shelf and the continental slope was given by Nelson (1989). When this is taken in conjunction with the previously mentioned poleward flows of the AAIW, NADW and AABW, it can be concluded that at the eastern boundary, the net flow of the greater part of the water column is poleward. This occurs with the exception of equatorward flowing waters at the surface under the influence of the wind, and under the influence of the shelf-edge jet. (Shannon & Nelson, 1996).

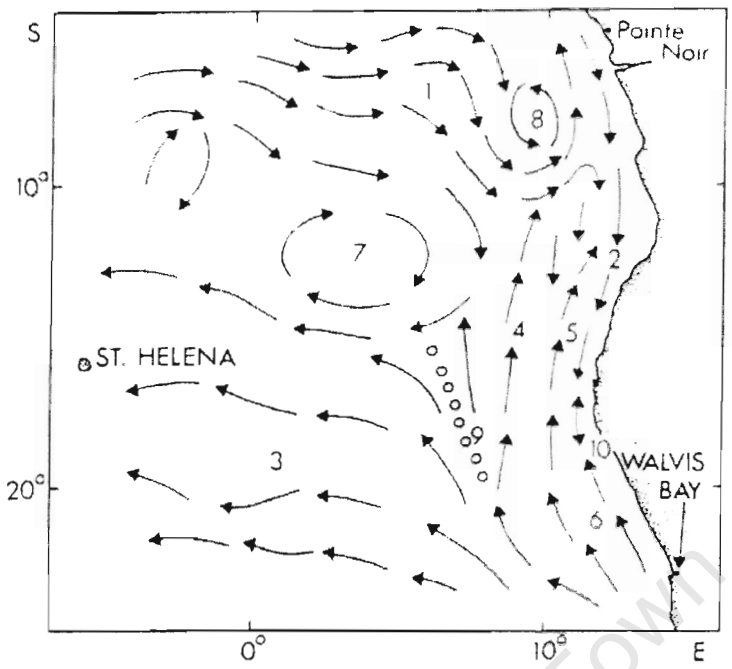

Figure 6: *Geostrophic water circulation in the upper 100m of the water column off the Angola and Namibian coastlines*

The features identified in Figure 6 are:

1. South Equatorial Countercurrent
2. Angola Current
3. Westward Branch of the Benguela Current
4. Northward Branch of the Benguela Current
5. Northward Branch of the Benguela Current
6. Northward Branch of the Benguela Current
7. Angola Dome
8. Region of anticyclonic curl
9. Benguela divergence zone
10. Merging zone of the Angola Current and Northward littoral branch of the Benguela Current

2.3.6 CIRCULATION ON THE SHELF

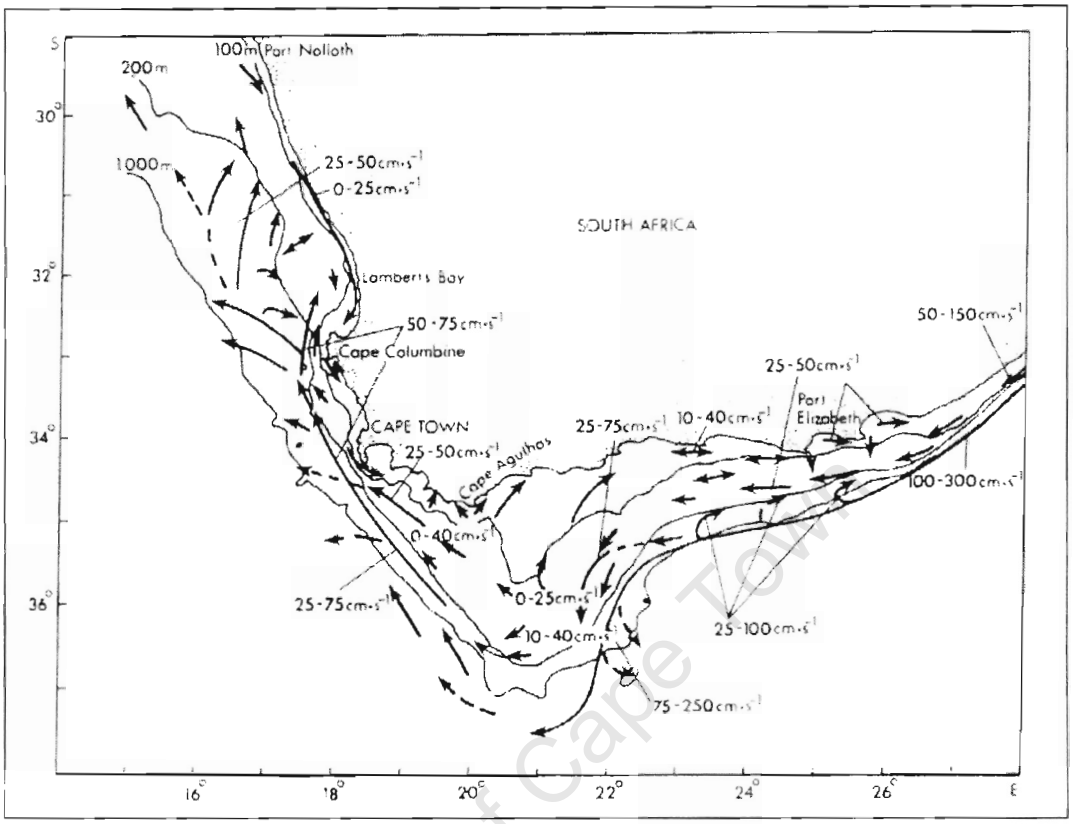

Figure 7: *Schematic diagram showing the circulation of the near surface current around the southwestern tip of Africa, from ADCP data collected between November 1989 and January 1992. Velocity ranges depict typical ranges and not extremes.*

The figure above shows the typical circulation on and around the shelf (near-surface) in the Benguela and Agulhas regions. The data used to generate this image comes from 13 cruises between 1989 and 1991, and was shown by Boyd et al (1992). The following features were identified by him based on this, as well as on the work of Boyd and Oberholster (1994):

- A convergent NW-orientated current system on the western Agulhas Bank that funnels into the West Coast jet current just off the Cape Peninsula as documented by Bang and Andrews (1974), Shelton and Hutchings (1982), Boyd et al. (1992), Largier et al. (1992), and Boyd and Shillington (1994) amongst others.
- A sluggish flow inshore of the 500m isobath as the inner shelf widens between Cape Town and Cape Columbine (moving equatorward), before speeding up to approximately 35cm/s.

- The current divides into two branches, through a process known as bifurcation, into an offshore flow and a longshore flow that is partially directed into St Helena Bay, as documented by Shannon (1985) and Nelson (1991).
- Upwelling plumes in both the Cape Peninsula and Cape Columbine regions in summer, with a constricted band of onshore flow just to the north of each plume (Agenbag 1992).
- North of St. Helena Bay, in the midshelf region, there is a mean onshore curvature towards Hondeklip Bay that binds a broad area of weak mean current to the east. The flow patterns around this area have a general northward trend.
- A southward current that often occurs near the surface close inshore over the entire region.

Additionally, a class of relatively short-lived motion that includes filaments and eddies are apparent on the satellite thermal and visual images (Shannon and Nelson, 1996). Agenbag (1992) demonstrated the method of using successive images to track features in the area, and showed the important role played by warm water spreading northwards adjacent to the shelf.

A particular semi-permanent feature exists as a large westward excursion of water from near Dassen Island (33.4°S, 18.1°E), which sometimes forms a mushroom-head shaped dipole beyond the shelf. This feature is possibly the result of instability between the shelf-edge jet and the subducted poleward undercurrent, or through nonlinear interactions between local currents and large scale circulation features. A similar process occurs near Cape Point on a smaller scale. Both these features differ in character from the plumes seen near Cape Columbine that are narrower and less persistent (Shannon and Nelson, 1996).

Bang & Andrews (1974) predicted and found, using direct current measurements, that a strong equatorward jet southwest of the Cape Peninsula exists. They estimated that the flux should be on the order of 7Sv thinking that it reached all the way to the bottom of the water column. It is now known that this flow is confined to the midwater and surface layers, and only to a strip of ~10km wide. This leaves it with a much smaller volume transport estimate of ~1Sv (Shannon and Nelson, 1996). A possible cause for the existence of this jet may lie in the upward displacement of the isopycnals that occur at the shelf break. This occurs throughout the West Coast (and other shelf breaks as well) and is a perennial feature. Through previous years, several attempts were made to study this flow but all suffered certain shortcomings (eg the works done by Shannon et al., 1981; Nelson, 1985). Shannon & Nelson (1996) verified the permanence of the jet using a ship mounted ADCP in 1989. The Jet was shown over the 300m – 400m isobaths and found to stretch from Cape Point to the Childs

Bank in varying strength. This can be seen in Figure 8. Further north of the Childs Bank, there is a general lack of data, but the ADCP section of Gordon et al., (1995) revealed that the jet there is weaker with a velocity of around 20cm.s^{-1} and found near the 200m – 300m isobaths.

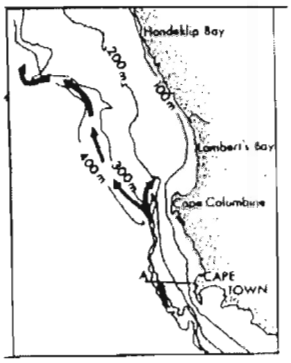

Figure 8: *The general appearance of the Shelf-edge Jet*[*]

Possibly the most well known mesoscale features in the Benguela are Upwelling and Filaments. A view of the climatological sea surface temperature anomalies over this area can give an idea as to the spatial extent of upwelling along the west coast of southern Africa. It shows a continuum of upwelling occurrences within which, a number of upwelling centres (or upwelling cells) are embedded. Shannon (1985) identified six major upwelling cells along the West Coast:

- Two perennial cells in the Northern Benguela just south of Cape Frio (18°S).
- The principal semi-permanent cell near Lüderitz (27°S)
- The perennial Namaqua Cell (30°S)
- The seasonal Columbine Cell (33°S)
- The seasonal Cape Peninsula Cell (34°S)

He also noted that the upwelling cells are usually located near regions of cyclonic wind stress curl and the typical westward extent of the influence of upwelling is between 150 – 250km, with a well developed longshore thermal system of fronts marking the extent of the upwelled water over much of the West Coast.

Upwelling Filaments are characteristic of the Benguela Oceanic Front, have typical lifespans of a few days to several weeks, and axes that are situated roughly perpendicular to the coast (Shannon and Nelson, 1996). Filaments have typical zonal dimensions of 200km but on occasion, may extend up to 1000km (Lutjeharms et al., 1991). Shillington et al. (1990) carried out an in-situ investigation of an Upwelling Filament and found it to be a relatively shallow feature confined to the upper 50m of the water column.

[*] from SHANNON and NELSON, 1996.

2.4 KEY QUESTIONS

This work sets out to answer some of the questions that have been raised regarding a numerical model of the Southern Benguela Region:

- What is the nature of the seasonality in temperature and salinity for the Benguela.
- What overall circulation pattern of the Benguela Region can be deduced using a numerical model, and does the circulation show any seasonal fluctuations?
- Is there a difference between the seasonal patterns observed at different locations along the West Coast?
- What significant differences are there between the modelled circulation and the conceptual circulation that is gained from the literature study?
- What enhancements on the understanding of upwelling does the model bring about.

3 CONFIGURATION OF THE MODEL

The model exists as a result of the requirements of the VIBES Project. In order to gain a better understanding of the physical processes affecting fish eggs, fish larvae, juvenile and adult fish during the recruitment cycle, a numerical model was required. The project enlisted the help of Dr. P. Penven to set up the model that, once completed, he named the Plume Model.

This chapter contains a description of the different aspects taken into account when creating Plume, and is in reference to his thesis.

3.1 PREVIOUS LITERATURE REVIEWED

As is done during all works of this nature, an extensive library of background work was researched prior to the set up of the Plume Model. Focus was placed on the shelf and slope dynamics specifically around the South and West Coast of Africa, but included studies conducted in other parts of the world as well. In the configuration of the Plume model, Penven gained valuable experience by studying the works of Van Foreest & Brundrit (1982) and Skogen (1998). To further understand how to apply a numerical model to his region of interest, he consulted works done by Barnier et al (1998), Biastoch & Krauß (1999) and de Miranda (1996), all of which were applied to an area that included the Benguela Region in their domains. Shortcomings of the abovementioned models with respect to the needs of the VIBES project were isolated and include: idealised forcing being incorporated, rigid lid approximations being used, stepwise or steep bottom topography causing errors in the calculations of the flow along the bottom, and resolutions being too coarse. The Plume Model was designed to improve on these shortcomings.

3.2 MODEL DESCRIPTION

In order to better estimate the flows along the bottom, which is of great importance to coastal dynamics, it was decided to make use of the bottom following σ-coordinate. He chose the Regional Ocean Modelling System (ROMS), which is a community code developed by the modelling groups at the Rutgers University and University of California Los Angeles in the USA, to create the model. ROMS belongs to a hierarchy of σ-coordinate models that originated with the Semi-Spectral Primitive Equation Model (SPEM), and the S-Coordinate Rutgers University Model (SCRUM). ROMS is an evolution of SCRUM and contains developments that are required to efficiently and robustly calculate the coastal circulations at

a high spatial resolution (eg: subgrid parameterisation, high order schemes, and high performance computing on SMP class computers).

3.2.1 THEORETICAL CONSIDERATIONS

EQUATIONS OF MOTION

The equations of motion, solved by the model, following the Bousinnesq and Hydrostatic Approximations take the form:

$$\frac{\partial u}{\partial t} = -u\frac{\partial u}{\partial x} - v\frac{\partial u}{\partial y} - w\frac{\partial u}{\partial z} + fv - \frac{\partial \phi}{\partial x} + F_u + D_u \qquad [2.1]$$

$$\frac{\partial v}{\partial t} = -u\frac{\partial v}{\partial x} - v\frac{\partial v}{\partial y} - w\frac{\partial v}{\partial z} - fu - \frac{\partial \phi}{\partial y} + F_v + D_v \qquad [2.2]$$

$$\frac{\partial T}{\partial t} = -u\frac{\partial T}{\partial x} - v\frac{\partial T}{\partial y} - w\frac{\partial T}{\partial z} + F_T + D_T \qquad [2.3]$$

$$\frac{\partial S}{\partial t} = -u\frac{\partial S}{\partial x} - v\frac{\partial S}{\partial y} - w\frac{\partial S}{\partial z} + F_S + D_S \qquad [2.4]$$

$$\rho = \rho(S,T,P) \qquad [2.5]$$

$$\frac{\partial \phi}{\partial z} = -\frac{\rho g}{\rho_0} \qquad [2.6]$$

$$0 = \frac{\partial u}{\partial x} + \frac{\partial v}{\partial y} + \frac{\partial w}{\partial z} \qquad [2.7]$$

Where:

- x, y, and z are the Cartesian coordinates with z being vertical and increasing upwards.
- u, v, w are the velocity components in the x, y, and z direction respectively.
- f is the Coriolis Parameter.
- ϕ is the Dynamic Pressure.
- F_u, F_v, F_T and F_S are the forcing terms.
- D_u, D_v, D_T and D_S are the dissipation terms
- T is the potential temperature
- S is the salinity
- P is the total pressure
- $\rho_0 + \rho$ is the total in-situ density
- g is the gravitational acceleration

The vertical boundary conditions were assigned as follows:

At the surface: $z = \zeta$

$$\kappa_M \frac{\partial u}{\partial z} = \frac{\tau^x_{surf}}{\rho_0} \quad [2.8]$$

$$\kappa_M \frac{\partial v}{\partial z} = \frac{\tau^y_{surf}}{\rho_0} \quad [2.9]$$

$$\kappa_T \frac{\partial T}{\partial z} = \frac{Q_T}{\rho_0 C_p} \quad [2.10]$$

$$\kappa_S \frac{\partial S}{\partial x} = (E - P)S \quad [2.11]$$

$$w = \frac{\partial \zeta}{\partial t} + u\frac{\partial \zeta}{\partial x} + v\frac{\partial \zeta}{\partial y} \quad [2.12]$$

At the bottom: $z = -h$

$$\kappa_M \frac{\partial u}{\partial z} = \frac{\tau^x_{bot}}{\rho_0} \quad [2.13]$$

$$\kappa_M \frac{\partial v}{\partial z} = \frac{\tau^y_{bot}}{\rho_0} \quad [2.14]$$

$$\kappa_T \frac{\partial T}{\partial z} = 0 \quad [2.15]$$

$$\kappa_S \frac{\partial S}{\partial z} = 0 \quad [2.16]$$

$$w = -u\frac{\partial H}{\partial x} - v\frac{\partial H}{\partial y} \quad [2.17]$$

Where:

- ζ is the free surface elevation
- κ_M, κ_T, κ_S are the vertical turbulent mixing coefficients, defined by a vertical turbulent closure scheme.
- τ^x_{surf}, τ^y_{surf}, are the surface wind stress components
- τ^x_{bot}, τ^y_{bot} are the bottom stress components. The bottom stress is parameterised in a sum of linear and quadratic terms:

$$\tau^x_{bot} = \left(\gamma_1 + \gamma_2\sqrt{u^2 + v^2}\right)u \quad [2.18]$$

$$\tau^y_{bot} = \left(\gamma_1 + \gamma_2\sqrt{u^2 + v^2}\right)v \quad [2.19]$$

- Q_T is the surface heat flux.
- E-P is evaporation less precipitation.
- H is the resting thickness of the water column.

Equations 2.1 and 2.2 express the momentum balance in the x and y directions. Equations 2.3 and 2.4 are the changes in salinity and potential temperature with respect to time. Equation 2.5 is the non-linear Equation of State. Equation 2.6 is the momentum balance in the vertical under the hydrostatic approximation and Boussinesq approximations. Equation 2.7 is the familiar Equation of Continuity for an incompressible fluid.

3.2.2 COMPUTATIONAL CONSIDERATIONS

COORDINATE SYSTEMS – THE GRID OF THE MODEL

Vertical σ stretched coordinate system

For a free sea surface, a generalized bottom following coordinate (σ) takes the form:

$$\sigma = \sigma\left(\frac{z-\zeta}{h+\zeta}\right) \quad -1 \le \sigma < 0 \qquad [\,2.20\,]$$

As an extension to this, a nonlinear stretching of the vertical coordinate that depends on the local water depth can be applied. (Song and Haidvogel, 1994). This enables a more uniform vertical resolution to be set up near the surface or the bottom, and can thus be used to give a better representation of the mixed layer and thermocline. The transformation that is applied in ROMS is:

$$z = h_\sigma + (h - h_\sigma)C(\sigma) \qquad [\,2.21\,]$$

where h_σ is a constant that is chosen as a typical surface mixed layer depth, and

$$C(\sigma) = (1-\theta_b)\frac{\sinh(\theta_\sigma)}{\sinh(\theta)} + \theta_b \frac{\tanh\left[\theta\left(\sigma + 1/2\right)\right] - \tanh\left(\theta/2\right)}{2\tanh\left(\theta/2\right)} \qquad [\,2.22\,]$$

A large θ, enhances the resolution in the surface layer. Additionally, if θ_b approaches 1, the resolution near the bottom boundary would be enhanced. The vertical velocity in σ coordinate direction is defined as:

$$\Omega = \frac{\partial \sigma}{\partial z}\left[w - (1+\sigma)\frac{\partial \zeta}{\partial t} - u\left(\frac{\partial z}{\partial x}\right)_\sigma - v\left(\frac{\partial z}{\partial y}\right)_\sigma \right] \qquad [\,2.23\,]$$

Once the coordinate system is transformed, the conditions placed on the system by 2.12 and 2.17, at the surface (σ = 0) and the bottom (σ = -1) means:

$$\Omega = 0 \qquad [\,2.24\,]$$

Horizontal Curvilinear Coordinates

ROMS makes use of horizontal curvilinear coordinates, which conforms to irregular boundaries and can be used to place more computational resolution in a specific region of interest. In Plume, the focus for greater resolution was placed near the coast. The coordinates are introduced by a transformation in the horizontal coordinate from x,y space to ξ,η space, as shown in the figure below, where the relationship of horizontal arc length to the differential distance is given by the formulae 2.25 and 2.26 as:

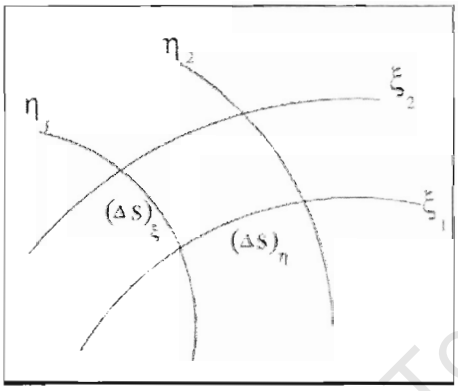

Figure 9: *Horizontal curvilinear coordinate system*

$$(\Delta s)_{\xi} = \left(\frac{1}{m}\right) d\xi \qquad [\ 2.25\ ]$$

$$(\Delta s)_{\eta} = \left(\frac{1}{n}\right) d\eta \qquad [\ 2.26]$$

Here, m(ξ,η) and n(ξ,η) are the scale factors that relate the differential distances (Δξ,Δη) to the physical arc lengths $[(\Delta s)_{\xi},(\Delta s)_{\eta}]$.

Coastal Boundaries as a grid

It is possible that coastal boundaries be specified via a finite-discretised grid using a land/sea masking technique. This is applied in the Plume Model.

DISCRETISATION SCHEME

On a horizontal plane, for most of the variables, the model makes use of a centred second-order finite-difference approximation adopted on an Arakawa C grid. The variables u and v are discretised differently, resulting in the staggered horizontal discretisation scheme as shown below.

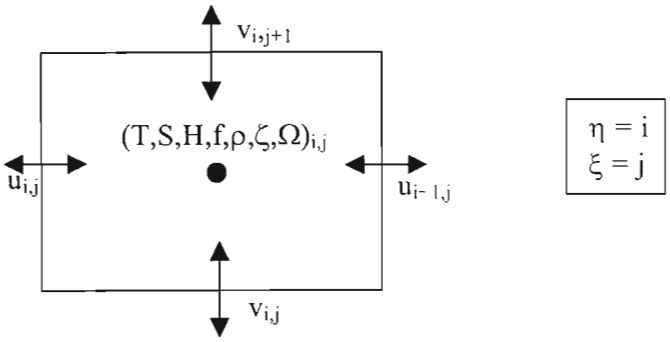

Figure 10: *Positioning of the variables on the Arakawa-type horizontal grid. The Discretisation scheme for the horizontal plane*

This scheme is effective in dealing in situations where the horizontal resolution is fine when compared to the first radius of deformation.

On the vertical plane, a staggered second-order finite-difference approximation is also applied. The vertical discretisation scheme is shown in the figure below.

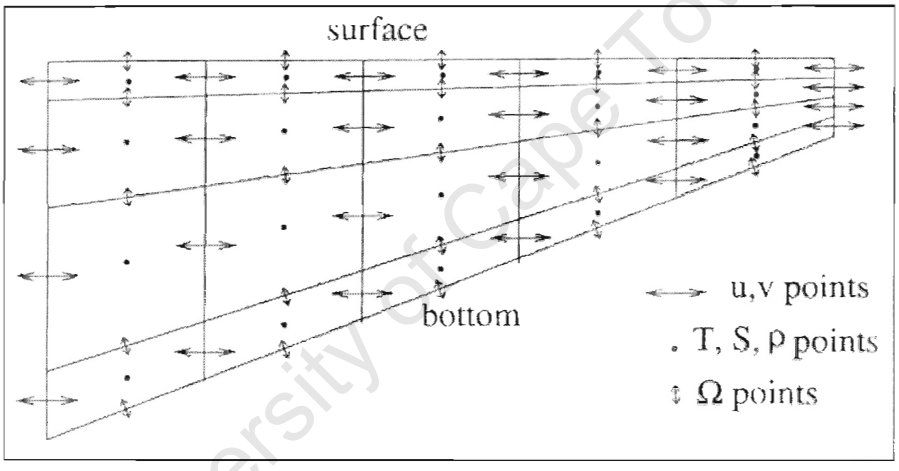

Figure 11: *The Discretisation scheme for the vertical plane*

The choices made for the discretisation schemes are traditional for second-order finite-difference models.

The hydrostatic primitive equations for momentum are solved using a split-explicit time-stepping scheme that requires a special treatment to deal with aliasing and a coupling between barotropic and baroclinic modes. Within each baroclinic step, a number of barotropic steps are calculated in order to evolve the free surface and vertically integrated momentum equations. In order to avoid the errors that are associated with aliasing of the frequencies that are resolved in the short barotropic steps but remain unresolved in the long baroclinic steps, the barotropic fields are time-averaged before they replace the values obtained by the

baroclinic step. This time-average on the barotropic field is done using a cosine shaped time filter that is centred at each new time level. Additionally, the separated time-stepping is constrained allowing for volume conservation, as well as the preservation of all constants necessary in tracer equations used in the model. All the 2D and 3D equations are time discretised using a third-order accurate predictor (Leap-Frog) and corrector (Adams-Molton) time-stepping algorithm. This has proved to enhance the stability and has allowed for larger timesteps than in other numerical schemes. The larger timesteps offsets the increased cost of the predictor-corrector algorithm.

THE PRESSURE GRADIENT SCHEME

The Pressure Gradient Error

One of the biggest advantages of using the σ-coordinate comes from the transformation from sea-surface or ocean bottom to σ-coordinate level. However, this causes great difficulty when attempting to calculate the pressure gradient as it introduces the pressure-gradient error. In the case of Plume, the sea-surface was always at σ = 20 and the ocean-bottom was always at σ = 0. For a constant σ, the x-component of the pressure gradient force is determined by the sum of two terms as shown in the following formula:

$$\left.\frac{\partial p}{\partial x}\right|_{z=Const} = \underbrace{\left.\frac{\partial p}{\partial x}\right|_{\sigma=Const}}_{A} \underbrace{-\frac{\sigma}{h}\frac{\partial p}{\partial \sigma}\frac{\partial h}{\partial x}}_{B} \qquad [2.27]$$

In the equation above, term A involves the variation of pressure along a line of constant σ, while term B is the hydrostatic correction. When using this equation near steep topography (ie: in regions where both term A and $\frac{\partial p}{\partial \sigma}$ are large), the two terms tend to cancel each other out, but a small error in computing each term can result in a relatively large error in the horizontal pressure gradient. (Song, 1998).

The Hydrostatic Inconsistency

A second source of error, as described by Haney (1991), is the hydrostatic inconsistency. It was demonstrated that, when using the second-order discretisation of 2.27, it is equivalent to interpolating the pressure between two consecutive σ layers to obtain the horizontal pressure gradient (Kliem & Pietrzak, 1999). The hydrostatic inconsistency arises if the slope and horizontal resolution are such that the extrapolation occurs instead of interpolation.

Minimisation of errors in calculating the Pressure Gradient

Kliem & Pietrzak (1999) and Song (1998) determined ways in which errors could be reduced.

- The truncation error in the derivation of 2.27 can be reduced by subtracting a horizontally homogeneous averaged density, $\overline{\rho}(z)$, to the density field. This method is only effective in small domains where the horizontal variations in density are limited.
- Transforming the density back to the Cartesian Space (z levels) before computing the pressure gradient. Problems can arise thereafter when computing values for the highest and lowest σ levels, and could end in extrapolations over steep topography.
- Using higher order numerical schemes. This will however increase the cost with respect to time in the running of the model.
- By retaining integral properties such as mass, energy and vorticity.

It is believed that the best pressure gradient formulation should minimize truncation errors while retaining integral properties.

The Pressure Gradient Scheme implemented in ROMS

ROMS uses the weighted Jacobian formulation proposed by Song (1998). It has been designed to minimise the truncation errors and to retain integral properties. If σ is the generalized bottom following coordinate system, the horizontal pressure gradient can be derived in a Jacobian form as follows:

$$\left.\frac{\partial p}{\partial x}\right|_{z=Const} = \left.\frac{\partial p}{\partial x}\right|_{z=\zeta} + \frac{g}{\rho_0}\int_{\sigma}^{\zeta}\left\{\frac{\partial z}{\partial \sigma'}\frac{\partial p}{\partial x} - \frac{\partial z}{\partial x}\frac{\partial p}{\partial \sigma'}\right\}d\sigma' \qquad [\,2.28\,]$$

Hence, the vertical variations in the horizontal pressure gradient are given by an integral of the Jacobian as follows:

$$J(z,\rho) = \frac{\partial z}{\partial \sigma}\frac{\partial \rho}{\partial x} - \frac{\partial z}{\partial x}\frac{\partial \rho}{\partial \sigma} \qquad [\,2.29\,]$$

Song (1998) defined the standard Jacobian formulation as the second-order central-difference discretisation of 3.29. He also proposed a weighted Jacobian scheme that is centred in z-space rather than in σ–space, as it is in the standard Jacobian formulation. Also in this paper, he shows that whilst the standard Jacobian is better when the hydrostatic inconsistency condition is satisfied, the weighted Jacobian gives superior results if the condition is violated. It is often the case, in realistic conditions, for the condition to be violated.

THE ADVECTION SCHEME

Previous ocean models have used second-order central-difference schemes for the treatment of advection. In conjunction with these, higher-order Laplacian diffusion operators or low-pass filters are applied in order to smooth the numerical noise that is induced by the dispersive computational errors or turbulent cascades. In ROMS, the advection operator for the momentum and tracer variables has been redesigned to reduce the dispersive errors by using an upstream-biased third-order scheme. This scheme results in explicit smoothing of the fields (by diffusion operators and low-pass filters) no longer being necessary, and thus enhances the effective resolution of the solution for the given grid. (Shchepetkin & McWilliams, 1998).

THE TURBULENCE-CLOSURE SCHEME

The parameterisation of the unresolved physical vertical mixing processes in ROMS is done via a non-local, K-profile planetary (KPP) boundary layer scheme (Large et al., 1994). There are two distinct parameterisations: one for the ocean interior and one for the oceanic surface boundary layer.

The depth of the boundary layer, which is a function of the surface forcing, the buoyancy, and the vertical velocity profile, is determined by equating a bulk Richardson number relative to the sea surface to a critical value. Once the depth of the boundary layer is found, the parameterisations can be applied.

Below the boundary layer, the vertical mixing is regarded as a superposition of three processes: vertical shear, internal wave breaking, and double diffusion. In the surface layer, the diffusivity is formulated to agree with the theory of turbulence. At the base of the surface layer, both diffusivity and its gradient are made to match the interior values.

3.3 CONFIGURATION OF THE PLUME MODEL

Once the theoretical and computational aspects were all accounted for, it was possible to proceed to the actual configuration of the model. Aspects that had to be dealt with during this configuration were:

- The configuration of the model grid,
- the initial conditions and the boundary conditions, and
- aspects pertaining to the time-dependant fluxes at the surface and other boundaries.

This section examines each of these aspects in greater detail.

3.3.1 THE PLUME GRID

HORIZONTAL GRID

The important constraining factors taken into account when setting up the grid for the Plume model were:

- The domain must be large enough to contain the most important dynamic features that are known to have an effect on the transport of eggs and larvae, and have enough space for these features to develop.
- The domain should be small enough so that a high resolution could still be maintained.
- According to Penduff (1998), the open boundaries should cross the current at a right angle, placed where there are minimums in current speed and variability, and placed where the topographic gradient perpendicular to the boundary is a minimum in order to avoid along-boundary currents.

To satisfy as much of these factors as possible, the grid was designed as shown in Figure 12.

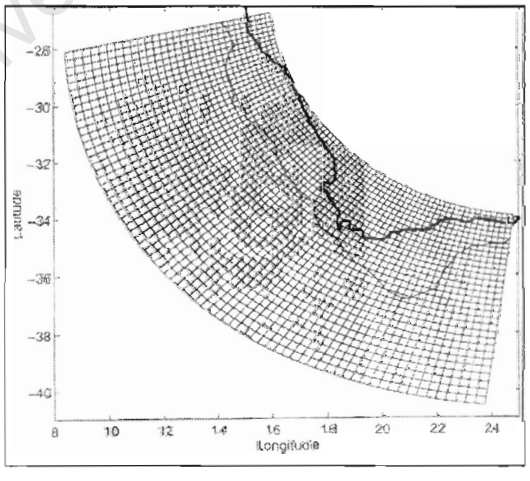

Figure 12: *The horizontal curvilinear coordinate grid chosen for the model is shown superimposed above the coastline and the approximate position of the shelf break.*

The grid roughly follows the southwest corner of Africa, which reduces the number of masked points that cause unnecessary time loss in the run. The resolution is identical in the ξ and η directions. In order to facilitate the connections to the open ocean, the grid was chosen in such a way that the northern and eastern boundaries cuts the shelf at, or close to narrow points.

Due to the presence of the highly energetic Agulhas Current, the Eastern boundary is unfortunately not located at a place where the currents are weak. In order to deal with this feature, Penven had to rely on a specific open-boundary scheme. The offshore eastern boundary of the model grid was placed south of the shelf break (on the ocean plane) ~300km from the tip of the Agulhas Bank. In this way, the final domain is 1300km long on its inner radius, 2240km long on it's outer radius, and ~740km wide.

The model was run using a low-resolution configuration that changed linearly from 18km at the coast to 31km offshore, and a high-resolution configuration that changed linearly form 9km at the coast to 18km offshore. The Plume model that is analysed in this work, is derived from the results of the high-resolution configuration.

The grid is isotropic and thus does not produce a dissymmetry in the dissipation of turbulence, and also the resolution at the coast where higher accuracy is needed, is higher than offshore.

Penven recognised that although the applied pressure gradient scheme allowed the presence of a steeper slope, some topographic smoothing may still be necessary to ensure stable and accurate simulations using realistic bathymetry. Haidvogel et al (2000) used a number, r, to assist in a similar situation. The number, r, was calculated as follows:

$$r = \frac{\Delta h}{2h} = \frac{h^{+1/2} - h^{-1/2}}{h^{+1/2} + h^{-1/2}} \qquad [2.30]$$

Empirical studies showed that good results were obtained when r does not significantly exceed the value of 0.2. In order to smooth the topography only were it was required, a Shapiro filter weighted by the values of r was applied in the following manner:

- if r < 0.15, the weighting = 0
- if r >= 0.15 the weighting = 1.

Thus the filter would only be used where the value of r was found to exceed the critical value of 0.15. Figure 13 compares the unsmoothed ocean topography to the smoothed ocean topography. One can see that though the filter has smoothed out the finer features such as the Cape Canyon and steep wall south of the Agulhas Bank, the major topographical features remain present in the bathymetry.

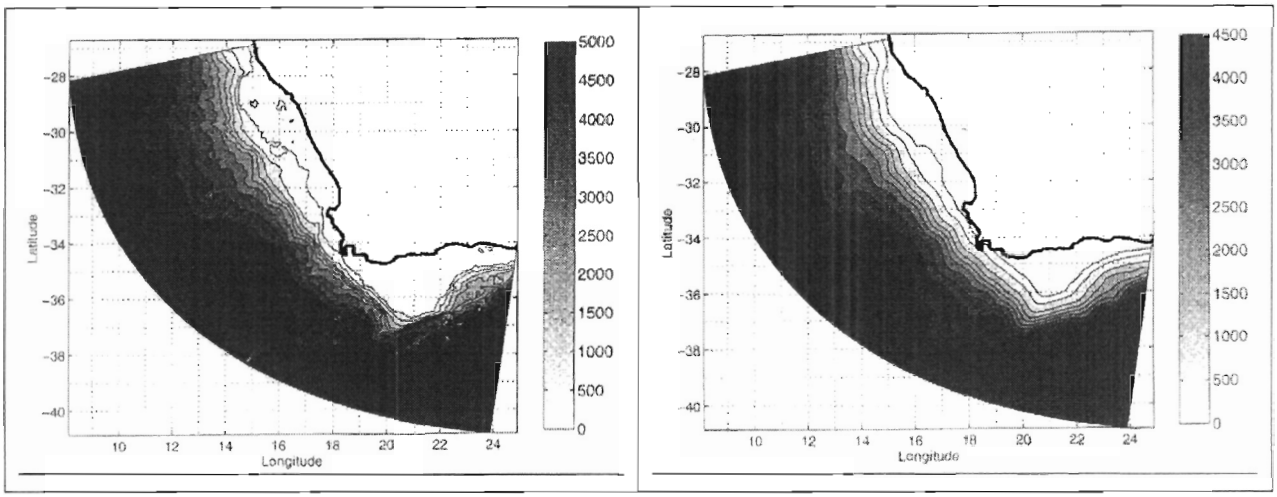

Figure 13: *A (left) and B (right) shows the raw and smoothed topography of the model domain respectively*

THE VERTICAL GRID

For the vertical, 20 different levels were chosen. Tests using an increased number of vertical levels were conducted to explore the improvement that this had on resolution at the bottom layers. These tests showed that the results did not display a significant improvement on the solution, leading to the decision to use only 20 levels. The vertical grid can be pictured as shown in the figure below:

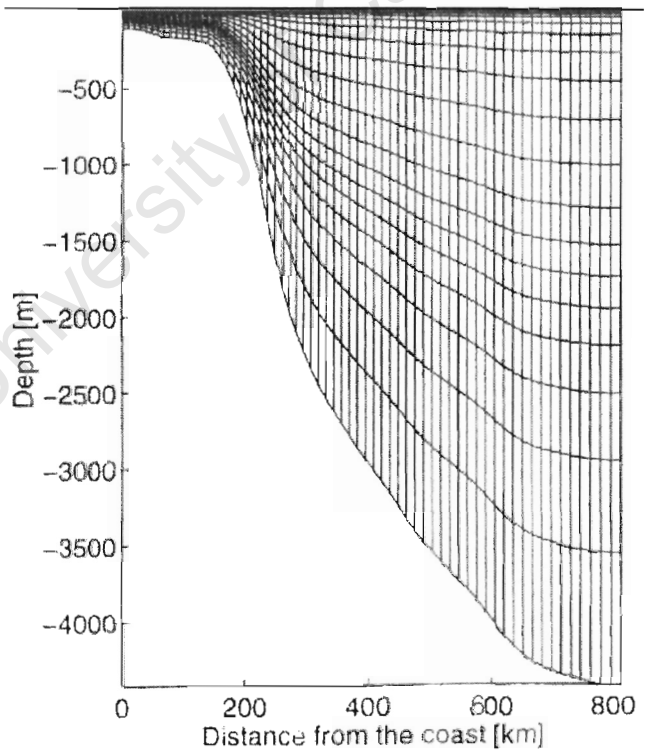

Figure 14: *The vertical σ-coordinate system. These are the vertical levels of the r points for a cross section off the shelf north of St. Helena Bay looking south.*

The minimum depth was fixed at 30m and the maximum depth was fixed at 5000m. The grid was set up in such a manner as to have a greater resolution near the surface where most of the variability and biological activity occurs. This was accomplished by setting the following:

- $\theta = 7$,
- $\theta_b = 0.3$, and
- $h_\sigma = 20$ metres

in equations 2.21 and 2.22. The result was a resolution of finer than 5m for the entire surface, but which grew to be very coarse (up to 1km) at the deepest points in the domain. Table 1 displays the calculated depths of the different levels where the bottom is at 30m, 2515.0m and 5000m depth respectively.

Level #	h = -30m	h = -2515.0m	h = -5000m
20	0.0	0.0	0.0
19	-1.0	-2.8	-4.7
18	-2.0	-6.5	-11.0
17	-3.0	-11.9	-20.7
16	-4.1	-20.5	-36.9
15	-5.1	-35.2	-65.2
14	-6.2	-61.1	-116.0
13	-7.4	-106.4	-205.5
12	-8.7	-181.7	-354.8
11	-10.1	-294.2	-578.3
10	-11.7	-436.9	-862.2
9	-13.3	-586.2	-1159.0
8	-14.8	-719.0	-1423.2
7	-16.3	-831.1	-1645.8
6	-17.7	-934.0	-1850.4
5	-19.1	-1045.7	-2072.2
4	-20.7	-1184.8	-2348.9
3	-22.4	-1371.8	-2721.2
2	-24.5	-1631.7	-3238.9
1	-26.9	-1997.5	-3968.1
0	-30.0	-2515.0	-5000.0

Table 1: *Height of the different s-coordinate levels above the surface in metres for different bottom depths (h).*

3.3.2 INITIAL CONDITIONS AND BOUNDARY CONDITIONS

THE OPEN BOUNDARY SCHEME

The model required a well-behaved, long-term solution for a configuration with open boundaries on up to three sides of the model grid. This numerical boundary scheme was needed to allow the inner solution to radiate through the boundaries with little reflection, and at the same time allow the information from the surrounding ocean to enter the domain. Marchesiello et al (2000) demonstrated that the active open boundary scheme implemented in ROMS estimates the two dimensional horizontal phase velocities in the vicinity of the

boundary. According to Raymond and Kuo (1984), for each model variable, ϕ, the normal (c_x) and tangential (c_y) phase velocities as it propagates through the domain are:

$$c_x = -\frac{\frac{\partial \phi}{\partial t}\frac{\partial \phi}{\partial x}}{\left(\frac{\partial \phi}{\partial x}\right)^2 + \left(\frac{\partial \phi}{\partial y}\right)^2} \qquad [2.34]$$

$$c_y = -\frac{\frac{\partial \phi}{\partial t}\frac{\partial \phi}{\partial y}}{\left(\frac{\partial \phi}{\partial x}\right)^2 + \left(\frac{\partial \phi}{\partial y}\right)^2} \qquad [2.35]$$

If the propagation is from the interior of the model domain towards the boundary, the reflection is avoided using the following wave equation:

$$\frac{\partial \phi}{\partial t} + c_x \frac{\partial \phi}{\partial x} + c_y \frac{\partial \phi}{\partial y} = \frac{\phi_{data} - \phi}{\tau_{out}} \qquad [2.36]$$

And if the propagation is from the open ocean towards the interior, the values at the boundary are nudged towards the data using:

$$\frac{\partial \phi}{\partial t} = \frac{\phi_{data} - \phi}{\tau_{in}} \qquad [2.37]$$

- Where τ_{in} and τ_{out} are the relaxation times
- And ϕ_{data} and ϕ are the specified value of the variable and the value of the variable calculated by the model respectively. This naming scheme continues later.

The tangential and normal components are discretised in ROMS using an upstream biased function in which the normal component is treated implicitly allowing the use of larger timesteps without the loss of stability. At the corners, the average values of the two adjacent boundary points are taken. Mass conservation around the entire domain is enforced (Marchesiello et al., 2000).

Problems arise when gridpoints are found to be a location of inflow for one process as well as a point of outflow for another process, but affecting the same variable. The series of steps taken in order to obtain a long-term stable solution to this problem are:

- The solution is weakly relaxed towards data in outflow conditions.
- The solution is weakly nudged towards the data in nudging bands close to the boundaries. For Plume, the nudging coefficient decreases linearly in the six points near the boundaries.
- A sponge layer with a linearly increasing mixing coefficient filters out any possible numerical noise or reflections produced near the open boundaries.

This method filters the model solution so that it connects smoothly to the surrounding open oceanic data, whilst still allowing it to develop a meaningful internal solution. The relaxation times are chosen empirically to avoid long-term drift and over-specification. The values chosen were:

- τ_{out} = 360 days all variables
- τ_{in} = 10 days for all velocities
- τ_{in} = 3 days for the tracers

A simple non-gradient scheme is applied for the boundary condition for the free surface elevation as it does not affect the inner solution for this variable on a C-grid.

The presence of the Agulhas Current that flowed into the eastern boundary of the domain caused to solution to be unstable after one or two years of simulation. The highly energetic, meandering current required a specific open boundary scheme in order to obtain a long-term stable solution. This was implemented into the code for the barotropic component of the velocities perpendicular to the boundaries. The scheme was originally applied by Flather (1976) for tidal models, and involves a one dimensional radiation equation (2.38) along with a one dimensional version of the linearised continuity equation (2.39) that is given as follows:

$$\frac{\partial \bar{u}}{\partial t} \pm c \frac{\partial \bar{u}}{\partial x} = 0 \qquad [2.38]$$

$$\frac{\partial \zeta}{\partial t} + H \frac{\partial \bar{u}}{\partial x} = 0 \qquad [2.39]$$

$$\Rightarrow \frac{\partial \bar{u}}{\partial t} = \pm \frac{c}{H} \frac{\partial \zeta}{\partial t} \qquad [2.40]$$

$$\Rightarrow \bar{u}_{bound} = \bar{u}_{data} \pm \frac{c}{H} (\zeta - \zeta_{data}) \qquad [2.41]$$

The sign in 2.41 depends on the position of the boundary in relation to the direction of wave propagation. For the phase velocity, assuming that the waves approaching the boundary are non-dispersive surface gravity waves, the celerity, c, is fixed at $c = \sqrt{gH}$ where g is the gravitational acceleration and H is the water column depth. Substituting into 2.41 yields:

$$\Rightarrow \bar{u}_{bound} = \bar{u}_{data} \pm \sqrt{\frac{g}{H}} (\zeta - \zeta_{data}) \qquad [2.42]$$

This scheme can be viewed as a one-way nesting scheme that conserves mass. The differences between the specified values and the calculated values are forced to radiate at the speed of surface gravity waves. It was recognised by Palma & Matano (1998) that the

constant provision of information by the boundary could over-determine the inner solution, but a case conducted using a shallow water model showed that this scheme provided the best overall performance. In the Plume model it was observed that this scheme also stabilized the inner solution, with the disadvantage being that the control from the boundaries could limit the physical significance of the solution obtained inside the model domain.

THE CLIMATOLOGY FIELDS

An initial attempt was made by using the Levitus global monthly climatology dataset to derive the initial and boundary conditions (Levitus, 1982). From this dataset, the sea surface elevation is computed as the dynamic height in reference to 500m depth and the baroclinic velocities are derived from the thermal wind relationship. The disadvantages of this method were:

- The solution was dependant on an arbitrary choice of the stationary reference level.
- Extrapolation was necessary to obtain data for use on the shelf and this gave spurious recirculation.
- The Agulhas Current was badly represented.

It was possible to obtain a solution using climatologies from this dataset, but an alternate method was sought. Seasonally averaged data derived from a z-coordinate, 1/3° resolution, basin-scale model of the South-Atlantic and Indian Oceans using a rigid-lid approximation was used as climatological inputs (Biastoch & Krauß, 1999). The disadvantage of this was that the use of the rigid-lid approximation meant the free surface elevation had to be calculated from the other variables. The seasonal data gave, or made it possible to calculate, a cyclical annual datastream that was needed to calculate each model variable. In order to avoid discontinuities resulting from differences in the climatological and model timesteps, ROMS executes a linear interpolation in time so that there is data for each model timestep.

For the initial conditions, the summer climatological values were used, and the model density field being calculated from the associated temperature and salinity variables. The variables $u, v, \bar{u}, \bar{v}, \zeta$ are set to zero initially. Under these conditions it was expected that the model would take a short time to reach an equilibrium state.

3.3.3 SURFACE FLUXES

ATMOSPHERIC FORCING

The atmospheric forcing fields are based on the data for monthly climatologies that is derived from the Comprehensive Ocean-Atmosphere Data Set (COADS) (Da Silva et al., 1994). The momentum forcing at the surface is given by the longitudinal and latitudinal components of the wind stress. Seasonally averaged vectors for wind stress are shown in Figure 15.

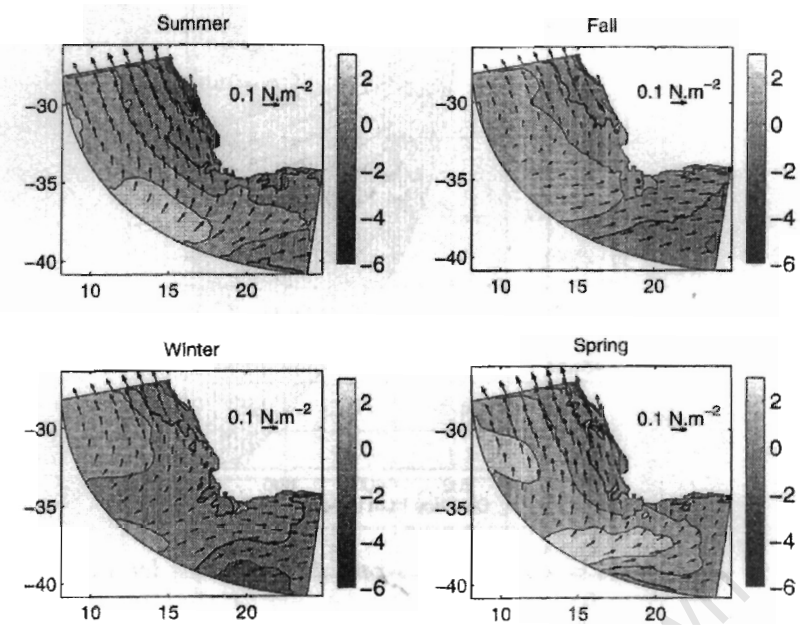

Figure 15: *Seasonally averaged vectors for windstress*

THERMOHALINE FORCING

The thermohaline forcing set up proved to be less straightforward than the atmospheric forcing discussed above. It is possible that this forcing may lead to an undesirable drift in the model as the feedback to the atmosphere is neglected entirely. It is for this reason that large basin scale models are often nudged back towards monthly mean climatological fields. Two related fluxes, viz the heat and fresh water fluxes were identified and considered.

Heat Flux

Barnier et al (1998) identified a method that is more satisfactory than the nudging-method. It attempted to linearise the thermal forcing around the climatological sea surface temperature (T_{clim}), in order to the feedback that the model sea surface temperature (T_{mod}) has on the surface heat fluxes. It was represented as:

$$\partial Q / \partial T_{c\,\mathrm{lim}} = \frac{Q_T - Q_{net}}{T_{\mathrm{mod}} - T_{c\,\mathrm{lim}}} \qquad [\,2.31\,]$$

Q_{net} is computed from the different contributions for the heat fluxes (infrared, sensible, and latent heat fluxes) and equals the term $\partial Q / \partial T_{c\,\mathrm{lim}}$ (Siefridt, 1994). This results in:

$$\partial Q / \partial T_{c\,\mathrm{lim}} = -4\sigma T_{c\,\mathrm{lim}}^3 - \rho_{atm} C_p C_h U - \rho_{atm} C_e L U \left[2353 \log\left(\frac{q_s}{T_{c\,\mathrm{lim}}^2} \right) \right] \qquad [\,2.32\,]$$

Where

- σ is the Stefan-Boltzman Constant,
- C_p is the specific heat of the atmosphere,
- C_h is the sensible heat transfer coefficient,
- U is the wind speed,
- C_e is the latent heat transfer coefficient,
- L is the latent heat of vaporisation and,
- q_s is the sea-level specific humidity.

Fresh Water Flux

The fresh water fluxes are specified as salt fluxes based on the climatological precipitation (P) and evaporation (E) fields from COADS. It is possible that the use of E-P regardless of the feedback from the model solution can cause a constant drift in the solution (Haidvogel et al., 2000). A method similar to the heat flux correction was unsuccessfully applied to the model. However since there is very little evaporation over the cold Benguela region, combined with low precipitation, the E-P term is also small for the West Coast. When compared to the salinity fluxes that occur at the lateral boundaries of the model, it is seen that the fresh water flux from the surface should be negligible and the solution should not drift excessively from the climatological values.

4 METHODOLOGY

This section of the work gives a detailed description of the methods used to calculate the Climatologies and anomalies used in the following sections, from the output of the Plume Model. Its purpose is to provide the reader with the method by which the dataset was formulated in order to answer the key questions posed in Section 2.4. The general structure followed by this section is:

- To provide a brief description of the output.
- To identify several areas of interest and select a timeperiod in the model's domain.
- To identify the variables that will be used, as well as those that may provide valuable insight into the physical processes that occur.
- To provide the method used to calculate any derived quantities from the primary output.

4.1 THE PRIMARY OUTPUT

The model output is saved in a format known as "Network Common Data Format" or NetCDF. This format, used widely in scientific studies, facilitates easier storage and retrieval of data structures in self-describing, machine-independent files. It was decided that, since the data would be processed using both Linux and Windows Platforms, Matlab and the corresponding NetCDF Toolbox for Matlab would be ideal processing tools due to their ability to facilitate the crossing between the two Operating Systems.

The Plume Model output has 71 variables calculated in 2-day time intervals, saved year by year for 10 years, on a grid with dimensions as specified in the previous section. This resulted in 10 different NetCDF files being saved after the run of the model.

As NetCDF files are intended to be self-describing, each separate file contained information, in the header, about what it contained. The headers are easily viewable using NetCDF tools. Table 2 shows some of the variables that appear in the header, as well as the description (given as the "long name"), and the units of measurement. In order to avoid any confusion with the international oceanographic standards for the use on the variables 'U' and 'V', it is necessary to state that in formulating the model and in the remainder of this dissertation, U represents the velocity component along the xi axis (which increases in an offshore direction), and V represents the velocity component along the eta axis (which is generally longshore and increases in an anticlockwise direction).

Variable Short Name	Variable Long Name	Units of Measurement
Zeta	Free Surface	Metres
Ubar	Vertically Integrated u-velocity component	Metres per second
Vbar	Vertically Integrated v-velocity component	Metres per second
U	U-velocity component	Metres per second
V	V-velocity component	Metres per second
W	Vertical velocity component	Metres per second
omega	S-coordinate vertical velocity component	Cubic Metres per second
Temp	Potential Temperature	Degrees Celsius
Salt	Salinity	PSU
Shflux	Surface Net Heat Flux	Watts per square metre
Sustr	Surface u-velocity stress	Newtons per square metre
Svstr	Surface v-velocity stress	Newtons per square metre

Table 2: *A tabular extract of the variables that appear in the NetCDF header file.*

4.2 THE SELECTED AREAS AND TIMEPERIOD OF INTEREST

The factors taken into consideration when making this decision were:

- The locations should be close to the surface and close to the coast. The original configuration of the Plume Model provided a greater resolution at the surface and close to the coast due to this area being of greater interest to the fish-recruitment process. The locations should however be deep enough to include the entire surface layer, and extend a reasonable distance offshore.
- The locations should be placed in such a way that they could be compared with respect to spatial differences, shelf width, and mesoscale activity while the comparison rendered meaningful results.
- The entire timeperiod should be long enough so that longer-term interannual events as well as the shorter-termed intra-seasonal events would be detected. The time interval should be such that the greatest possible resolution is maintained while still keeping computational cost to a reasonable amount.
- The first two years of the model's output were considered as "spin-up" years, and should not be taken into consideration.

After consideration of these factors, it was decided to select three 2-dimensional sections from the model output for closer investigation. The three sections would be at different locations along the West Coast all extending along a line of constant eta on the model grid. The would be chosen in such a way as to gain a good reflection of any latitudinal variation that may occur along the West Coast and would all extend offshore until, at least, a point beyond the shelf-break. The sections would extend to a depth of 200m and would continue for

20 xi-points from the closest point inshore, thus the offshore distance would vary from transect to transect. A Matlab script was used to find three suitable gridpoints on the Plume grid that were as close as possible to Cape Point, Cape Columbine and the Olifants River Estuary. Once these starting points were found, the sections were constructed by taking the next 19 xi-points from the starting location. The sections are identical to a transect that a research vessel would perform if it were to travel along a straight line from the starting point to the end point of each section. They are therefore named, the Cape Point Transect (CPT), the Cape Columbine Transect (CCT) and the Oliphants River Estuary Transect (ORET). The geographical details of the three transects are listed in Table 3.

Transect Name	Start of Transect	End of Transect	Horizontal Distance
Cape Point Transect (CPT)	34°31'51.3075"S 18°28'29.4393"E	36°18'25.2380"S 16°54'10.7128"E	243km
Cape Columbine Transect (CCT)	32°25'02.2405"S 18°07'47.2575"E	33°48'27.3606"S 16°21'41.4616"E	214km
Olifants River Estuary Transect (ORET)	31°30'06.7586"S 17°57'38.7843"E	32°43'30.3858"S 16°21'54.7322"E	202km

Table 3: *Geographical details of the three selected transects.*

Figure 16 details the location of the three transects. The Cape Point Transect is shown in blue, the Cape Columbine Transect is shown in red, and the Oliphants River Estuary Transect is shown in violet. The dots indicate the locations where the xi and eta lines intersect.

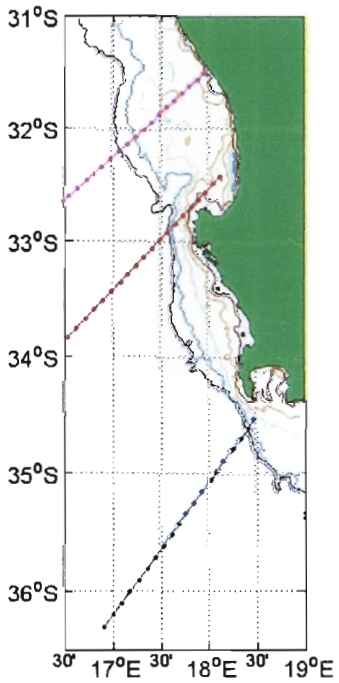

Figure 16: *The geographical locations of the Cape Point Transect (blue), the Cape Columbine Transect (red), and the Oliphants River Estuary Transect (violet).*

4.3 SELECTION OF VARIABLES

From the variables listed in Table 2, a decision on what variables to be focussed on had to be made in order to achieve the goals set out at the beginning of this section.
It was decided to select the variables: Salinity, Temperature, components of velocity along the xi and the eta axes.

The Salinity and Temperature were selected as they contained information about the physical state of the water. The components of velocity along the two axes were chosen as they provided the information regarding the dynamics of the water at the locations specified. These were essential if any study into the circulation within the domain was to be carried out.
For all these variables, the climatology averaged over a two-day time interval from the seven years, as well as the associated anomalies would be calculated.

4.4 CALCULATION DETAILS

For each variable, three different quantities had to be extracted and derived from the model data. They were, the instantaneous value, the climatology (as described in the previous section) and the anomaly.

The instantaneous values of a selected variable (eg: temperature, salinity) was extracted directly from the model output and saved in a matrix format. For 8 years of data averaged over 2 day intervals, at 20 horizontal points and for all 20 sigma layers, this procedure resulted in a matrix that had dimensions of 1440 by 20 by 20. This procedure was done for each of the selected variables at each of the transects.

In order to calculate the climatologies, the instantaneous matrices were utilized. For each data point, an average was found for the particular time interval of each year and stored as the climatology of that point for that particular time interval. In other words, an average value for the first 2-day interval of each year was found and stored as the climatology for the first 2-day interval. A climatology was then found for all 180 2-day intervals and stored in consecutive order. Once this was completed the procedure was repeated for the following gridpoint until climatologies for the entire year for each gridpoint was found. This resulted in a matrix that had dimensions of 180 by 20 by 20. This procedure was repeated for each of the selected variables for each of the three transects.

The anomalies, defined as being the difference between the instantaneous value and the climatological value, was calculated by subtracting the climatological value from the instantaneous value for each 2-day time interval, at each point, for the 8 years of data. This resulted in a matrix that had dimensions of 1440 by 20 by 20. This procedure was repeated for each of the selected variables for each of the three transects.

Once, these three large matrices were calculated, it became necessary to interpolate them onto a regular grid to allow them to be examined with greater ease. The matrices were then interpolated onto a regular grid using a Spline Method. Since this method can be used as both an interpolation and extrapolation tool, data obtained where the model was not defined, such as underground or on land, where removed from the resulting dataset.

The following figure is a flow diagram illustrating the process followed to produce the final matrices from the model output.

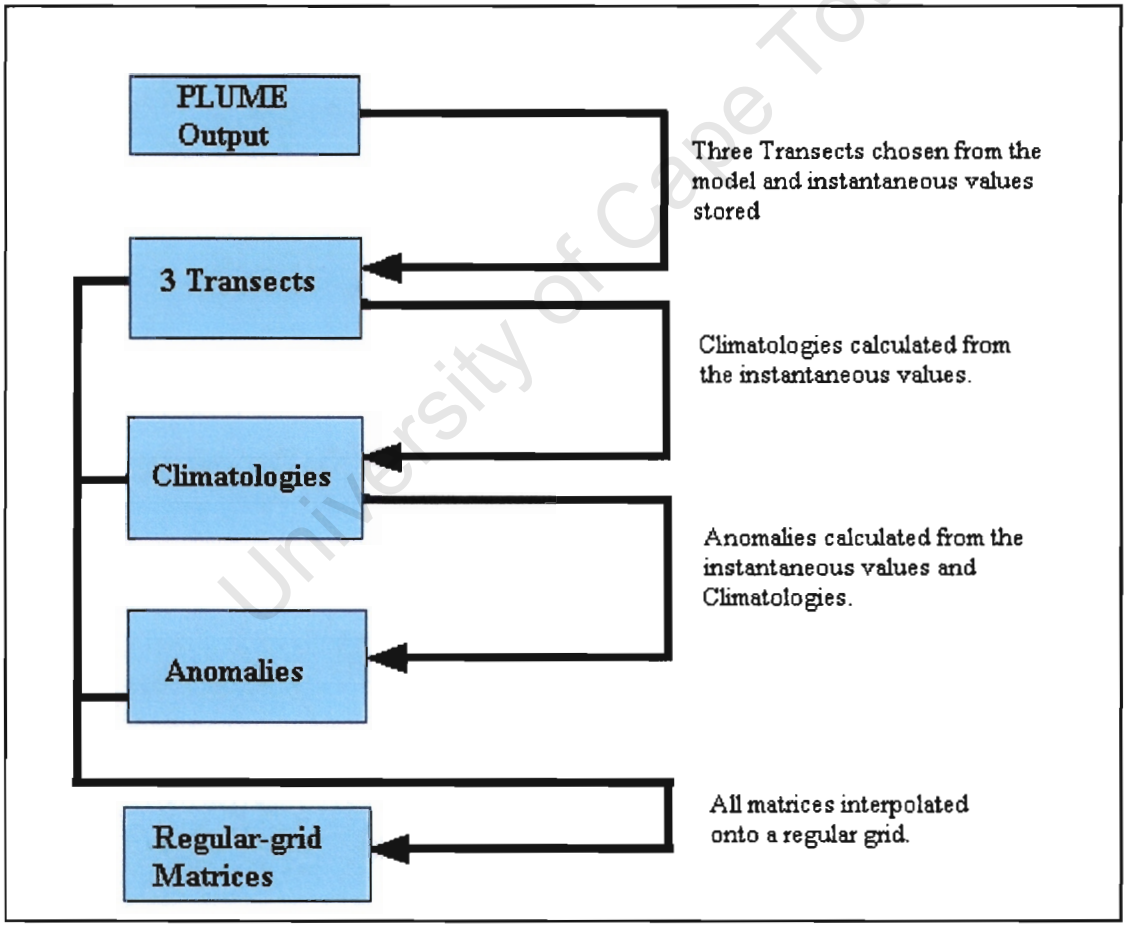

Figure 17: *Flow diagram illustrating the calculation procedures.*

5 RESULTS

This section presents the results that were obtained from the calculations detailed in the previous section. All results are presented for the sake of completeness and they are discussed in the following Section 6.

For each of the four variables (temperature, salinity, U and V) a timeseries of the climatology at an inshore and an offshore point are presented. These are followed by Hovmuller Diagrams of the climatology and anomaly at each of the three transects. This procedure is carried out for the surface data, and then for data at 200m below the surface.

5.1 TEMPERATURE

5.1.1 RESULTS AT THE SURFACE

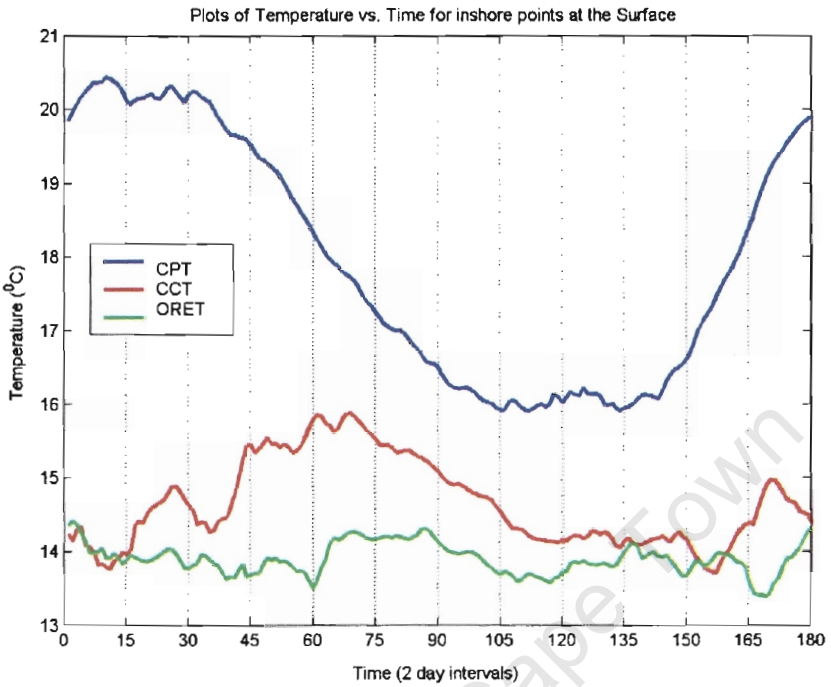

Figure 18: *Timeseries of Temperature Climatology for the inshore locations at the surface.*

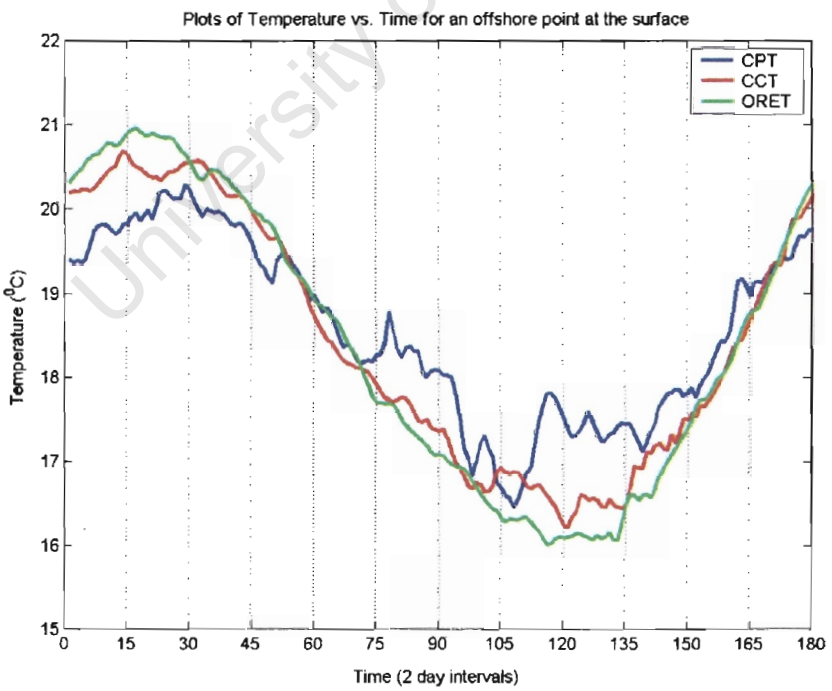

Figure 19: *Timeseries of Temperature Climatology for the offshore locations at the surface*

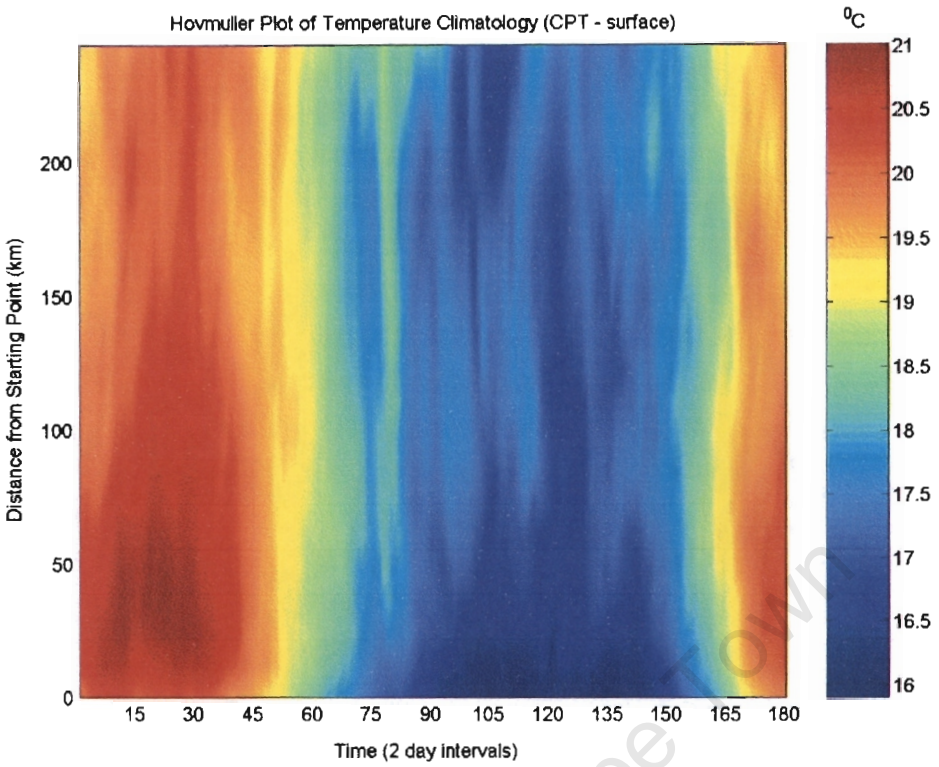

Figure 20: *Hovmuller Plot of Temperature Climatology along the surface of the Cape Point Transect*

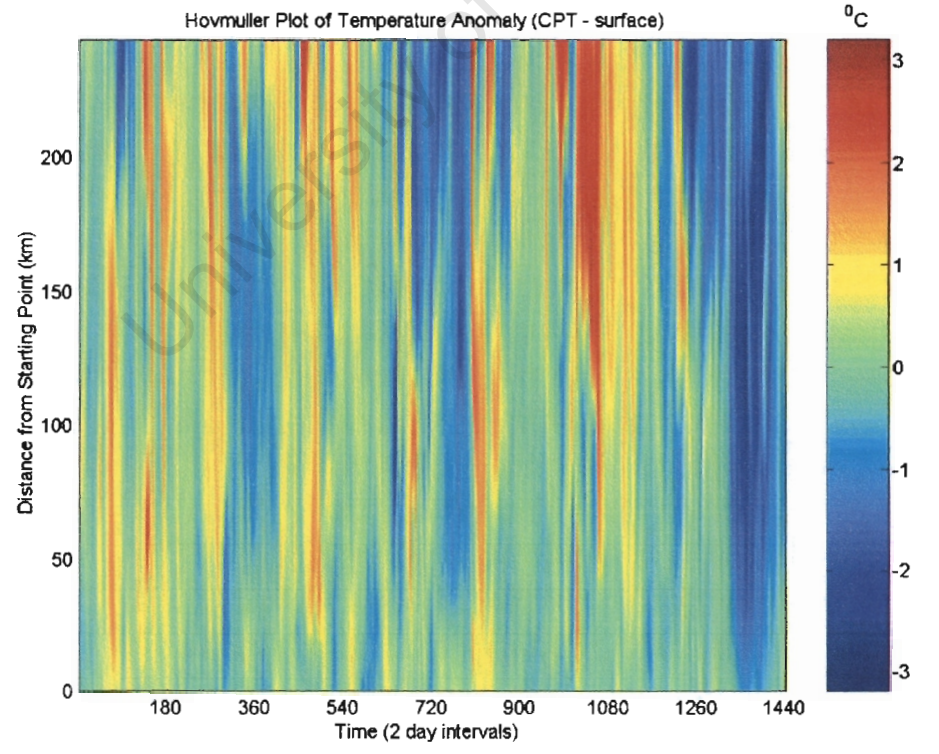

Figure 21: *Hovmuller Plot of Temperature Anomalies along the surface of the Cape Point Transect*

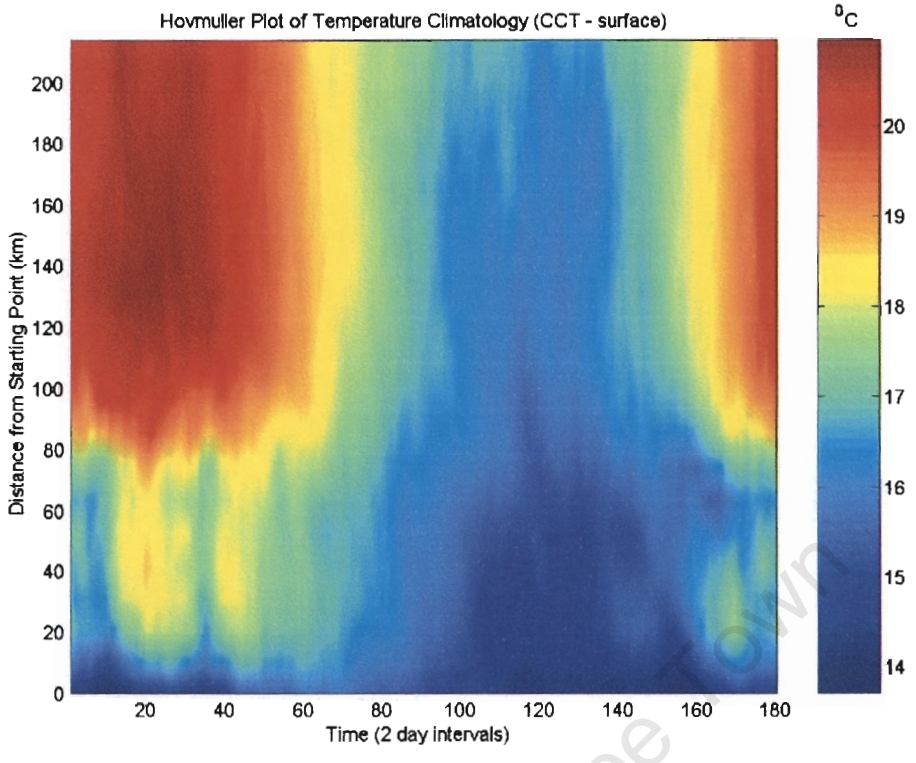

Figure 22: *Hovmuller Plot of Temperature Climatology along the surface of the Cape Columbine Transect*

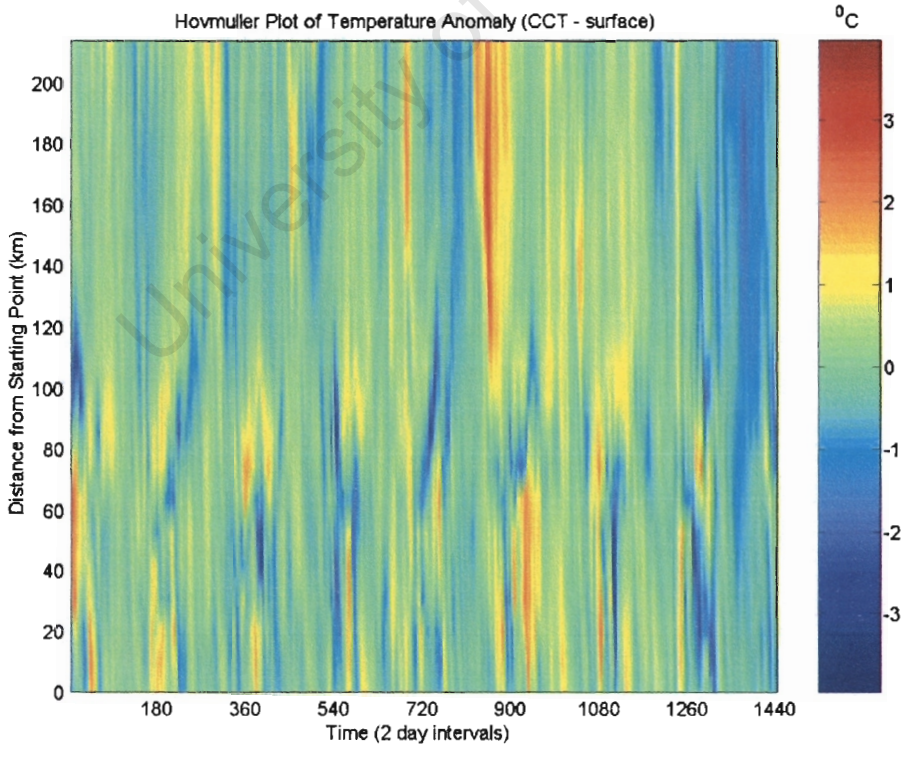

Figure 23: *Hovmuller Plot of Temperature Anomalies along the surface of the Cape Columbine Transect*

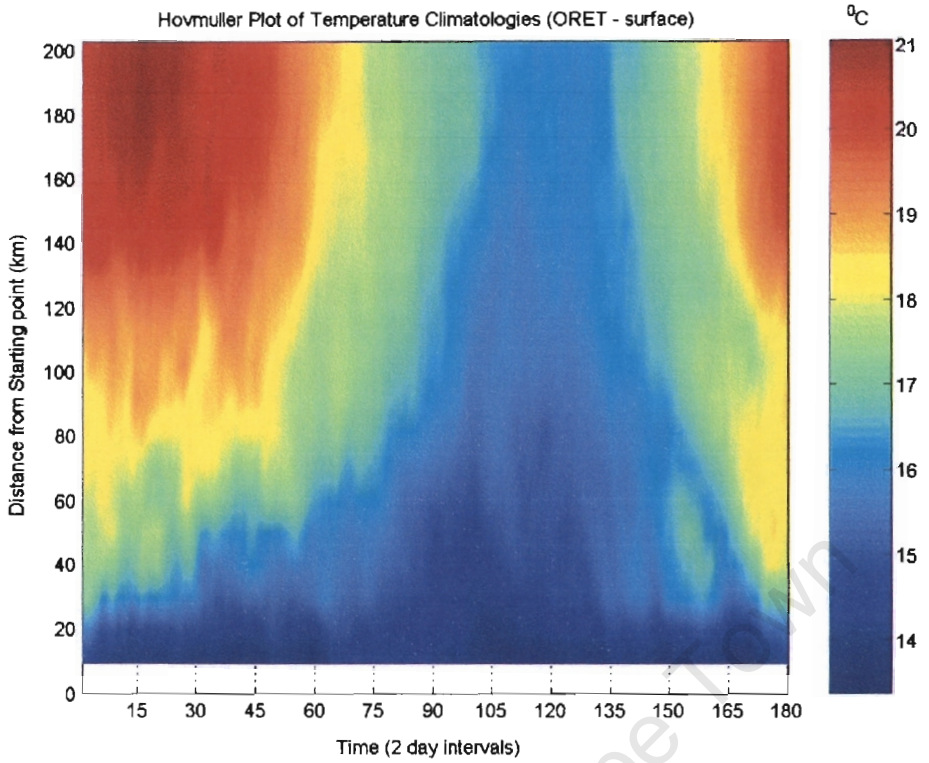

Figure 24: *Hovmuller Plot of Temperature Climatology along the surface of the Oliphants River Estuary Transect*

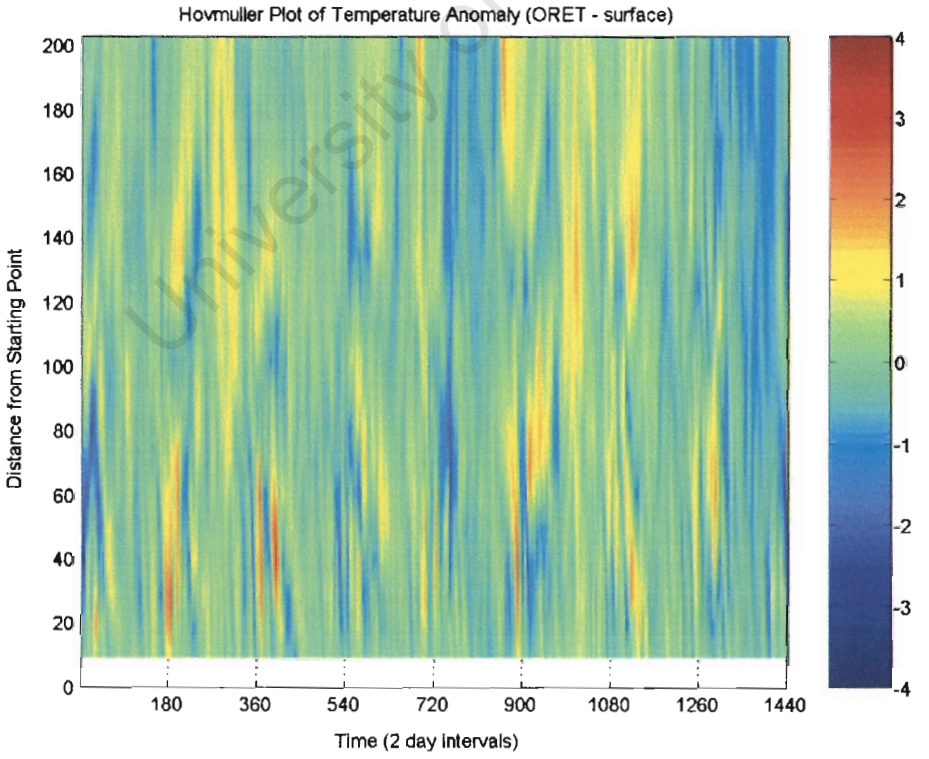

Figure 25: *Hovmuller Plot of the Temperature Anomalies along the surface of the Oliphants River Estuary Transect*

5.1.2 RESULTS AT 200M DEPTH

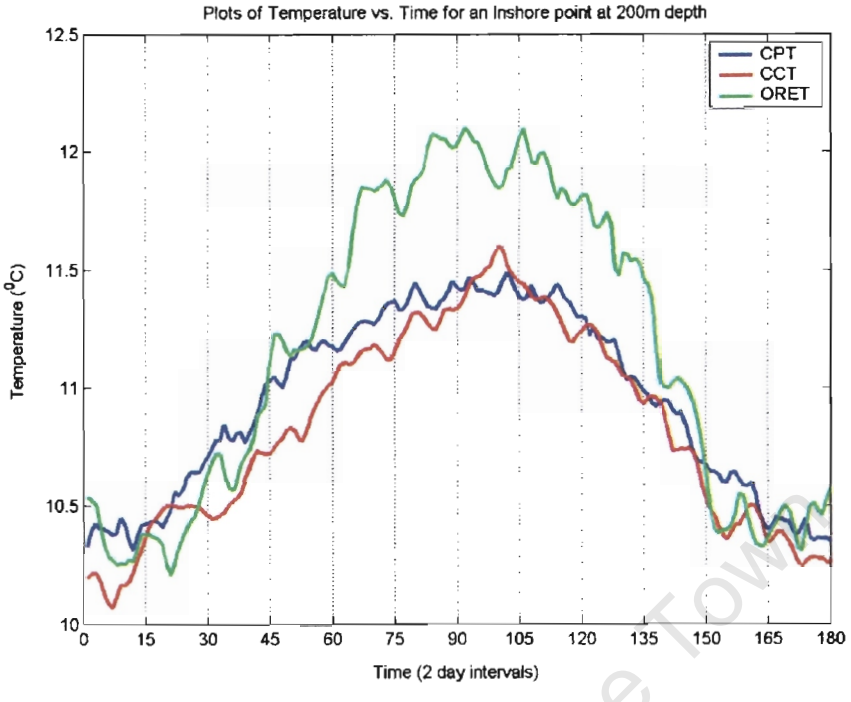

Figure 26: *Timeseries of Temperature Climatology for the inshore locations at a depth of 200m.*

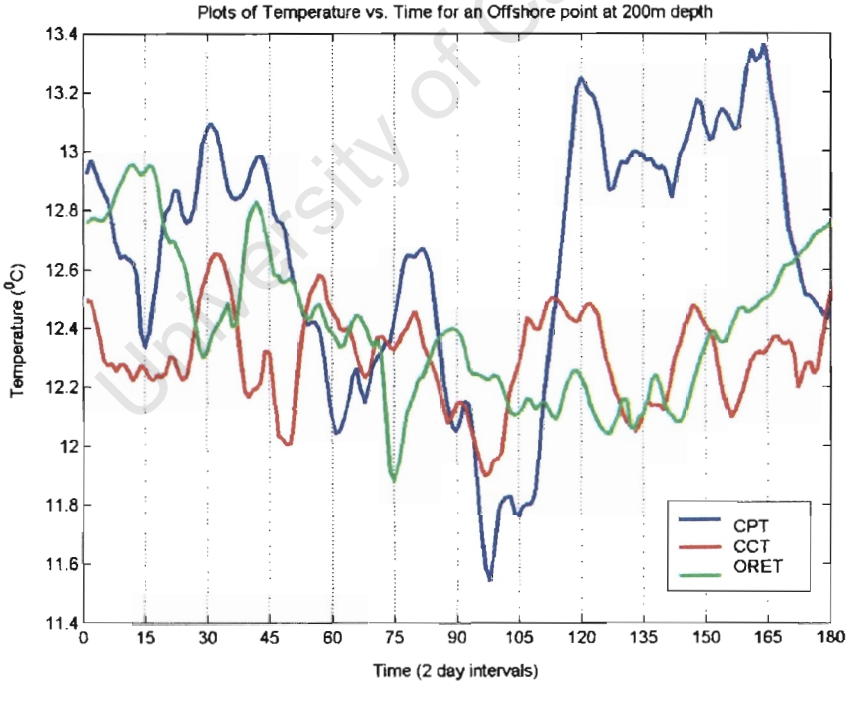

Figure 27: *Timeseries of Temperature Climatology for the offshore locations at a depth of 200m*

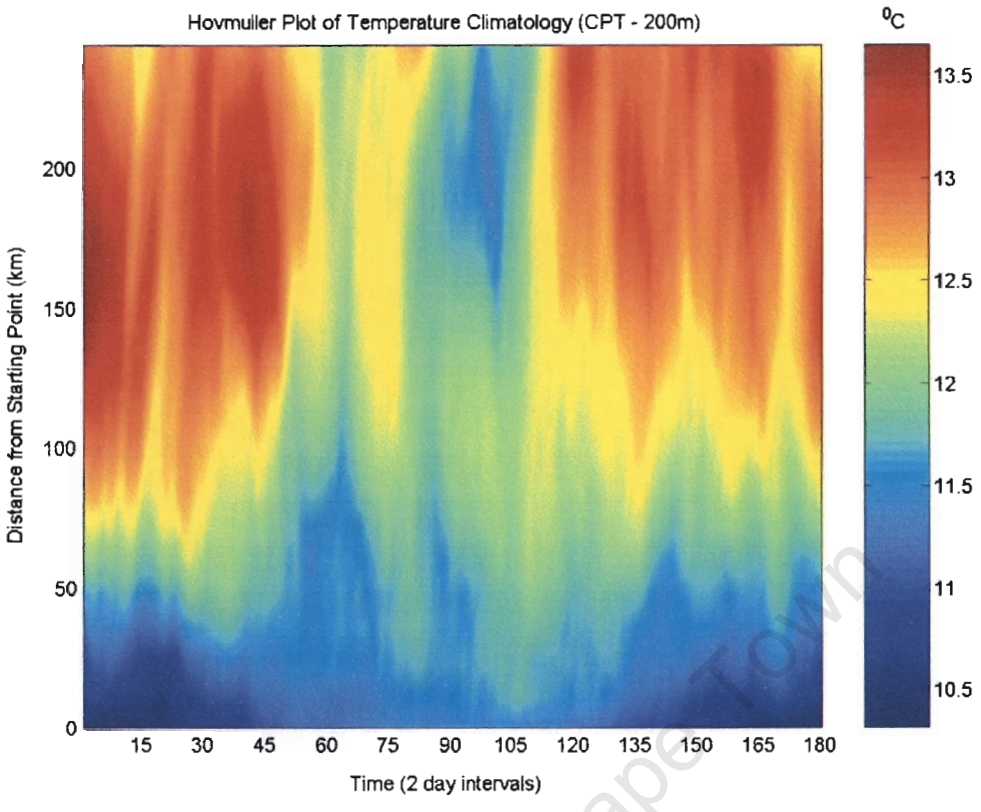

Figure 28: *Hovmuller Plot of Temperature Climatology at 200m deep along the Cape Point Transect*

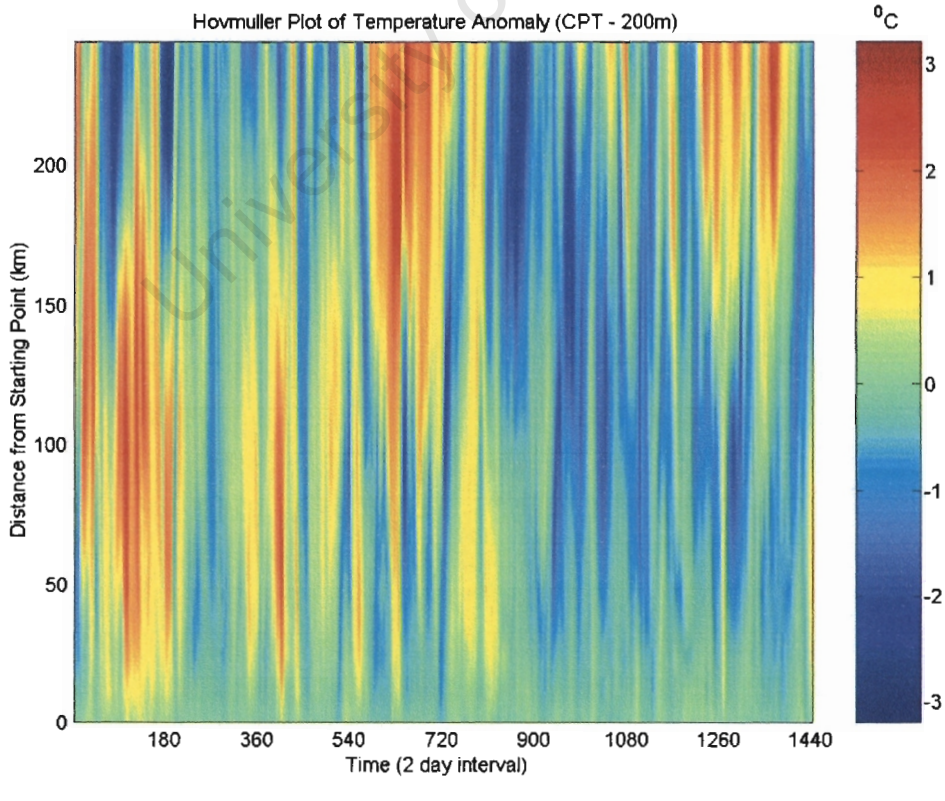

Figure 29: *Hovmuller Plot of Temperature Anomalies at 200m deep along the Cape Point Transect*

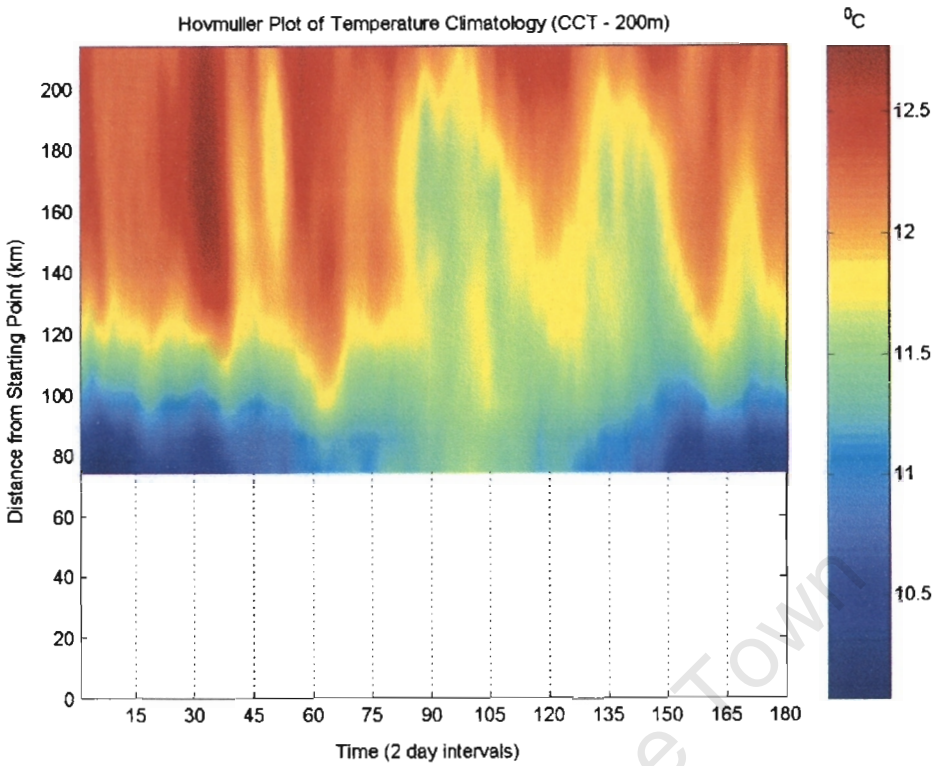

Figure 30: *Hovmuller Plot of Temperature Climatology at 200m deep along the Cape Columbine Transect*

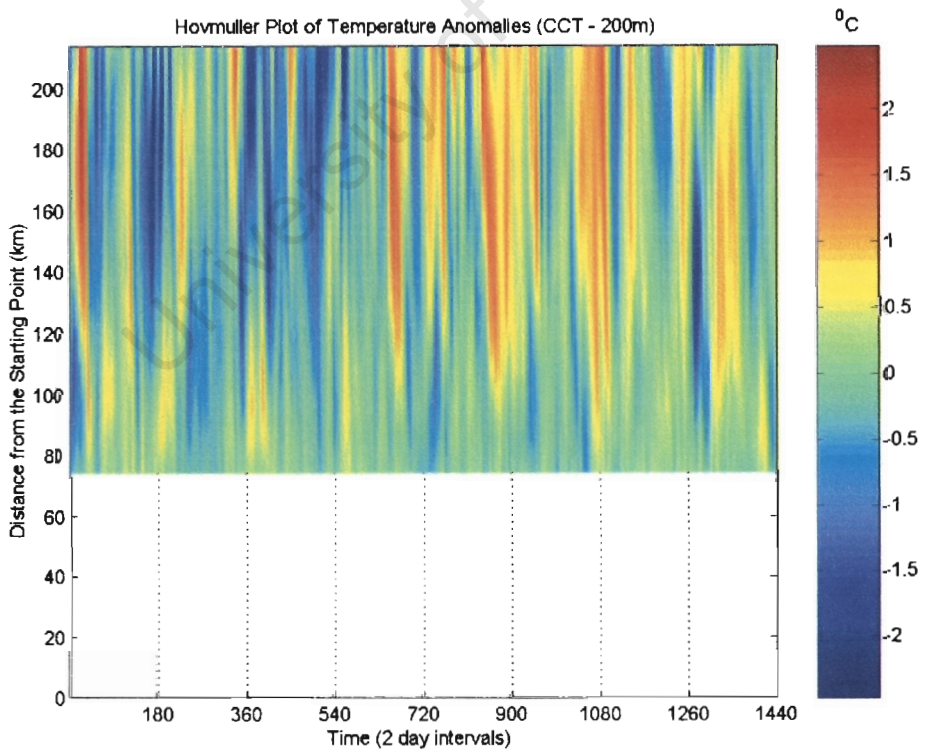

Figure 31: *Hovmuller Plot of Temperature Anomalies at 200m deep along the Cape Columbine Transect*

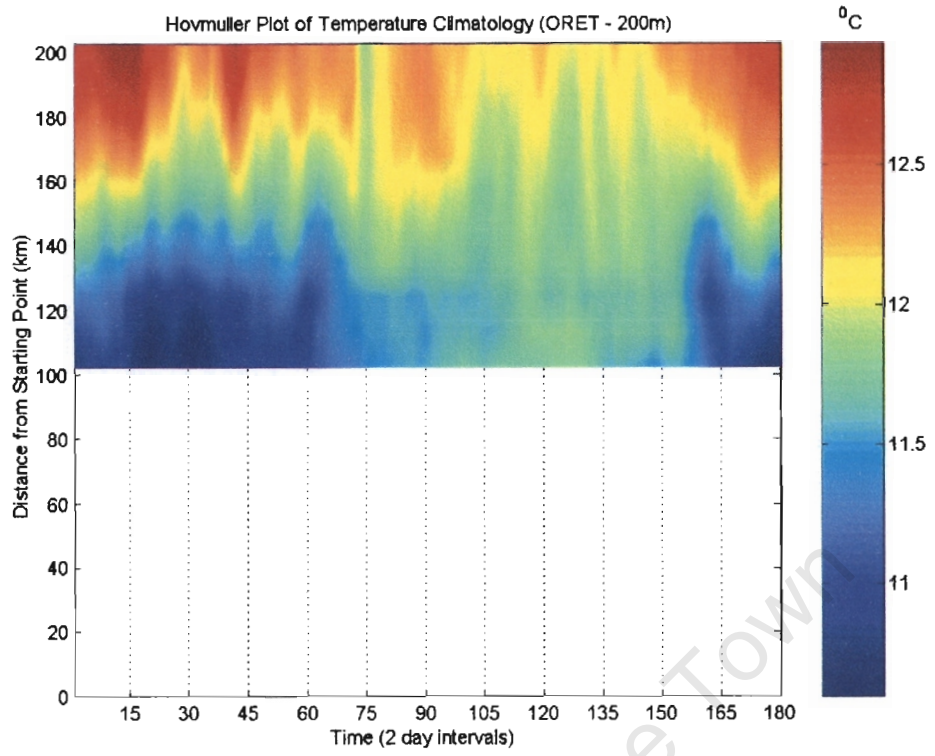

Figure 32: *Hovmuller Plots of Temperature Climatology at 200m deep along the Oliphants River Estuary Transect*

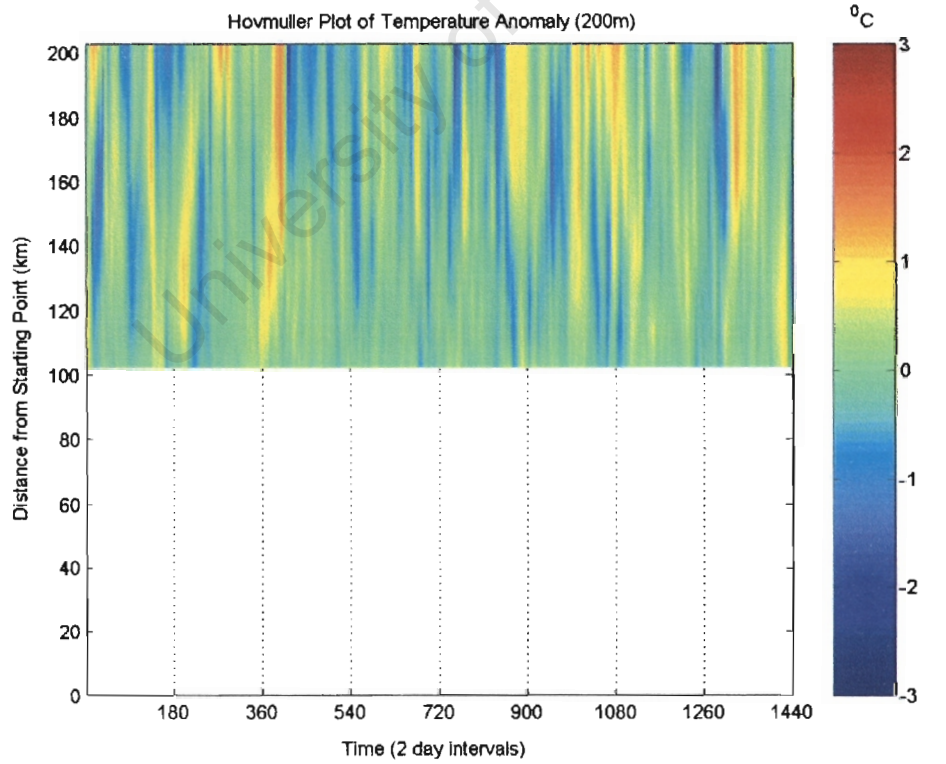

Figure 33: *Hovmuller Plot of Temperature Anomalies at 200m deep along the Oliphants River Estuary Transect*

5.2 SALINITY

5.2.1 RESULTS AT THE SURFACE

Figure 34: *Timeseries of Salinity Climatology for the inshore locations at the surface*

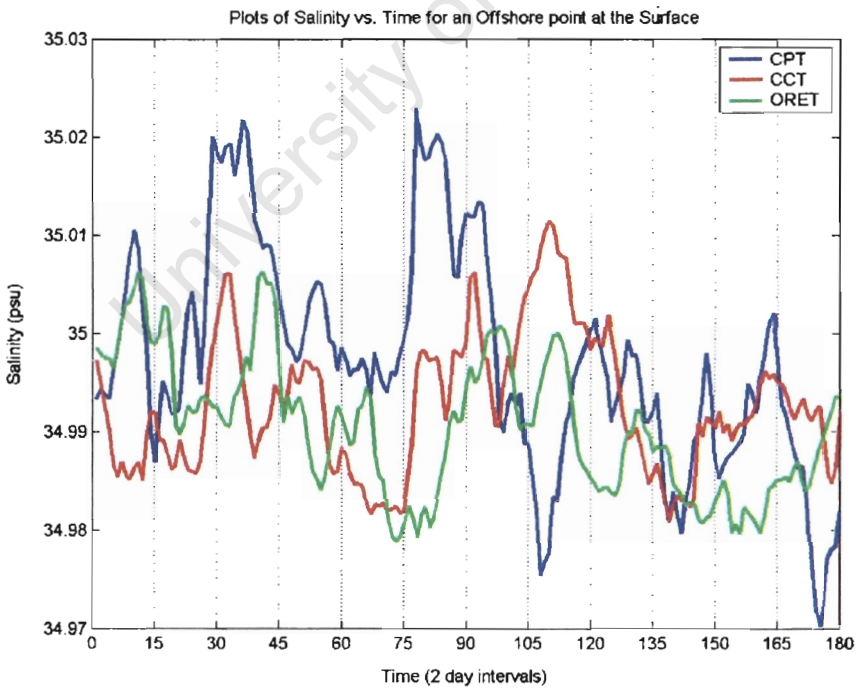

Figure 35: *Timeseries of Salinity Climatology for the offshore locations at the surface*

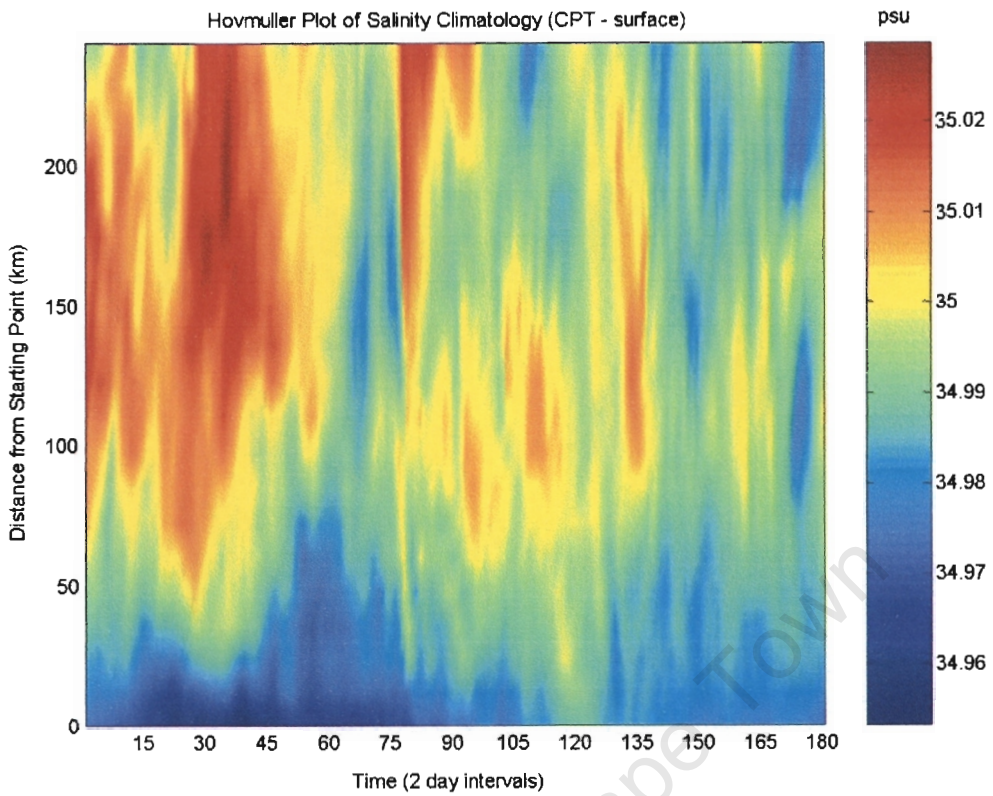

Figure 36: *Hovmuller Plot of Salinity Climatology along the surface of the Cape Point Transect*

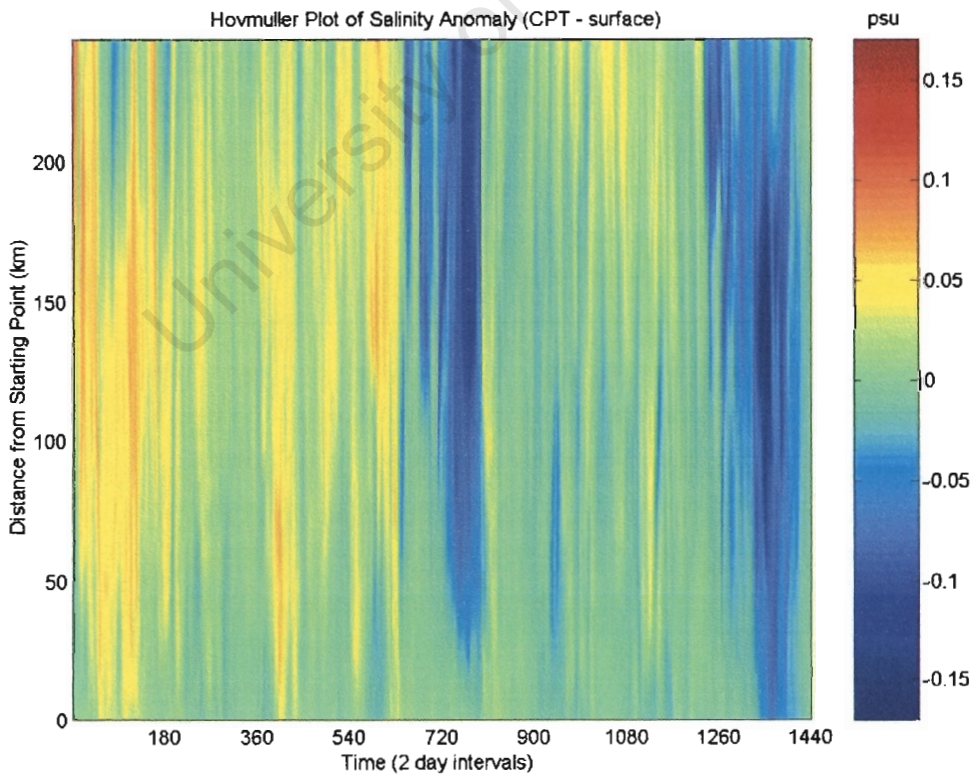

Figure 37: *Hovmuller Plot of Salinity Anomalies along the surface of the Cape Point Transect*

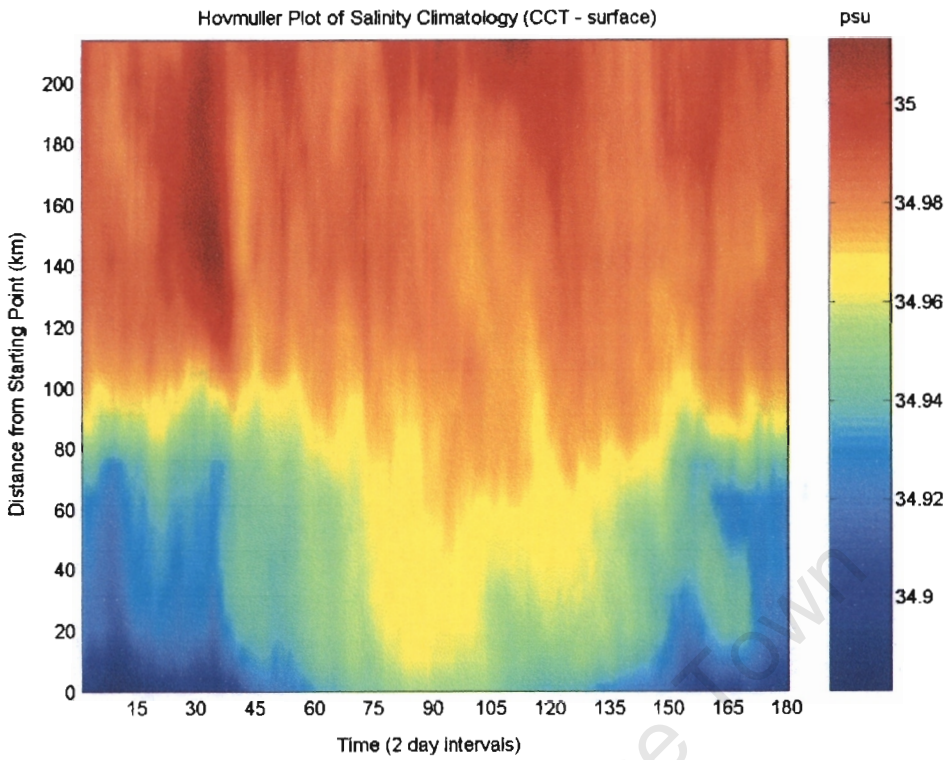

Figure 38: *Hovmuller Plot of Salinity Climatology along the surface of the Cape Columbine Transect*

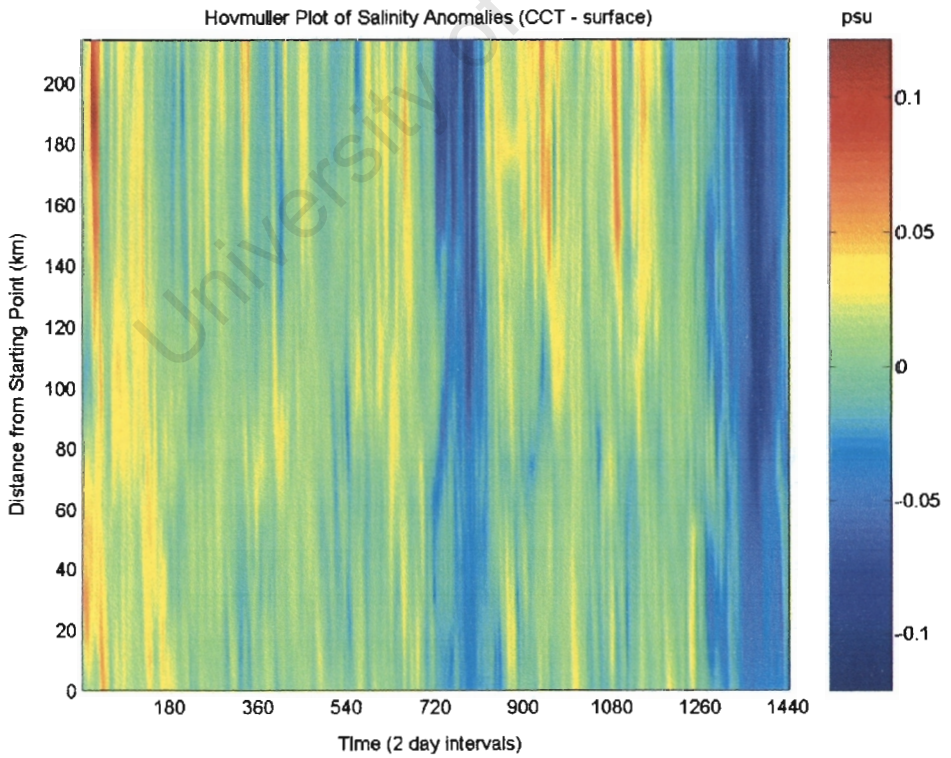

Figure 39: *Hovmuller Plot of Salinity Anomalies along the surface of the Cape Columbine Transect*

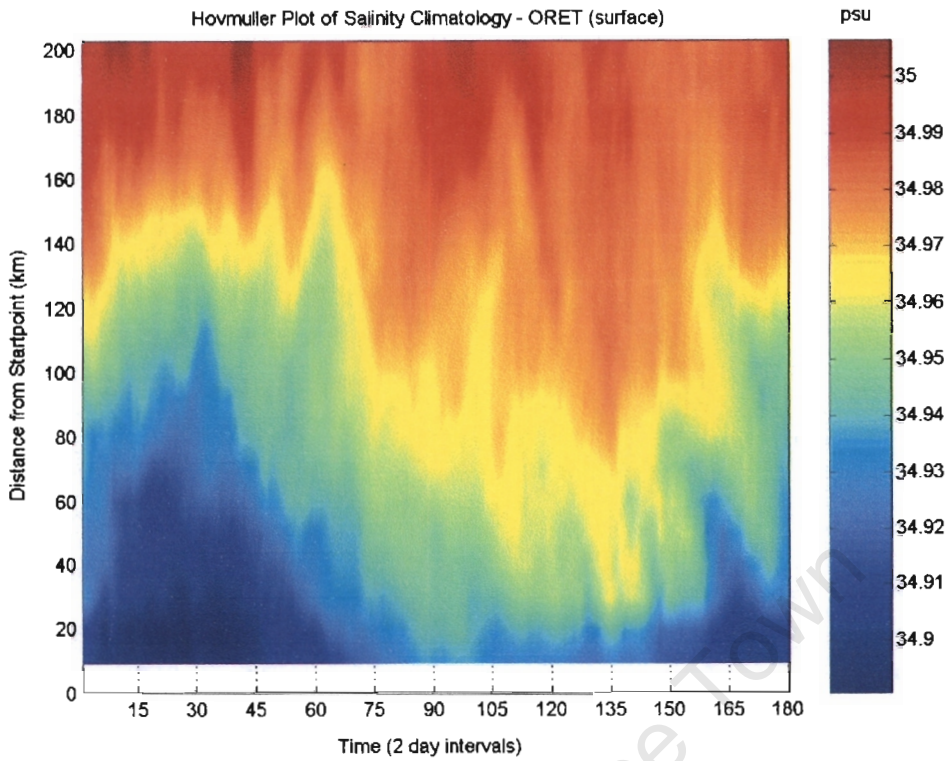

Figure 40: *Hovmuller Plot of Salinity Climatology along the surface of the Oliphants River Estuary Transect*

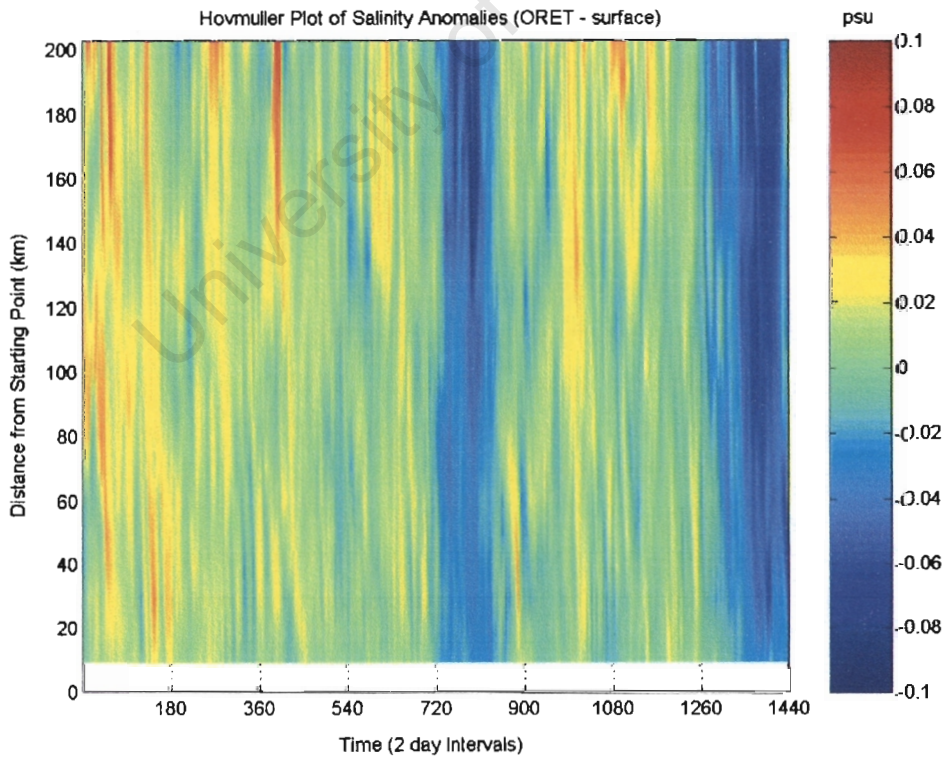

Figure 41: *Hovmuller Plot of Salinity Anomalies along the surface of the Oliphants River Estuary Transect*

5.2.2 RESULTS AT 200M DEEP

Figure 42: *Timeseries of Salinity Climatology for the inshore locations at a depth of 200m*

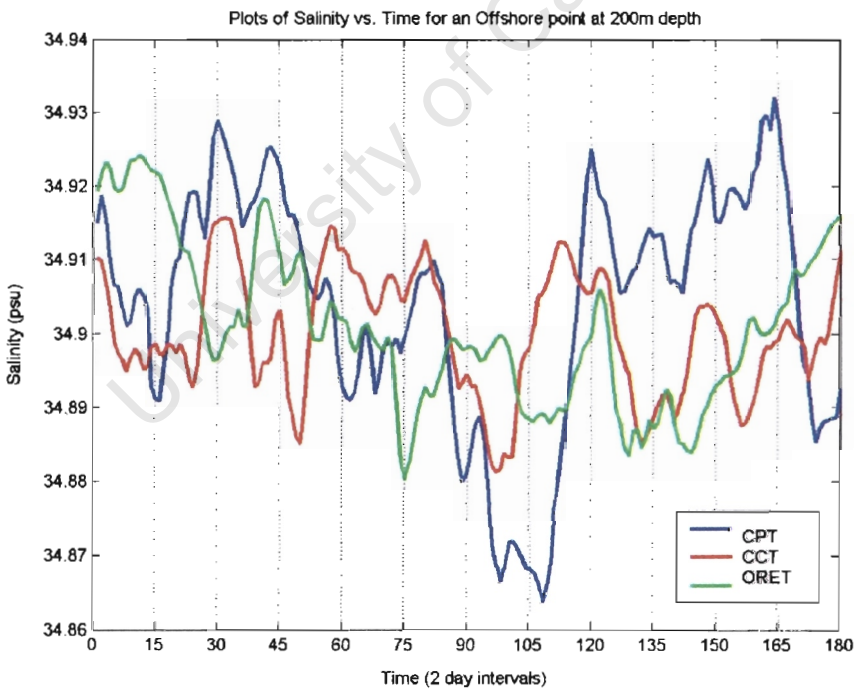

Figure 43: *Timeseries of Salinity Climatology for the offshore locations at a depth of 200m*

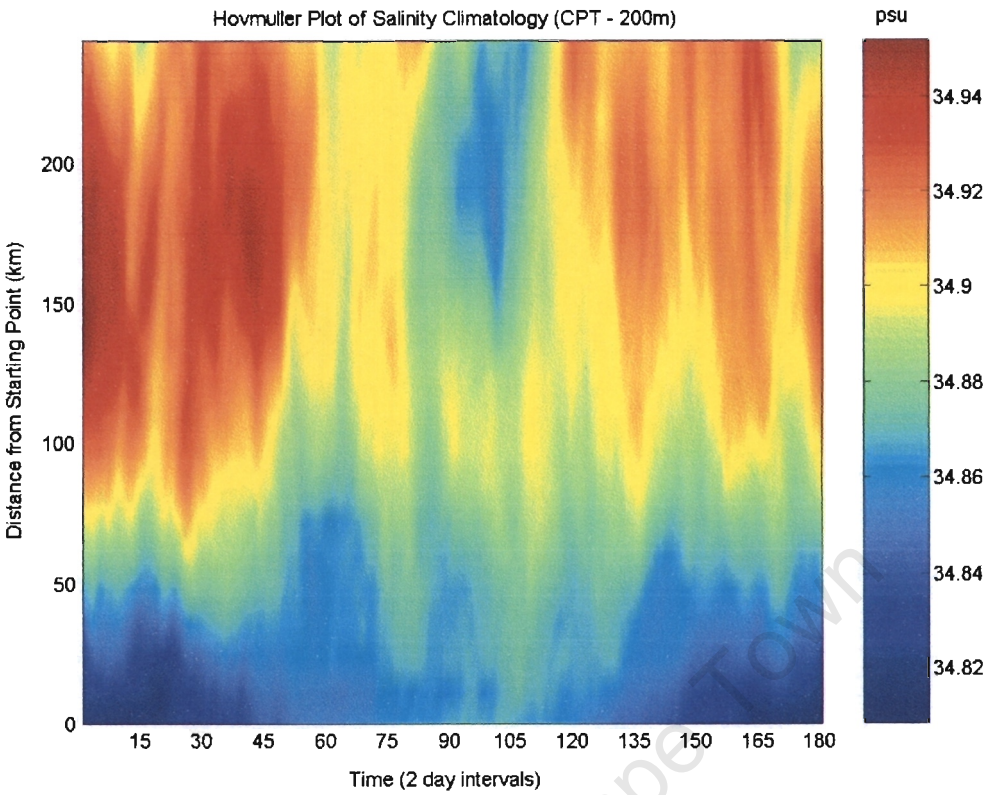

Figure 44: *Hovmuller Plot of Salinity Climatology at 200m deep along the Cape Point Transect*

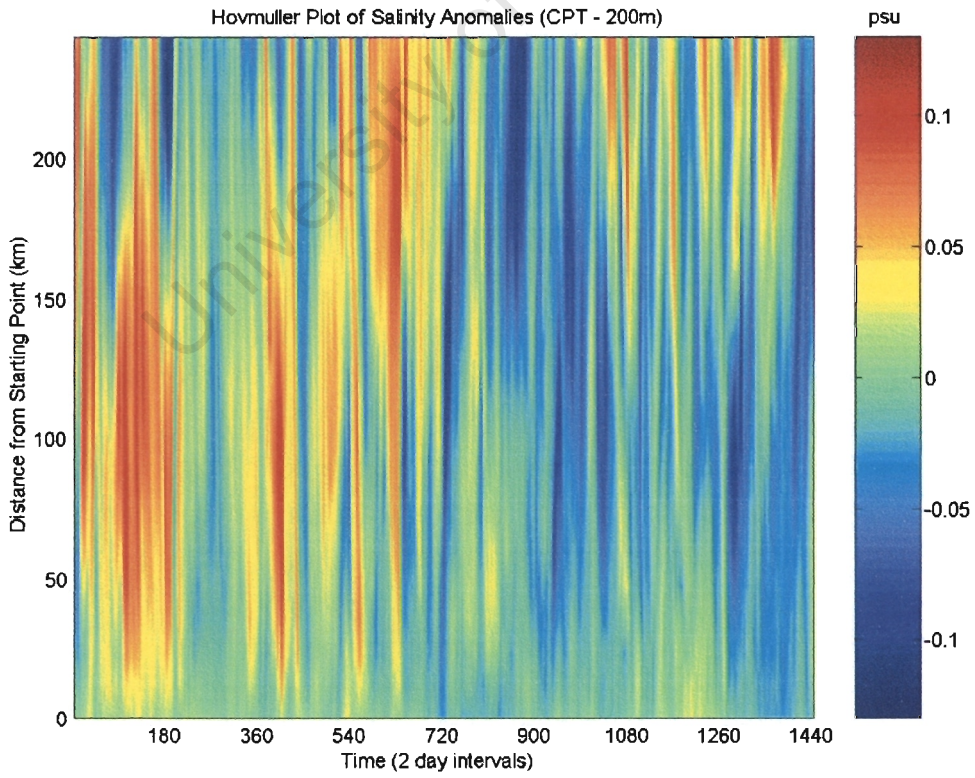

Figure 45: *Hovmuller Plot of Salinity Anomalies at 200m deep along the Cape Point Transect*

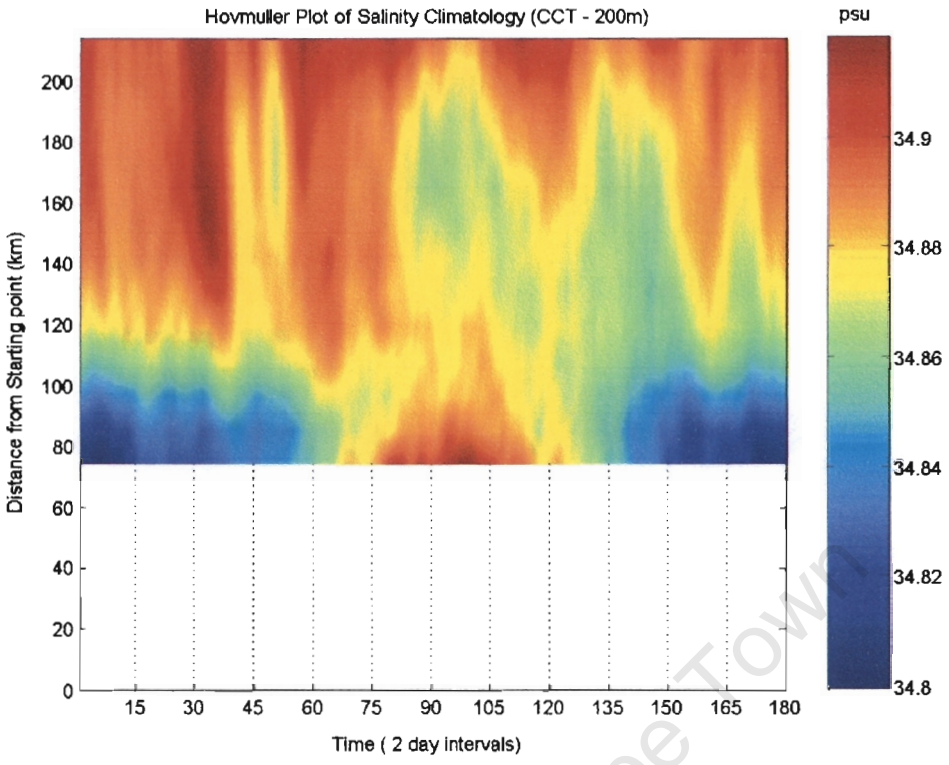

Figure 46: *Hovmuller Plot of Salinity Climatology at 200m deep along the Cape Columbine Transect*

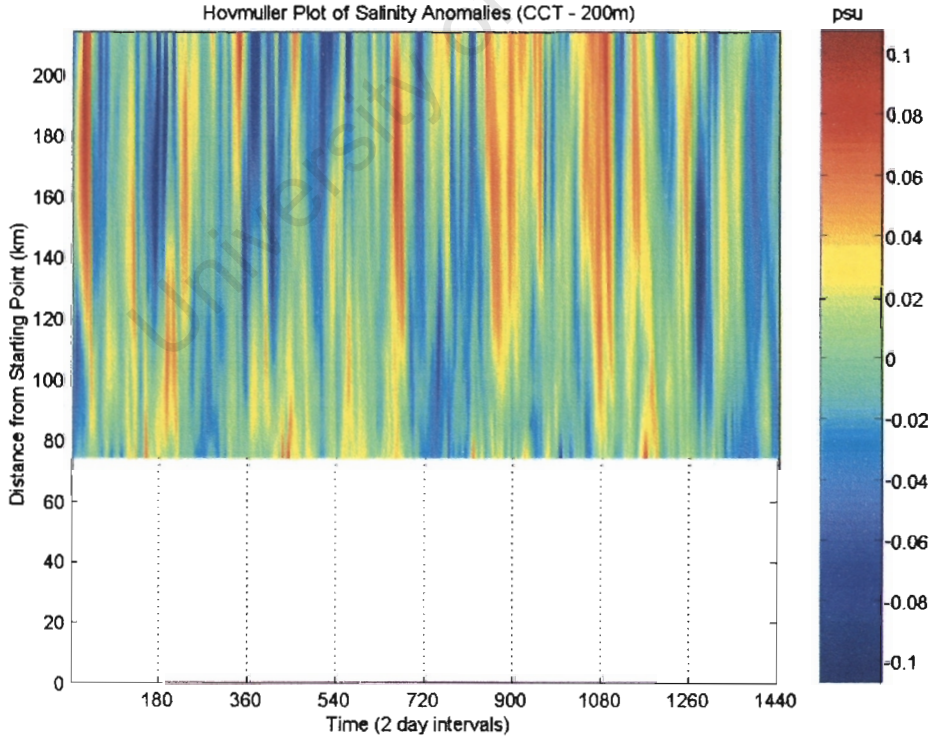

Figure 47: *Hovmuller Plot of Salinity Anomalies at 200m deep along the Cape Columbine Transect*

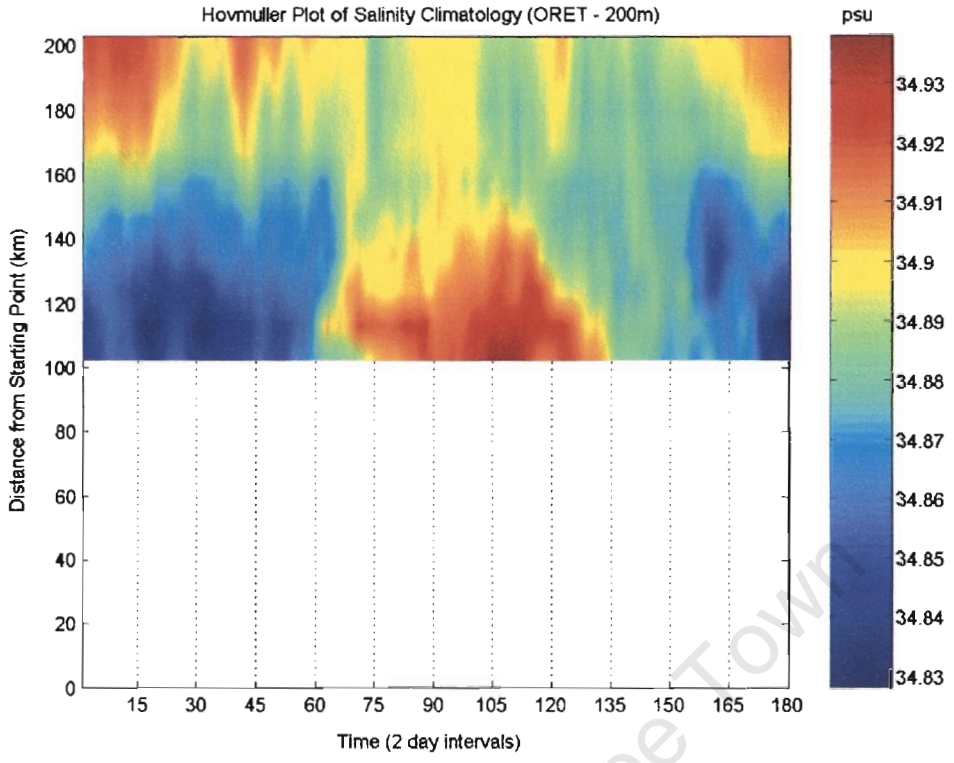

Figure 48: *Hovmuller Plot of Salinity Climatology at 200m deep along the Oliphants River Estuary Transect*

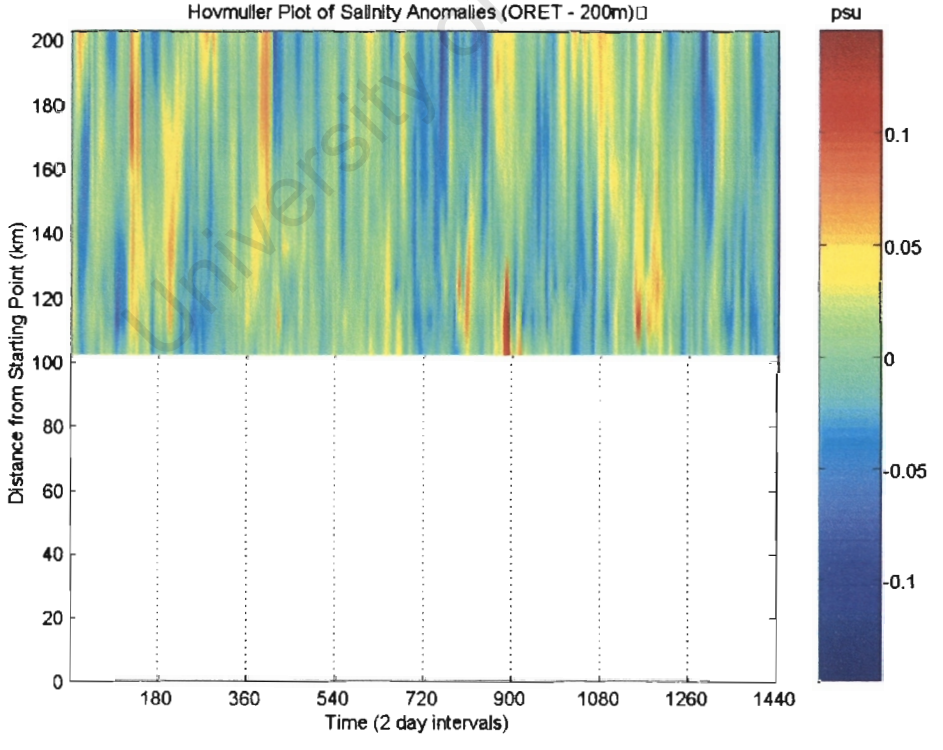

Figure 49: *Hovmuller Plot of Salinity Anomalies at 200m deep along the Oliphants River Estuary Transect*

5.3 U VELOCITY (POSITIVE INDICATES OFFSHORE FLOW)

5.3.1 RESULTS AT THE SURFACE

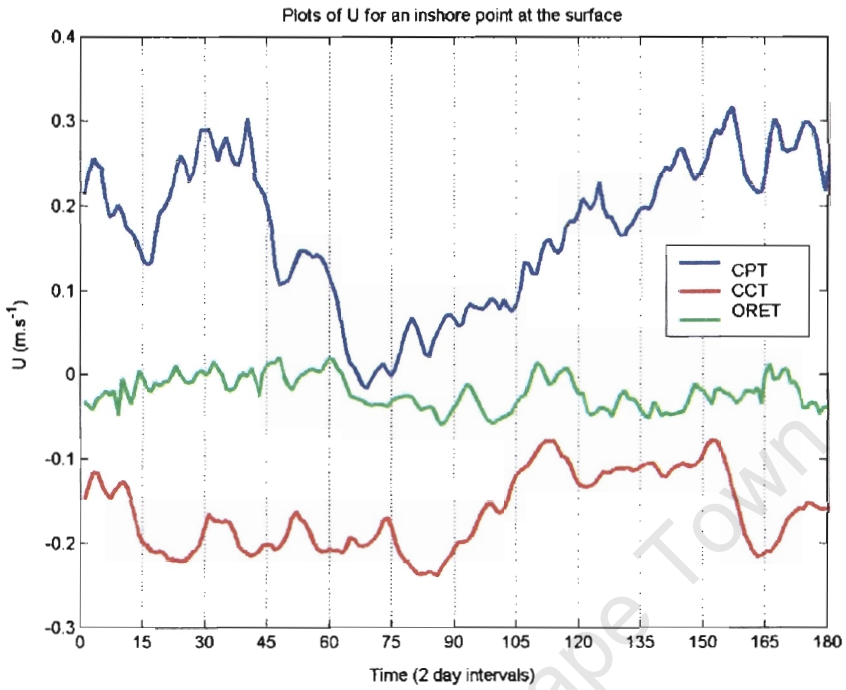

Figure 50: *Timeseries of U Climatology for the inshore locations at the surface*

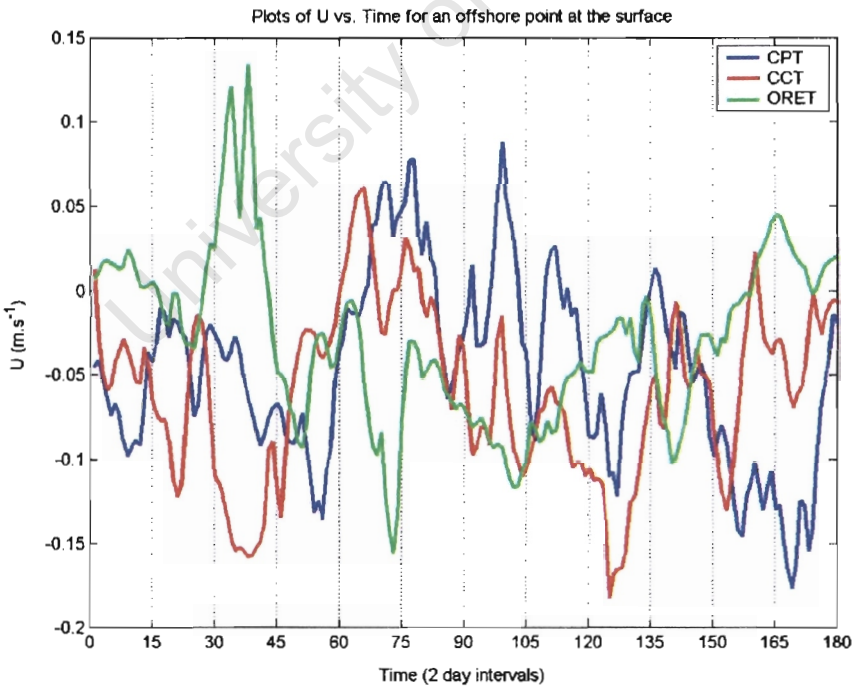

Figure 51: *Timeseries of U Climatology for the offshore locations at the surface*

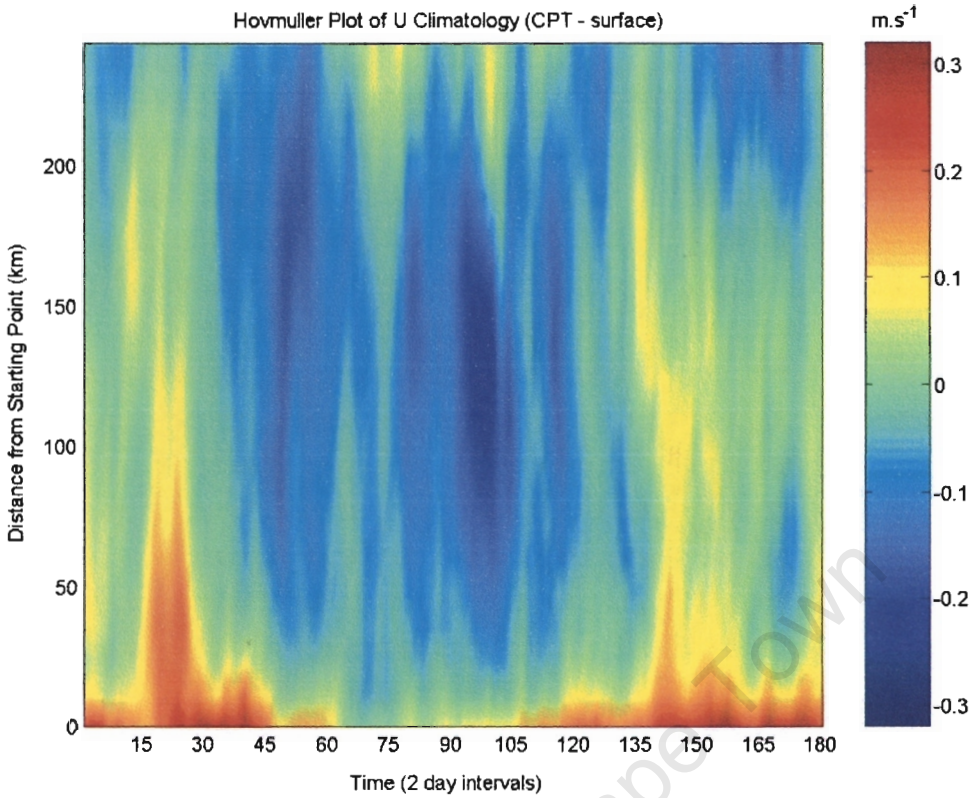

Figure 52: *Hovmuller Plot of U Climatology along the surface of the Cape Point Transect*

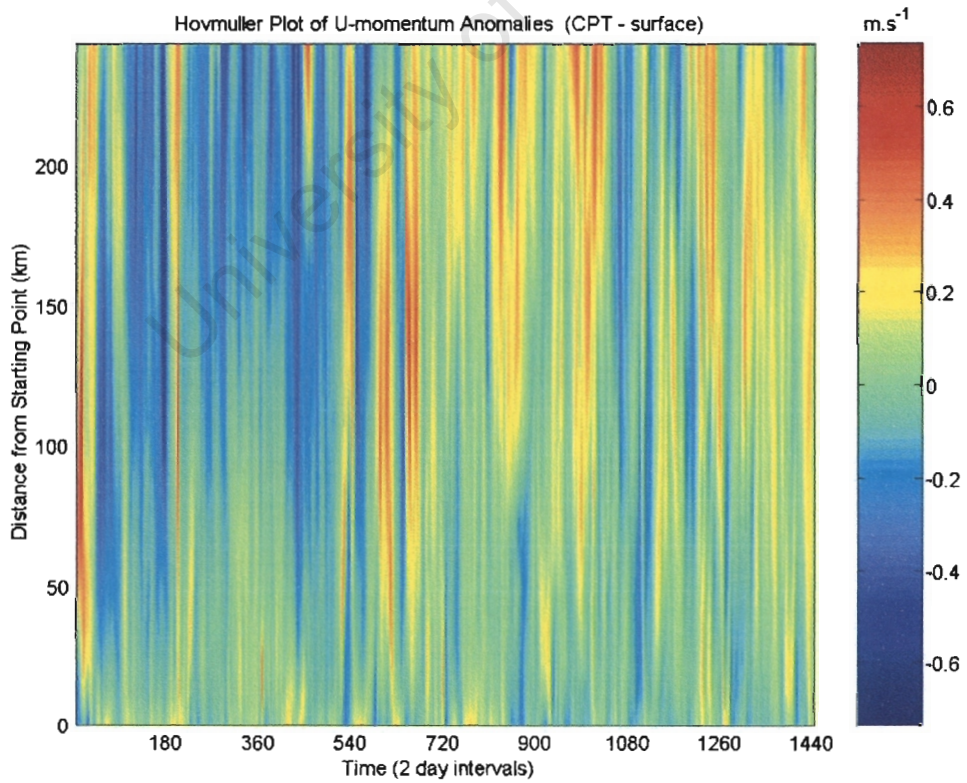

Figure 53: *Hovmuller Plot of U Anomalies along the surface of the Cape Point Transect*

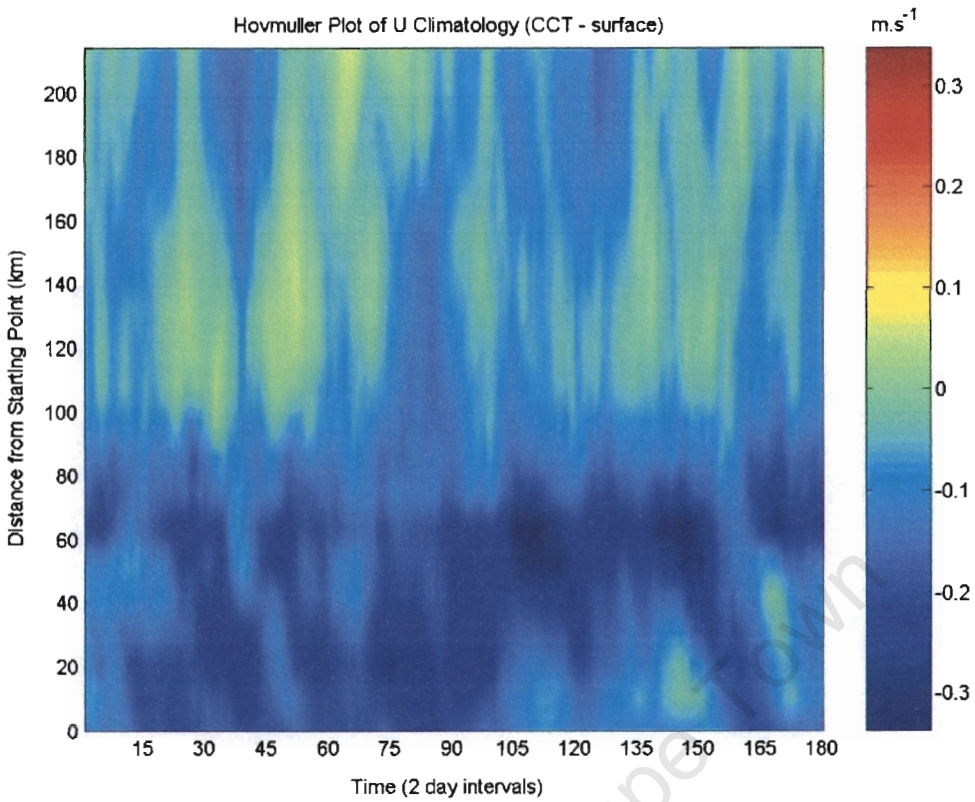

Figure 54: *Hovmuller Plot of U Climatology along the surface of the Cape Columbine Transect*

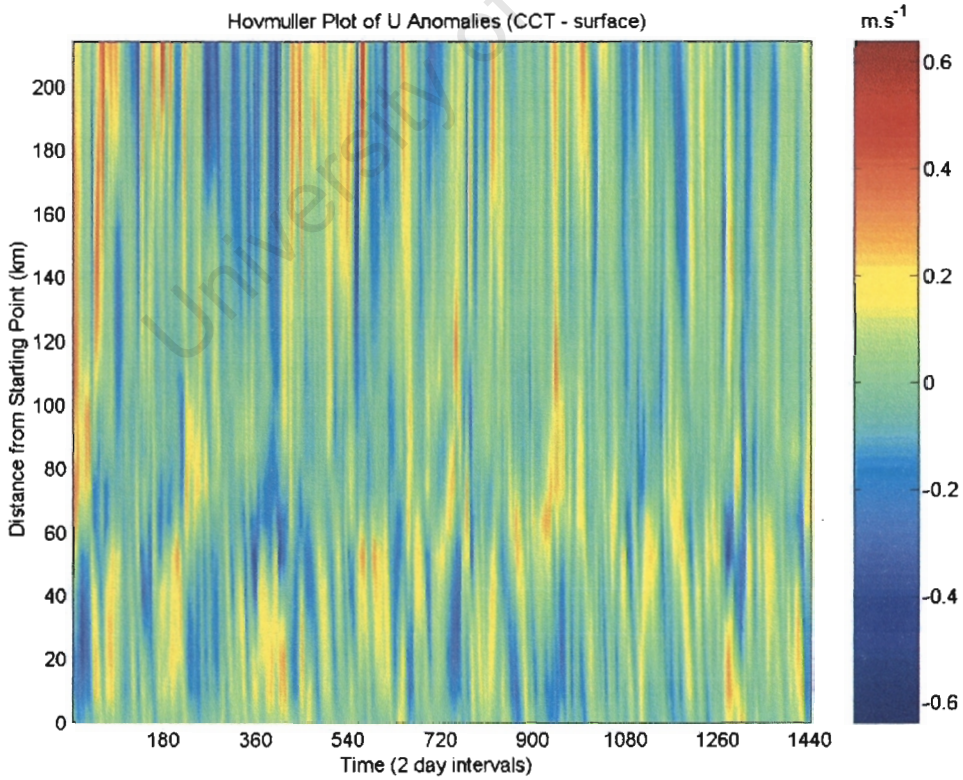

Figure 55: *Hovmuller Plot of U Anomalies along the surface of the Cape Columbine Transect*

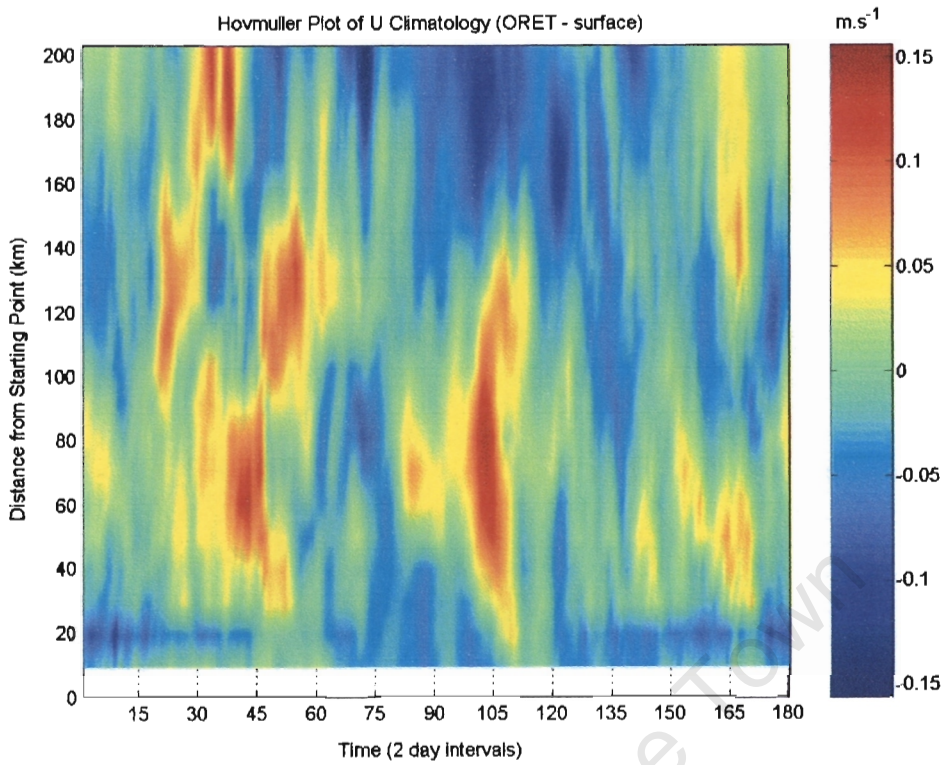

Figure 56: *Hovmuller Plot of U Climatology along the surface of the Oliphants River Estuary Transect*

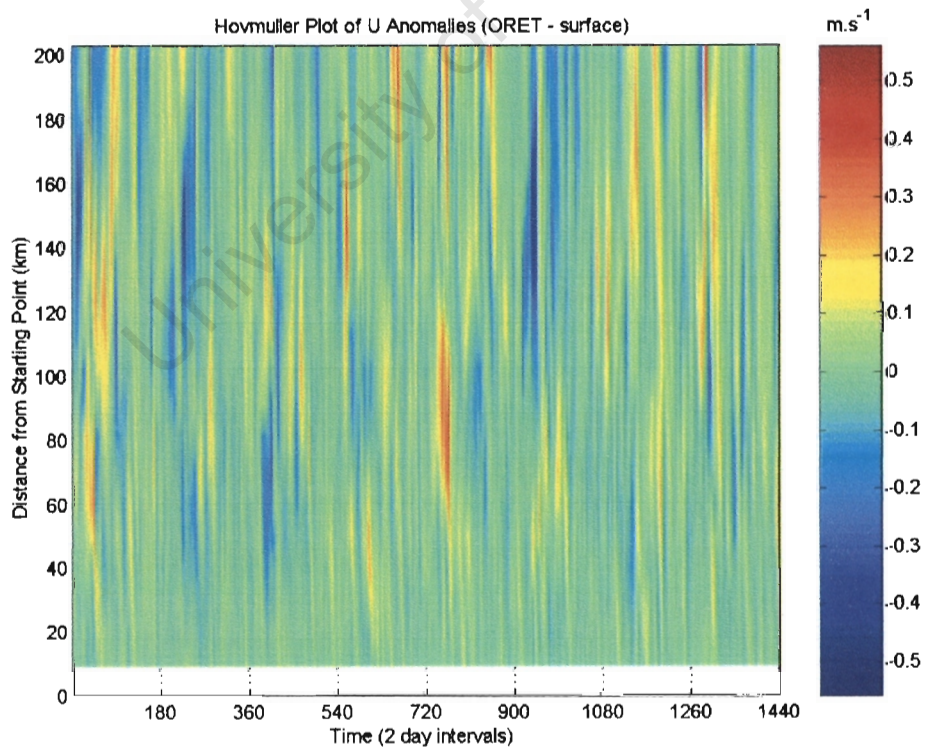

Figure 57: *Hovmuller Plot of U Anomalies along the surface of the Oliphants River Estuary Transect*

5.3.2 RESULTS AT 200M DEPTH

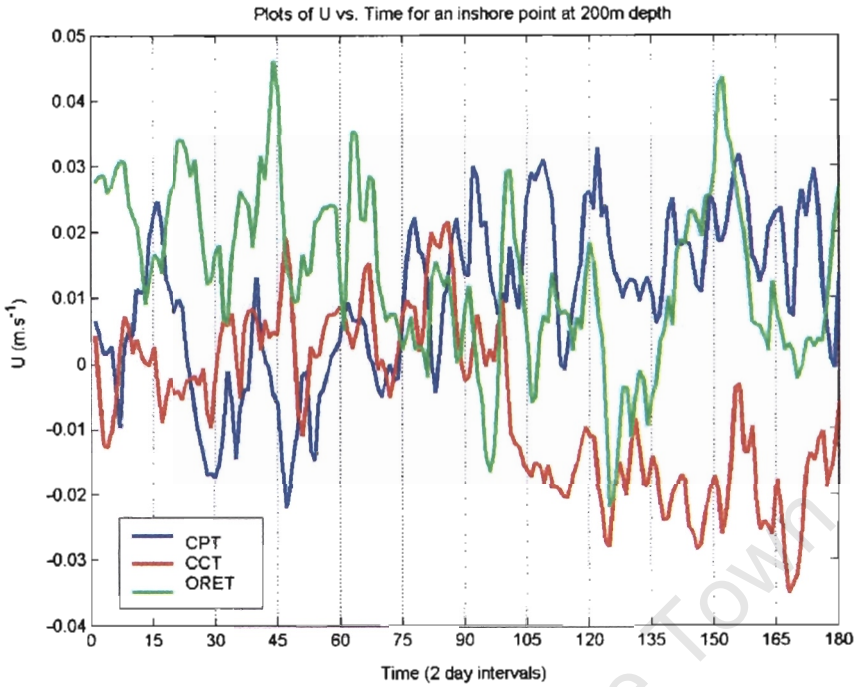

Figure 58: *Timeseries of U Climatology for the inshore locations at 200m deep*

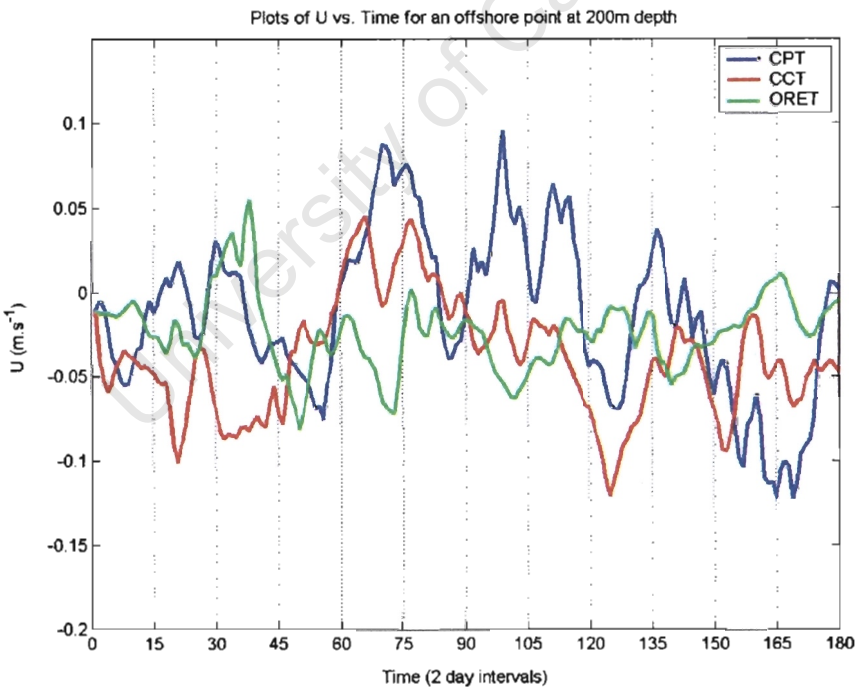

Figure 59: *Timeseries of U Climatology for the offshore locations at 200m deep*

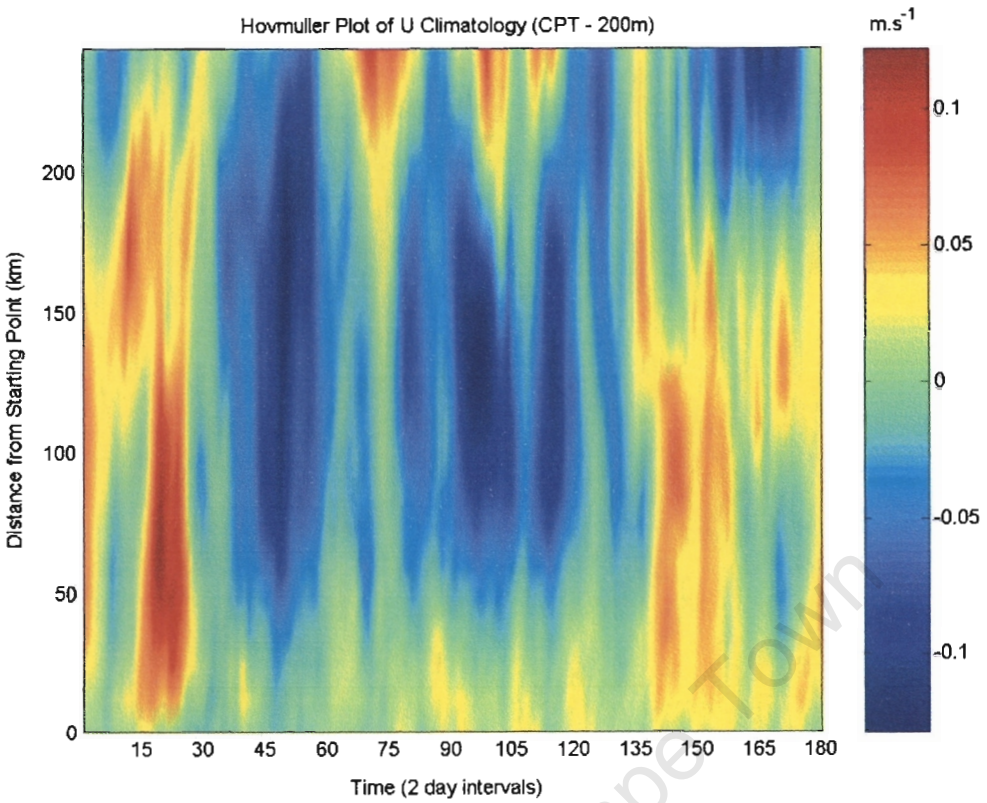

Figure 60: *Hovmuller plot of U Climatology at 200m deep along the Cape Point Transect*

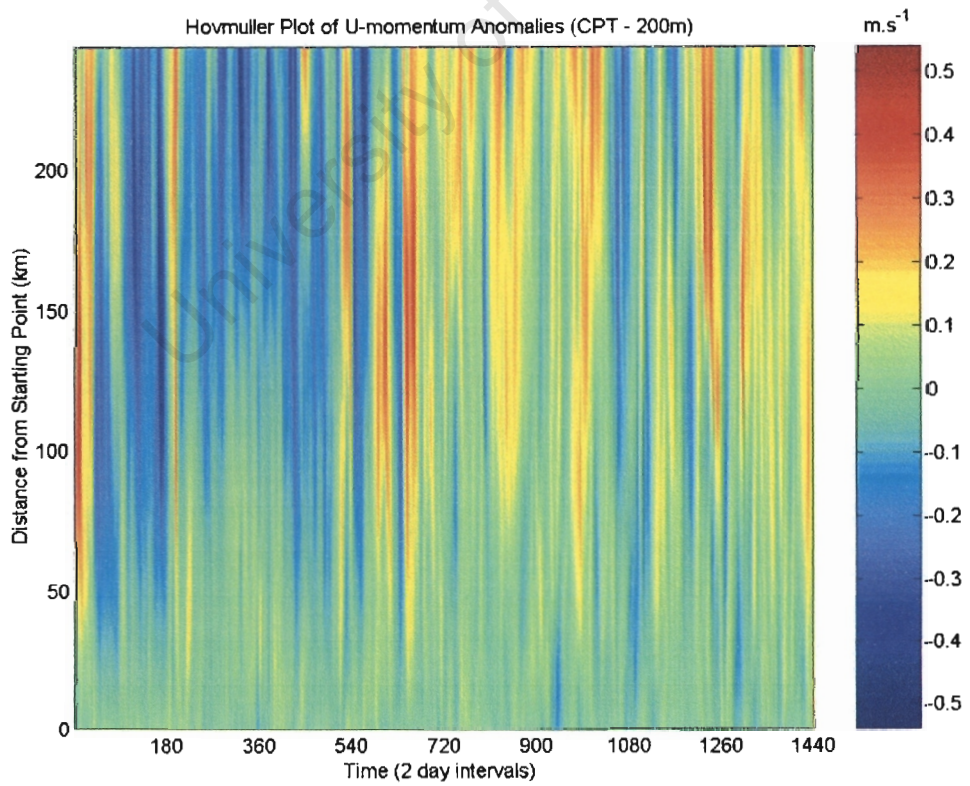

Figure 61: *Hovmuller Plot of U Anomalies at 200m deep along the Cape Point Transect*

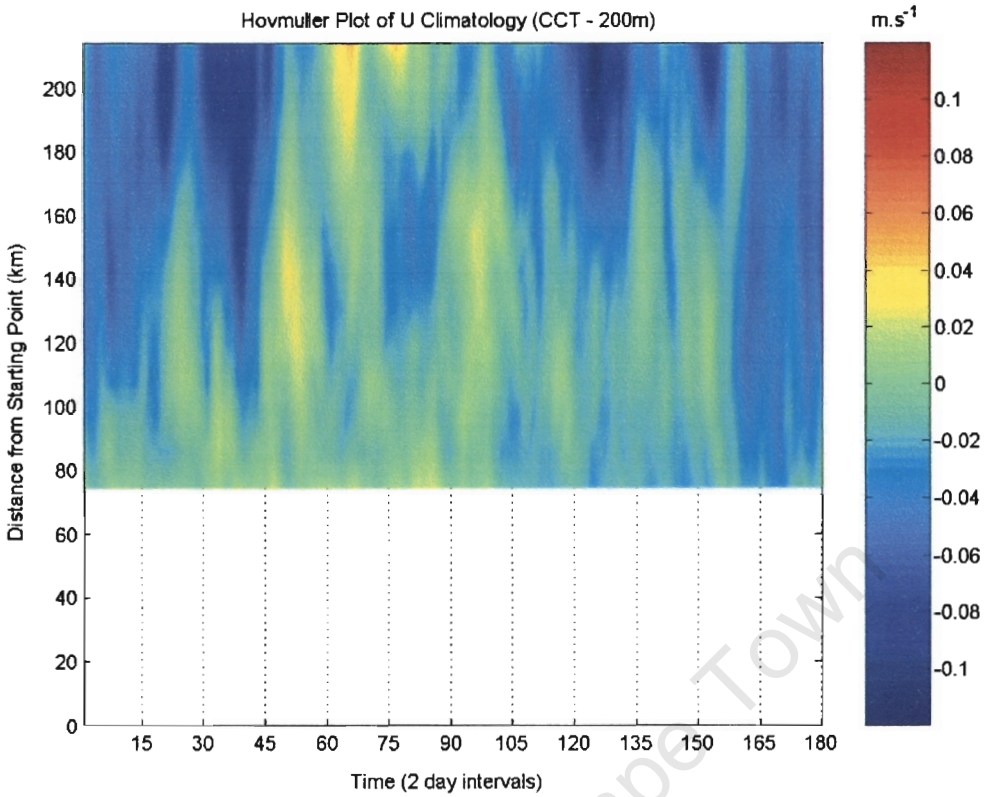

Figure 62: *Hovmuller Plot of U Climatology at 200m deep along the Cape Columbine Transect*

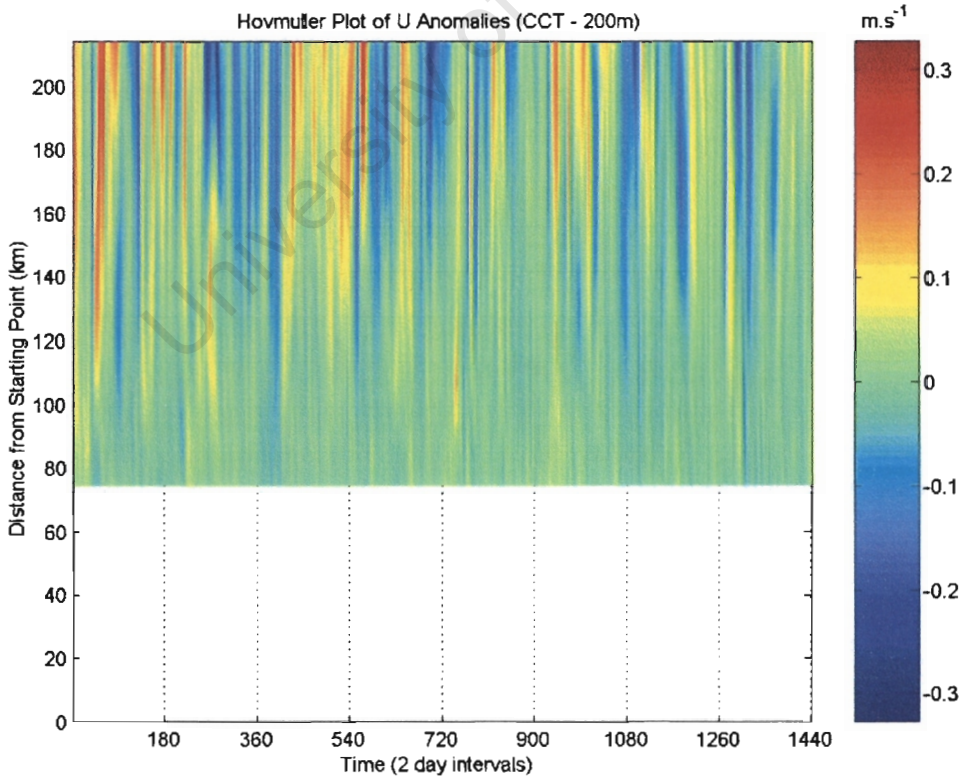

Figure 63: *Hovmuller Plot of U Anomalies at 200m deep along the Cape Columbine Transect*

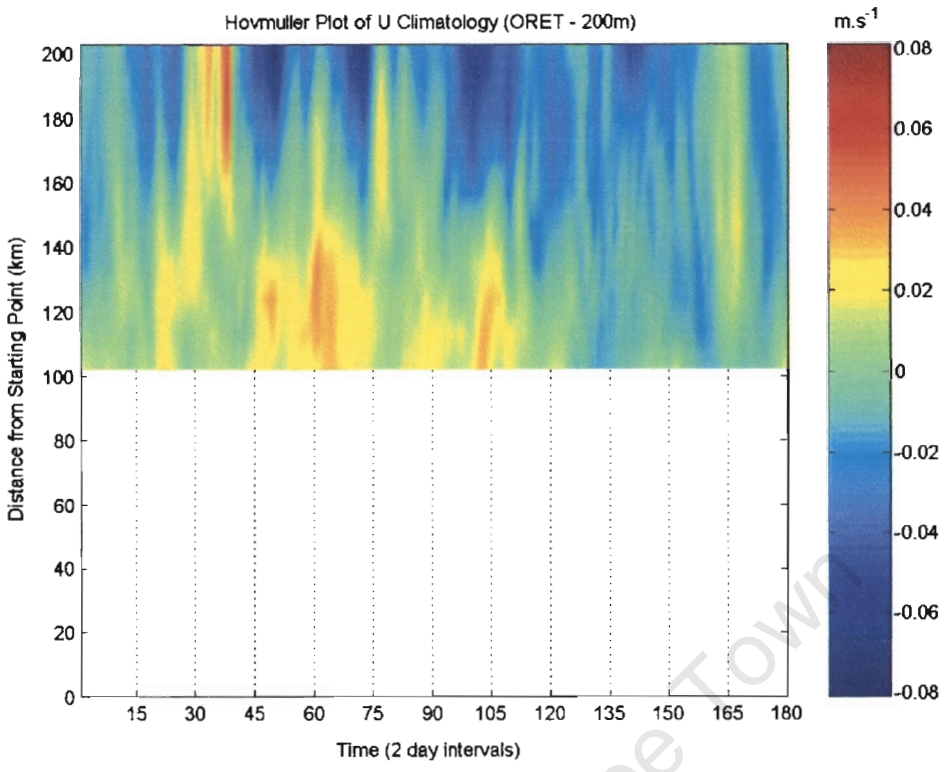

Figure 64: *Hovmuller Plot of U Climatology at 200m deep along the Oliphants River Estuary Transect*

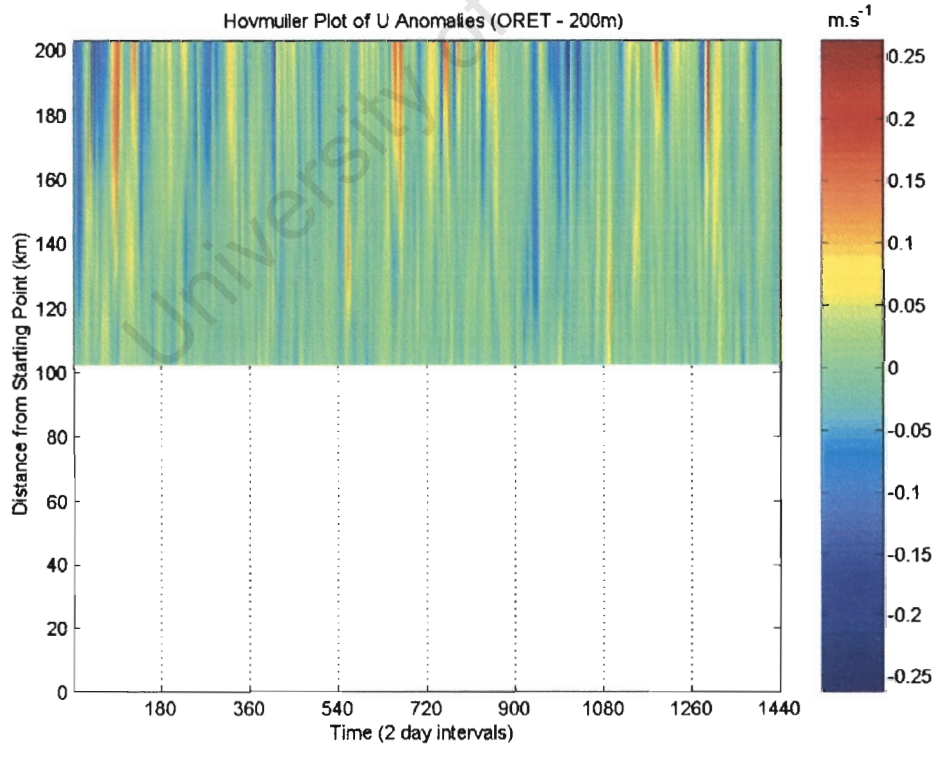

Figure 65: *Hovmuller Plot of U Anomalies at 200m deep along the Oliphants River Estuary Transect*

5.4 V VELOCITY (POSITIVE INDICATES SOUTHWARD FLOW)

5.4.1 RESULTS AT THE SURFACE

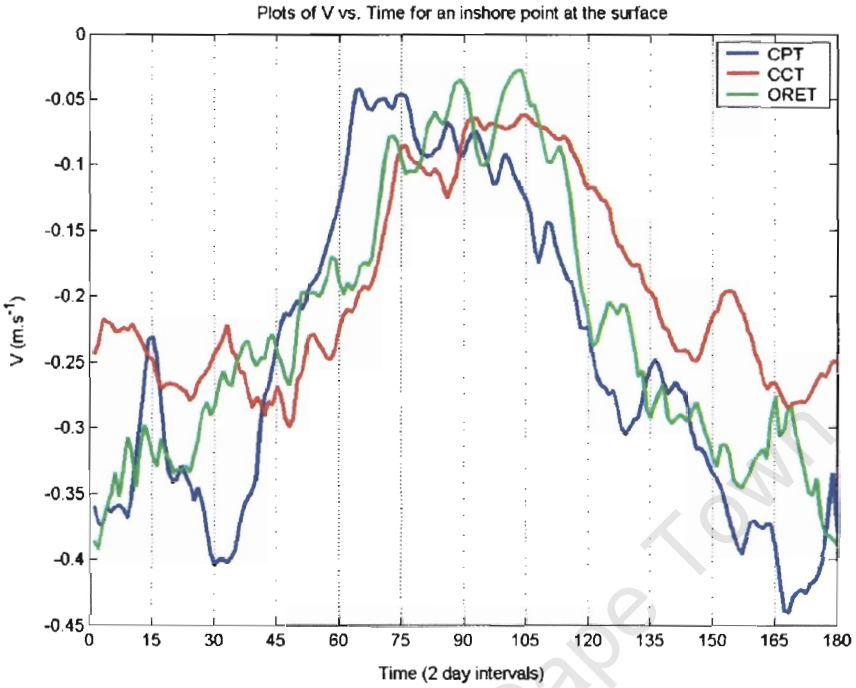

Figure 66: *Timeseries of V Climatology for the inshore locations at the surface*

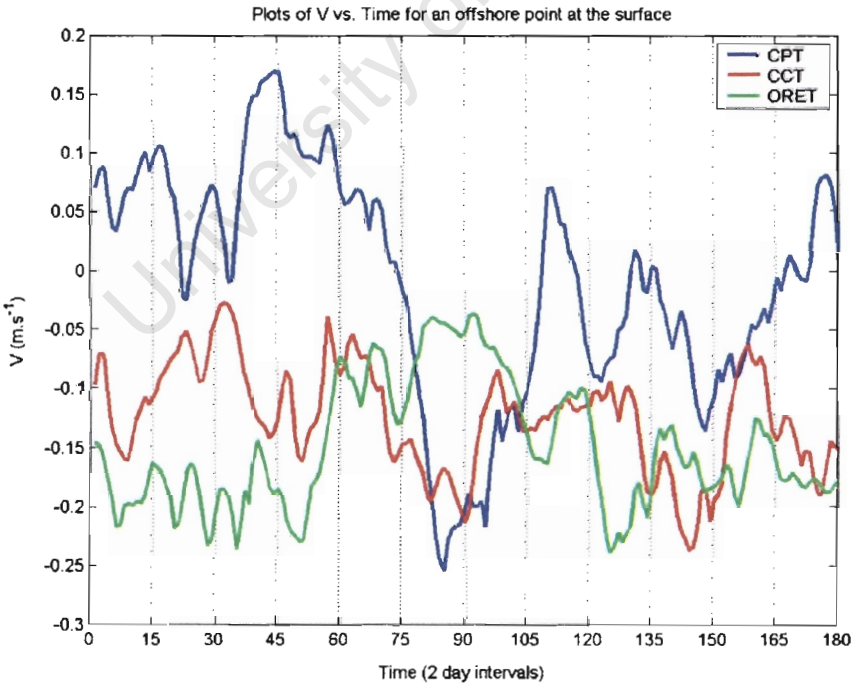

Figure 67: *Timeseries of V Climatology for the offshore locations at the surface*

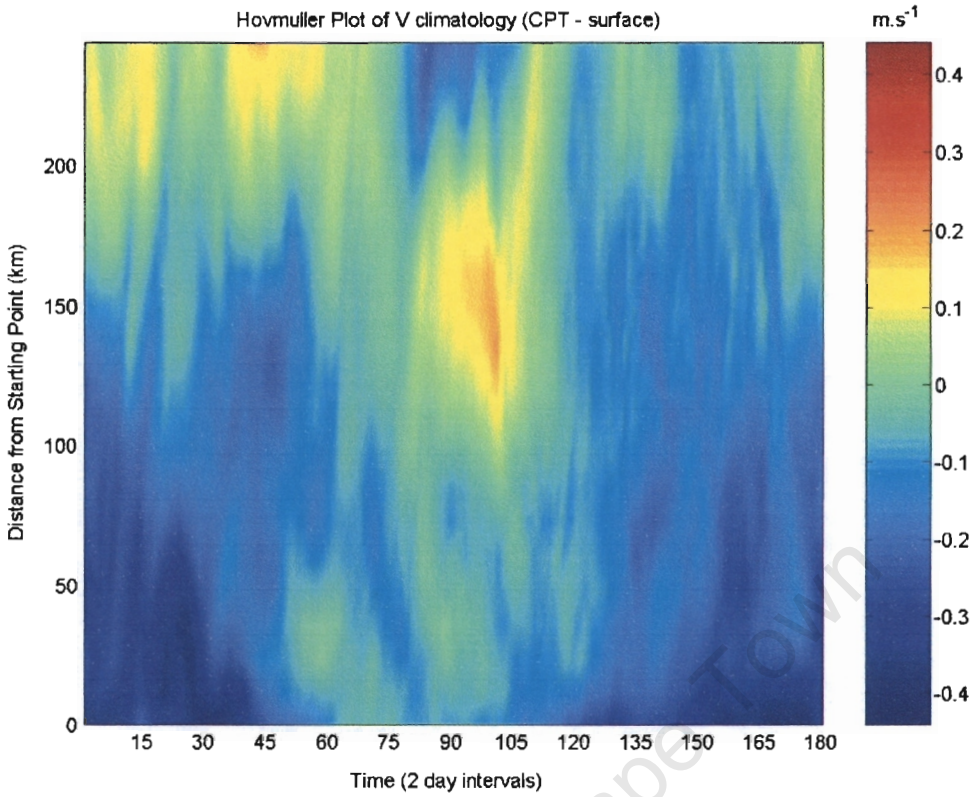

Figure 68: *Hovmuller Plot of V Climatology along the surface of the Cape Point Transect*

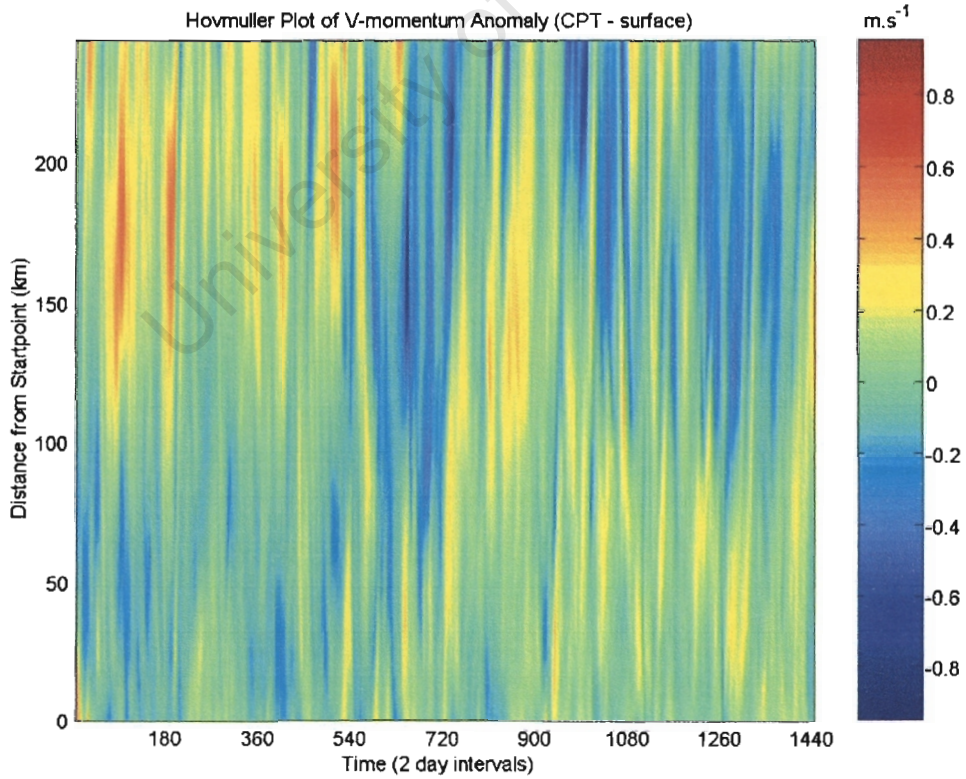

Figure 69: *Hovmuller Plot of V Anomalies along the surface of the Cape Point Transect*

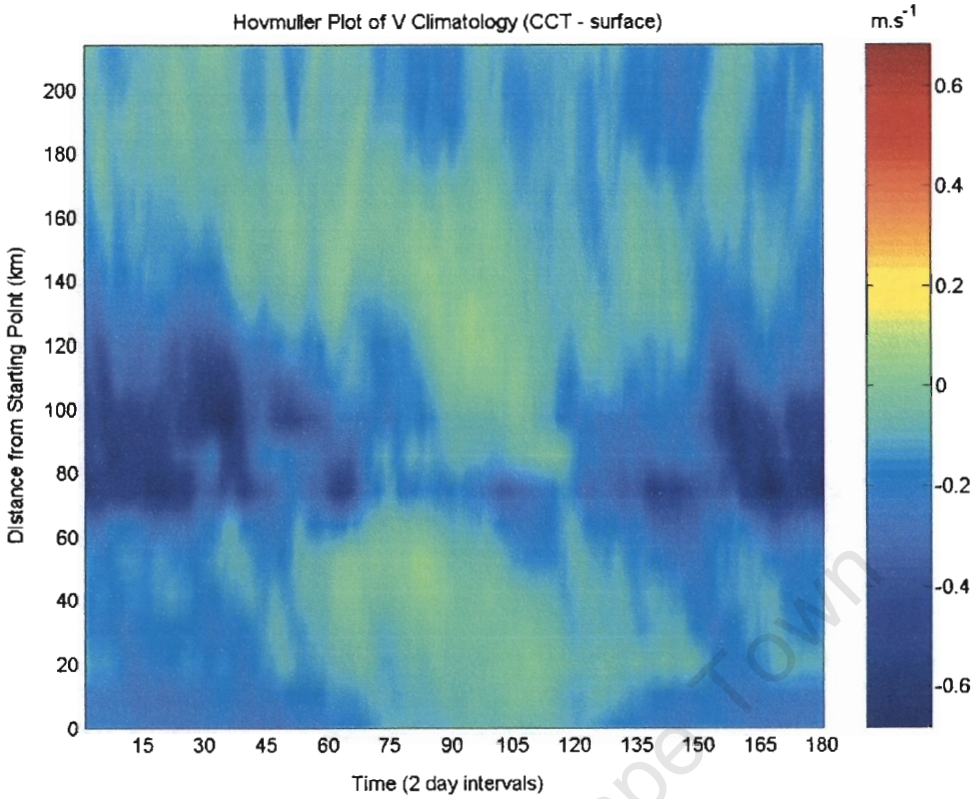

Figure 70: *Hovmuller Plot of V Climatology along the surface of the Cape Columbine Transect*

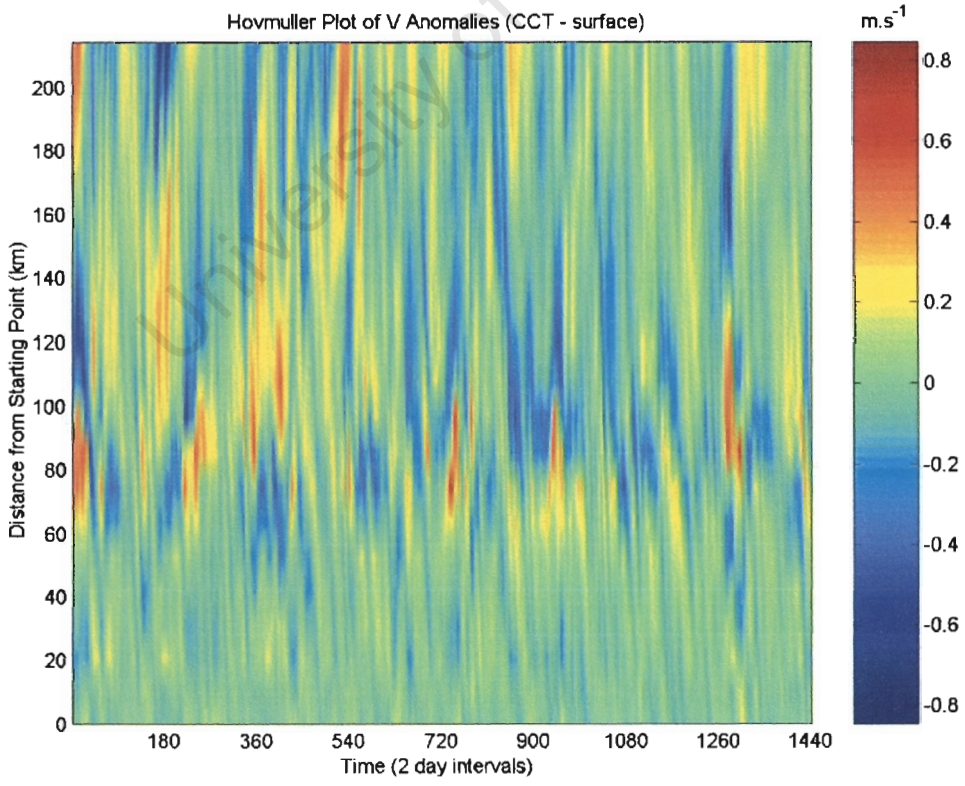

Figure 71: *Hovmuller Plot of V Anomalies along the surface of the Cape Columbine Transect*

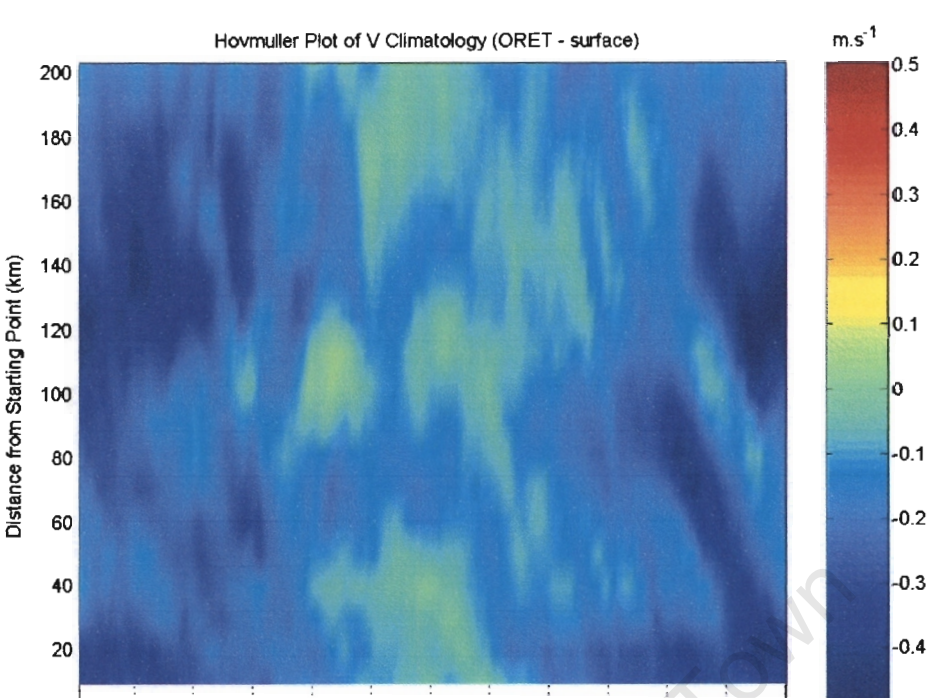

Figure 72: *Hovmuller Plot of V Climatology along the surface of the Oliphants River Estuary Transect*

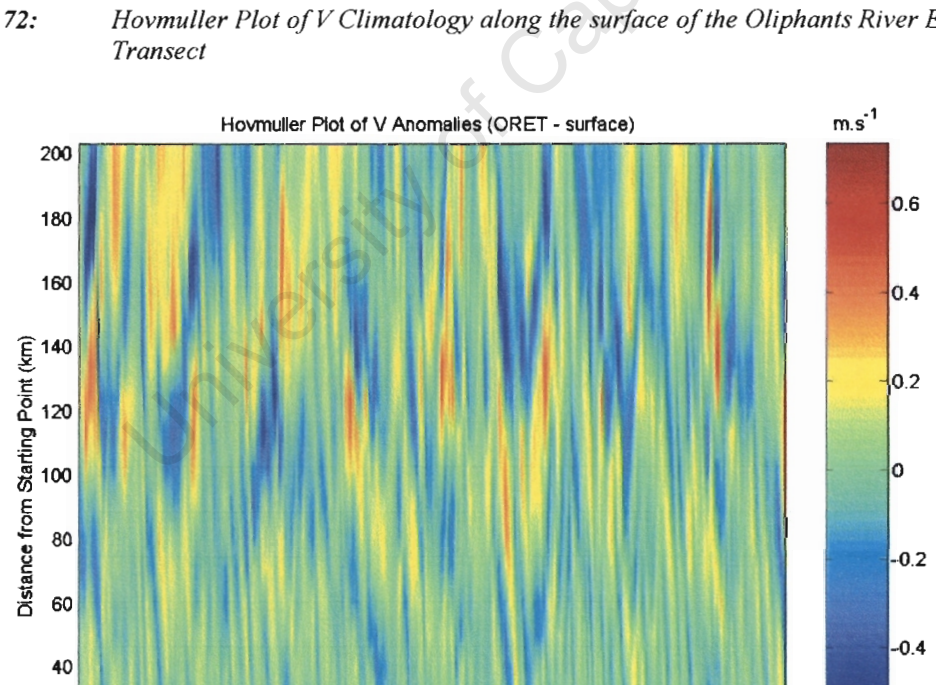

Figure 73: *Hovmuller Plot of V Anomalies along the surface of the Oliphants River Estuary Transect*

5.4.2 RESULTS AT 200M DEPTH

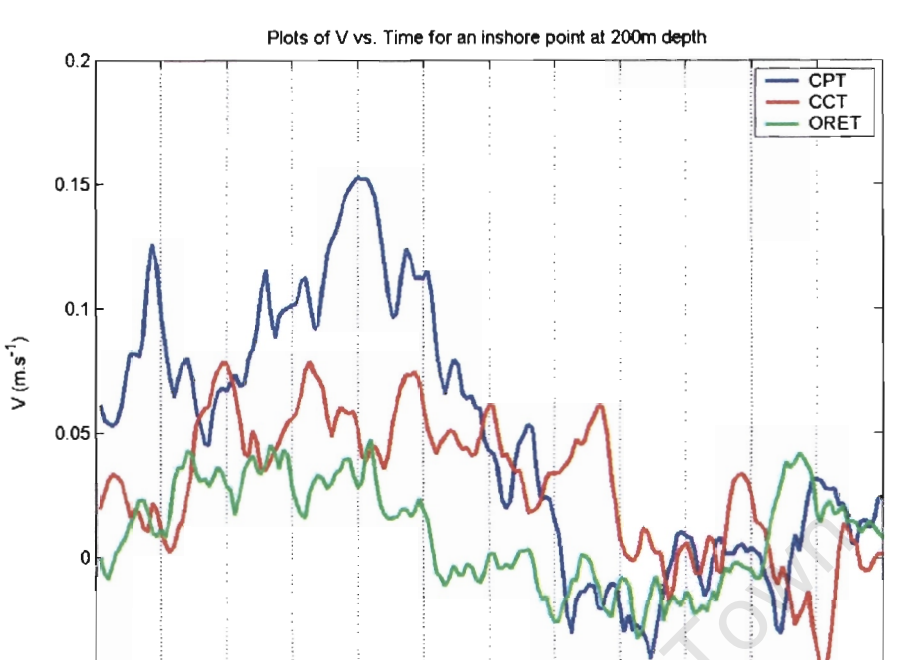

Figure 74: *Timeseries of V Climatology for the inshore locations at 200m deep*

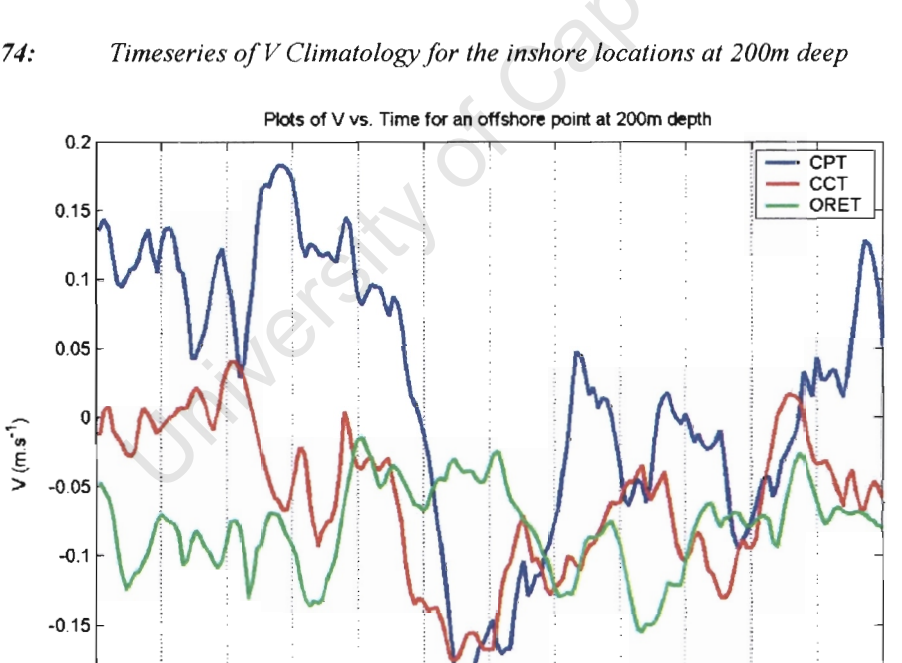

Figure 75: *Timeseries of V Climatology for the offshore locations at 200m deep*

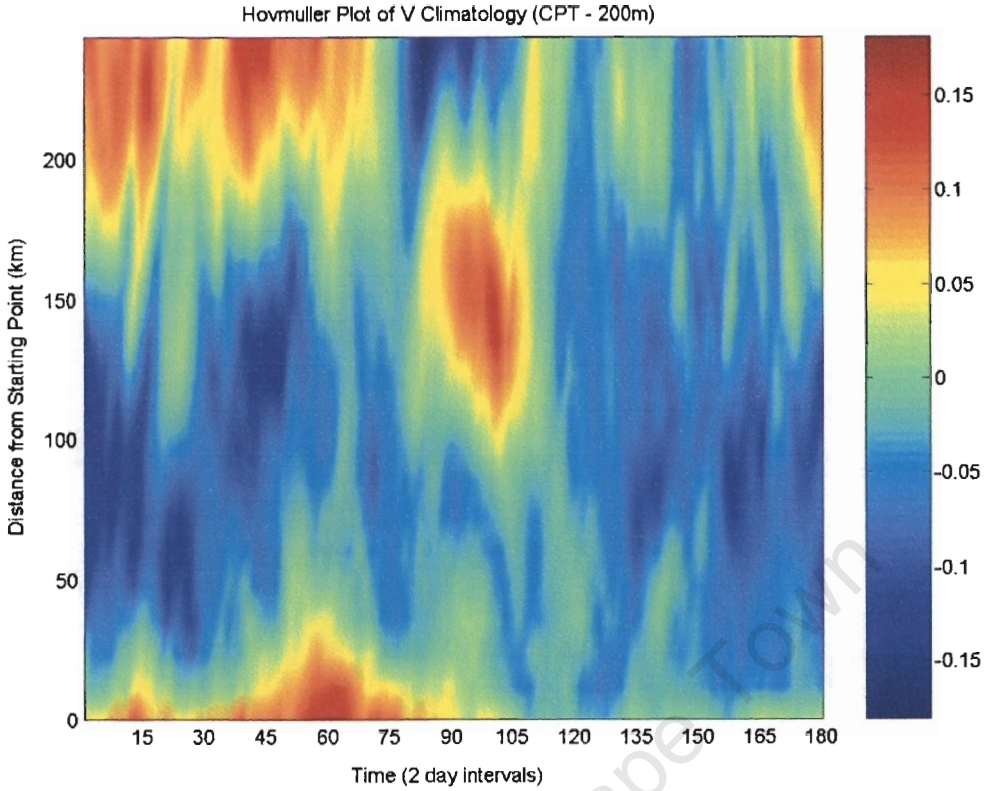

Figure 76: *Hovmuller Plot of V Climatology at 200m deep along the Cape Point Transect*

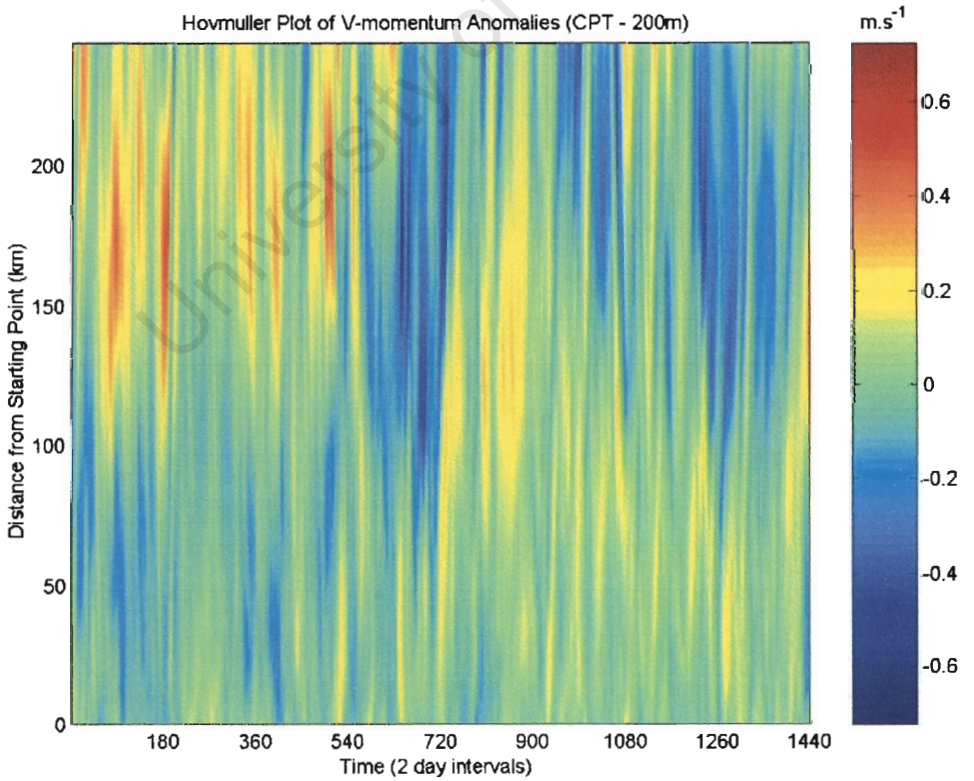

Figure 77: *Hovmuller Plot of V Anomalies at 200m deep along the Cape Point Transect*

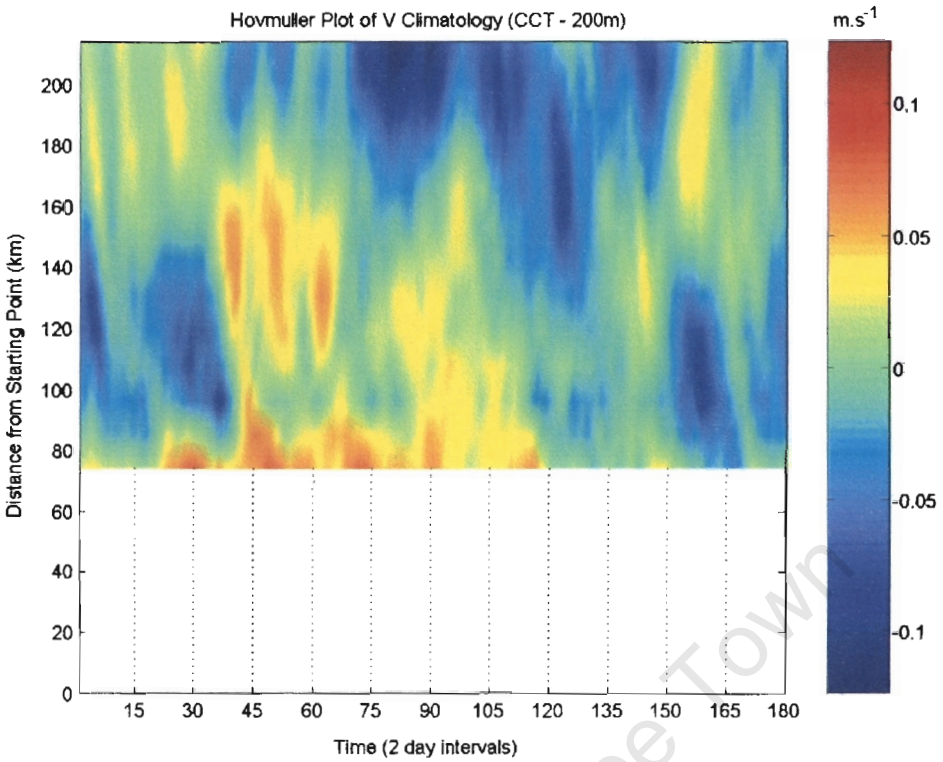

Figure 78: *Hovmuller Plot of V Climatology at 200m deep along the Cape Columbine Transect*

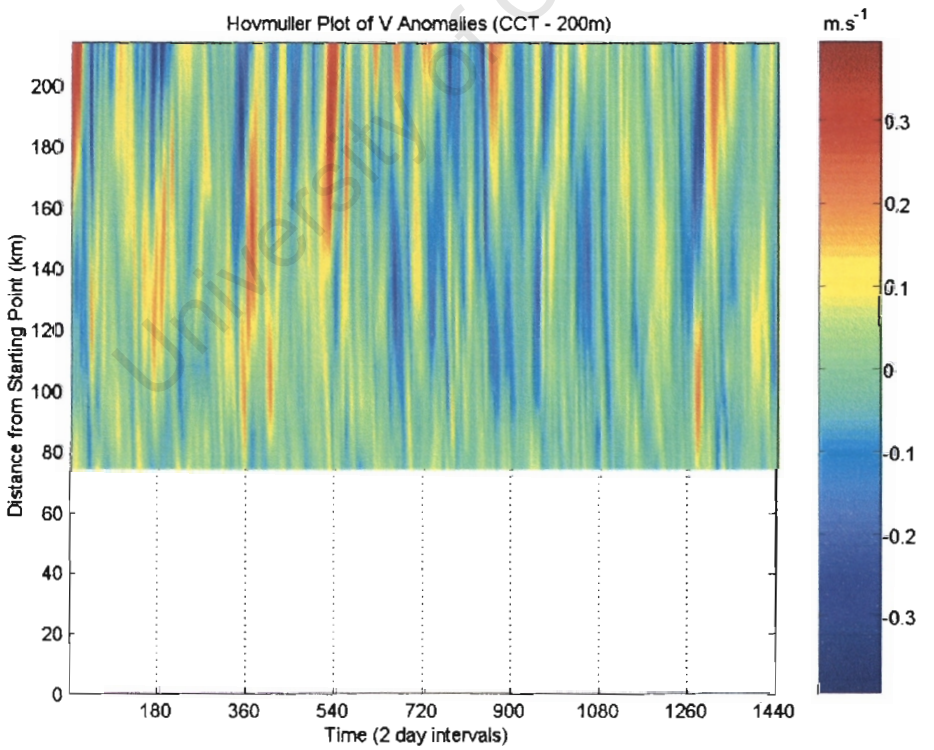

Figure 79: *Hovmuller Plot of V Anomalies at 200m deep along the Cape Columbine Transect*

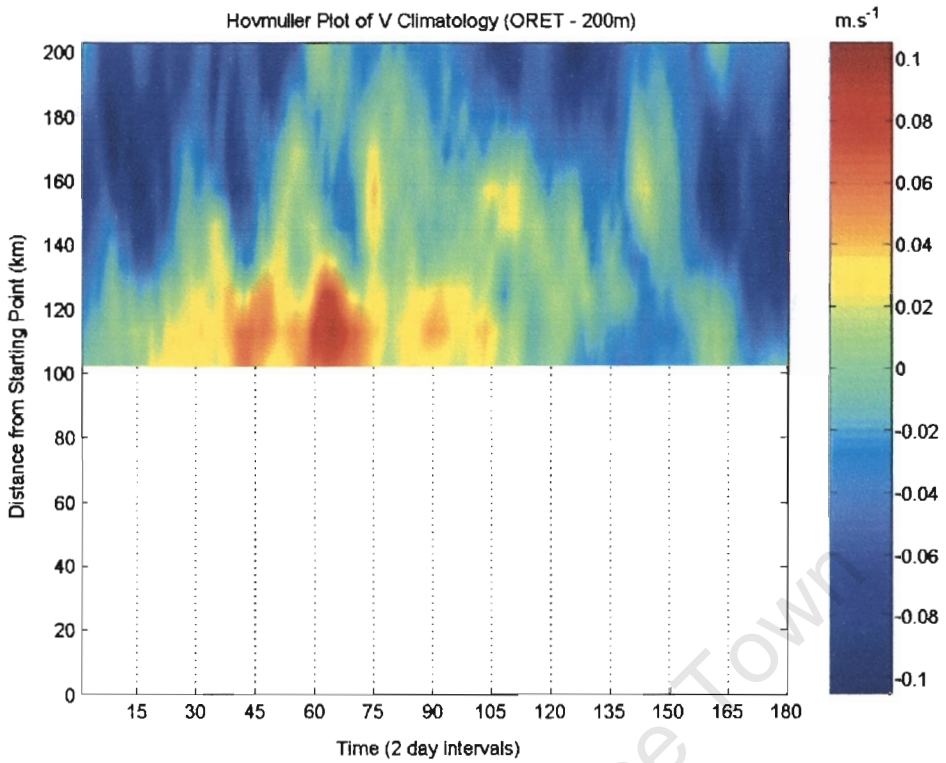

Figure 80: *Hovmuller Plot of V Climatology at 200m deep along the Oliphants River Estuary Transect*

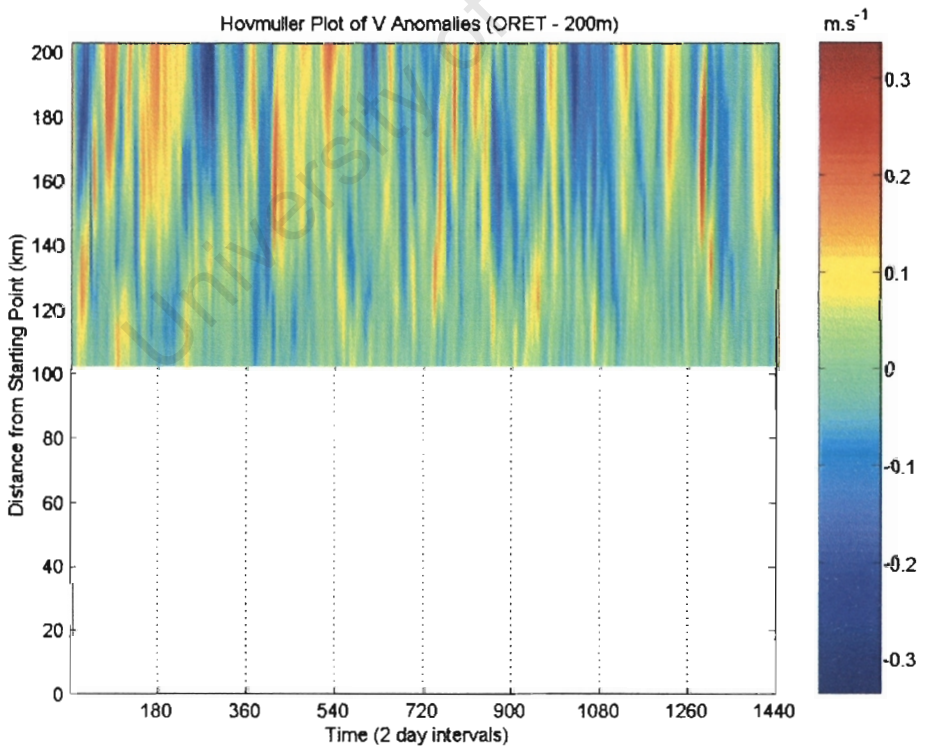

Figure 81: *Hovmuller Plot of V Anomalies at 200m deep along the Oliphants River Estuary Transect*

6 DISCUSSION

This section provides a description and discussion of the results previously presented section. The plots are discussed sequentially beginning with the timeseries plots and continuing to the climatology and anomalies for each transect, first at the surface and then at a depth of 200m. Once all the plots pertaining to a variable have been discussed, a short summary is given to integrate the discussion.

6.1 TEMPERATURE

From the timeseries (Figures 18 and 19) of the inshore and offshore points at the surface, we can observe that temperatures are higher towards the south and decrease northwards. The seasonal cycle is also more pronounced at the CPT, and its presence fades away gradually to the north. At the ORET it is barely noticeable. Offshore however, the latitudinal variation, makes little difference to the climatological temperature signal. All three transects displayed comparable values within the 16°C - 21°C range. The seasonal cycle at the offshore location is easily noticeable at all the transects. The amount of interannual variability, which would enhance the "jaggedness" of the line, appears to be highest in the offshore region of the CPT reminding us that this is an area of high activity due to Agulhas rings and filaments. Table 4 summarises the key factors observed in Figures 18 and 19.

Transect Name	Region	Approximate Mean Temperature (°C)	Approximate Temperature Range (°C)	Seasonal Cycle	Variability
CPT	Onshore	18.0	4.0	Easily detectable	Low
CCT	Onshore	15.0	2.0	Faintly detectable	Moderate
ORET	Onshore	14.0	1.0	Hardly detectable	Moderate
CPT	Offshore	18.3	3.5	Easily detectable	High
CCT	Offshore	18.5	5.0	Easily detectable	Low
ORET	Offshore	18.5	5.0	Easily detectable	Low

Table 4: *Characteristics of the Temperature Climatology as seen from point sources at the surface*

The temperature climatology along the surface of the CPT (Figure 20) shows a very clear seasonal picture with warming occurring from the start of December through to the end of April. On overall the alternating red and blue bands indicate that there is little cross-shore variation. It is interesting to note that both the maximum and minimum temperatures are located at the coastal side of the transect (<50km from the start of the transect). The associated anomalies (Figure 21), that are on the scale of ±3°C, are noticeably larger in the offshore region, indicating that there is more variability occurring here. There are two distinct

negative anomalies offshore, through year 5 and year 8, with positive anomalies between them.

At the CCT the surface climatology (Figure 22) shows a largely seasonal picture except for points located less than 20km from the start of the transect. We also see that the water closest to the coast is cooler throughout the year. This probably occurs due to a mixture of the seasonal cycle in winter and upwelling in summer. It also results in a well-developed cross-shore temperature gradient occurring in the warmer months (December – April) and a weaker gradient being set up in the cooler months (May – November). In both instances the water at the coast is usually cooler than the waters in the offshore area. This results in a positive temperature gradient as you move offshore. From the image we also notice that there is a change in the cross-shore temperature gradient at ~80km from the start of the transect. It appears as though there is a thermal front located here during December – April, but not during May - November. The associated anomalies that range from ±4°C (Figure 23), show a detectable series of events located at around 80km. Also shown by the anomalies, is the trend for larger anomalies to occur near the coast, as well as a negative anomaly occurring throughout the transect in year 8.

Along the surface of the ORET the temperature climatology (Figure 24) shows that there is once again a continual presence of cool water at the coast. From this transect it is possible to estimate that the cool water (marked roughly by the 15.5°C isotherm) is ~15km from the coast in summer and extends up to ~120km from the coast in winter. It also shows the existence of a thermal front at ~70km from the coast. The associated anomalies (Figure 25) that range from ±4°C, show that the largest of the interannual variability occur within 70km of the coast. There is also a slightly negative anomaly being detected throughout Year 5 and Year 8.

Looking at the subsurface data, we find an interesting pattern at the inshore locations (Figure 26). There is an annual cycle present in the subsurface waters, but it is distinctly out-of-phase with the seasonal cycle at the surface. This is noticed by observing that the maximum value at all three transects occur during the winter months (June and July) while the minimum values occur during the summer months (December and January). When compared to the surface location on the CPT (Figure 18), we can see that the ranges of the subsurface temperature climatologies are roughly twice as small. While a general decrease with temperature was expected, we are now able to see that this gradient is most pronounced at the CPT, and diminishes towards the north. An estimate from the graphs shows that, for the onshore locations, the mean annual temperature decrease, calculated as the difference between the

mean annual temperature at the surface and the mean annual temperature at 200m, was 7.5°C at CPT, 4°C at CCT and 3°C at ORET.

As upwelling would tend to lessen the vertical temperature gradient, the difference between temperatures at the surface and at 200m would be less in an area where upwelling intensity increases. From the above calculation we can deduce that upwelling is more intense at the north and decreases moving southwards.

Moving offshore, we see that there is little left of the seasonal signal as it is hidden behind mesoscale activity (Figure 27). At the ORET, however, the seasonal signal can be faintly detected. The range between the maximum and minimum temperature from the climatology is also about twice as small as that measure at the surface. This was also seen at the onshore locations. The approximate difference between the surface and 200m mean temperature shows little latitudinal variation. The estimated values were calculated to be 5.5°C at CPT, 6°C at CCT and 6°C at ORET.

Table 5 summarises the characteristics of the temperature climatologies at 200m deep.

Transect Name	Region	Approximate Mean Temperature (°C)	Approximate Temperature Range (°C)	Seasonal Cycle	Variability
CPT	Onshore	11.0	1.1	Easily detectable	Low
CCT	Onshore	11.0	1.5	Easily detectable	Low
ORET	Onshore	14.0	1.7	Easily detectable	Moderate
CPT	Offshore	12.6	1.9	Hardly detectable	High
CCT	Offshore	12.3	0.7	Hardly detectable	High
ORET	Offshore	12.4	1.2	Hardly detectable	High

Table 5: *Characteristics of the Temperature Climatology as seen from point sources 200m below the surface*

The climatology at 200m deep along the CPT (Figure 28) shows that there is an overall seasonal pattern in both the onshore and offshore region. Offshore, the pattern is what we would normally expect from the seasonal warming and cooling, but close to the coast the inverse occurs with waters being cooler during summer and warmer during winter. The changeover region from an inverse to a normal seasonal cycle occurs roughly 50 – 75km from the start of the transect. The anomalies that range between ±3.2°C, are mostly small near the coast and large at locations further than 50km.

The temperature climatology at 200m deep along the CCT (Figure 30), faintly shows the normal seasonal pattern in the offshore areas, while the inverted seasonal cycle is easily noticeable, in the inshore region, and confined to a horizontal distance of ~25km from the shelf. Here at the CCT, the changeover region is located around 20 – 40km from the shelf.

Similarly to what was previously observed, the anomalies are larger in the offshore area and fall between the range spanning ±2.5°C.

The temperature climatology at 200m along the ORET (Figure 32), is similar to that observed at the CCT. Here however, the offshore extent of the inverted seasonal cycle reached out to ~35km from the shelf. The range of the anomalies was ±3°C and it was noticed once, again that the largest anomalies fell in the offshore region. On overall, the anomalies were smallest here, indicating a smaller amount of mesoscale activity.

The most likely explanation of the inverted seasonal cycle seen that the onshore locations in the subsurface onshore region, is that Upwelling, which also exhibits seasonal characteristics, causes the water temperature to drop during the months that its intensity increases. Since warming due to insolation is only expected to affect a thin layer at the surface of the water column, the warming effect during the summer months would tend to obscure the cooling brought on by the heightened state of upwelling during these times. Below the surface however, where direct heating from the atmosphere is not a major factor, the cooling due to upwelling is dominant. The intensity of the Upwelling at the CCT and ORET, would also explain the presence of the perpetually cool waters on the coastal side of those transects. By looking at how far offshore cool water can be found during Summer at the surface, and at how far offshore the changeover region is at 200m, we are able to estimate the vertical structure of Upwelling on each transect. The results are summarised in Table 6.

Transect Name	Offshore extent at surface (km)	Offshore extent at 200m (km)	Depth from which water comes (m)
CPT	0	50	>200m
CCT	10	25	>200m
ORET	20	40	>200m

Table 6: *Details of the vertical structure of upwelling from temperature climatologies*

6.2 SALINITY

The seasonal fluctuation is easily discerned from the salinity climatologies at the inshore locations at the surface of the three transects (Figure 34). Fresher waters with a mean salinity of ~34.92psu are found towards the north while more saline water with a mean salinity of ~34.97psu can be found at the CPT. This indicates a general decrease in salinity while travelling north. From the image, it can be observed that while the season signal at the CCT and ORET transects are in phase, the signal observed at the CPT lags by about 2 months. This can be physically interpreted as a salinity "event" originating around the ORET or CCT, travelling southwards along the West Coast and reaching the location of the CPT after two months. From the timeseries at the surface of the offshore locations (Figure 35), we see that at all transects, the seasonal signal is small in comparison to other factors. Generally the offshore waters are more saline than their onshore counterparts, and while there was a salinity gradient between transects at the onshore locations, it is not present offshore. Table 7 summarises the characteristics of the salinity climatologies at the surface.

Transect Name	Region	Approximate Mean Salinity (psu)	Approximate Salinity Range (psu)	Seasonal Cycle	Variability
CPT	Onshore	34.97	0.04	Easily detectable	Low
CCT	Onshore	34.92	0.08	Easily detectable	Low
ORET	Onshore	34.91	0.05	Easily detectable	Low
CPT	Offshore	35.00	0.05	Hardly detectable	High
CCT	Offshore	34.99	0.03	Hardly detectable	High
ORET	Offshore	34.99	0.03	Hardly detectable	High

Table 7: *Estimated characteristics of the Salinity Climatology as seen from point sources at the surface*

The salinity climatology along the surface of the CPT (Figure 36) shows that at the onshore regions there is a slight seasonal signal noticed by observing the patch of lower salinity water located here during February - July. There is also clearly a concentration of higher salinity water during this same period at the offshore location. This results in a considerable cross-shore salinity gradient being set up between February and July. During the rest of the year, the salinity values tend towards an equilibrium state. The range of the anomalies (Figure 37) fall between ±0.2psu, and indicate two outstanding negative anomalies of ~-0.1psu during Year 5 and Year 8 centred at around 150km from the start of the CPT. All of the other years exhibited a slightly positive anomaly of ~0.05psu.

The climatology along the surface of the CCT (Figure 38) shows that there is a clearly noticeable offshore extent at which the salinity displays the seasonal cycle. This occurs at

~100km from the start of the transect. In the first 100km of the transect, the seasonal cycle has low values from November – March and high values from June – August. Further than 100km offshore, there is a constant salinity value greater than ~34.97psu.
The anomalies (Figure 39) show that there are once again two distinct low anomalies occurring in the offshore region of ~ -0.1psu during Year 5 and Year 8. During the rest of the years, the transect is dominated by a slightly positive anomaly of around 0.3psu.

Along the surface of the ORET, the salinity climatology (Figure 40) shows a similar pattern to the climatologies seen at the other transects. The seasonal cycle is noticeable until ~150km from the coast. Further offshore salinities >34.97psu are relatively constant throughout the year. The cycle that is noted within ~150km of the coast, has higher values during June-August and lower values during November - March making it in phase with the cycle that was observed at the CCT. The anomalies (Figure 41) are similar to the one calculated for the CCT, in that it shows two negative anomalies during Year 5 and Year 8. Between these negative anomalies, a slightly positive anomaly dominates.

At 200m below the surface we still find the seasonal cycle displayed in the Salinity climatology at all three transects in the onshore region (Figure 42). The climatology at the CPT and the CCT show a decrease with depth whereas those at the ORET remain relatively constant. At this depth, the onshore seasonal cycle is also seen to be in phase at all three transects. Offshore (Figure 43), the salinities exhibit the same general characteristics as those found at the surface. The only noticeable difference is that the waters below the surface are clearly less saline that those above. This shows a definite decrease in salinity with depth. Table 8 summarises the general characteristics of the salinity climatologies as taken from point sources at 200m deep.

Transect Name	Region	Approximate Mean Salinity (psu)	Approximate Salinity Range (psu)	Seasonal Cycle	Variability
CPT	Onshore	34.84	0.04	Easily detectable	Low
CCT	Onshore	34.85	0.12	Easily detectable	Low
ORET	Onshore	34.89	0.15	Easily detectable	Moderate
CPT	Offshore	34.90	0.07	Hardly detectable	High
CCT	Offshore	34.90	0.04	Hardly detectable	High
ORET	Offshore	34.90	0.04	Hardly detectable	High

Table 8: *Estimated characteristics of the Salinity Climatology as seen from point sources at 200m below the surface.*

The climatology at 200m deep along the CPT (Figure 44) shows that there are two different seasonal cycles occurring along the transect. The onshore cycle, that matches what was seen at the other locations, tends to have higher salinities during the winter months and lower

salinities during the summer months, while the offshore cycle displays the inverse. The anomalies (Figure 45) that range between ±0.12psu shows that the amount of variability seen throughout the transect. The negative anomaly during Year 5 is still present in figure but the anomaly seen previously during Year 8 is somewhat less noticeable.

At 200m deep along the CCT (Figure 46), the seasonal cycle is confined to a narrow strip close to the shelf, extending to about 40km offshore. During the winter months at the shelf, and throughout the year in the offshore region high salinity water prevails at this depth. The associated anomalies (Figure 47) show almost nothing of the negative anomalies observed during Year 5 and Year 8 at the other locations. While range of the anomalies is still roughly equal (±0.11psu), no clear pattern can be noticed from them.

The climatology along the ORET at 200m (Figure 48) shows that the seasonal cycle here is confined to an area within ~60km from the shelf. Further offshore, the water is again dominated by high salinity values. The associated anomalies (Figure 49) exhibit a range that is a good degree larger than the salinity anomalies at the other subsurface locations (±0.2psu). Apart from the large positive anomaly located at the shelf during the first half of Year 6, the rest of the anomalies appear to be small.

On overall, the salinities have shown a pattern that can be understood if one accepts that the seasonal cycle has a more direct effect on the temperature of the water than on the salinity. In the open ocean, where upwelling is not a major factor, seasonal warming and cooling would therefore not normally be noticed in the salinity as it is not directly affected. Temperature, on the other hand would be affected directly. If you consider areas where upwelling, which displays seasonal characteristics in its intensity, is a known factor, we can understand the reason for observing a seasonal cycle in the salinities that was confined to the coast. This was noticeable at least down to a depth of 200m. Waters of lower salinity are being brought to the surface during periods when the intensity of upwelling peaks. There is a link between the vertical structure of the seasonal cycle observed in the salinities (Table 9) and the vertical structure of upwelling deduced from temperature observations (Table 6).

Transect Name	Offshore extent where seasonal cycle was noticed at the Surface (km)	Offshore extent where seasonal cycle was noticed at 200m deep (km)
CPT	75	50
CCT	90	40
ORET	130	60

Table 9: *Vertical structure of the seasonal signal as seen from the Salinity climatologies.*

As upwelled water nears the surface, we expect that it would start to spread out. In the upper layers however, the temperature signal becomes obscured due to the warming. When looking over longer time periods, the temperature mixes at a faster rate than the salinity and thus the salinity would "hold" the upwelling signal for a longer period of time. Thus the table displayed above (Table 9) shows a better picture of the vertical structure of the upwelled water than the previous one given (Table 6).

In general, the range of the anomalies was always higher than the range of the climatologies, which is an indication of the variability seen in the region. Year 5 and Year 8 have stood out again as years during which a large negative anomaly prevailed.

6.3 WATER CIRCULATION (U & V)

The timeseries at the surface for the inshore locations (Figure 50, 66) shows that there is a seasonal signal in the V (longshore) component at all transects, while a noticeable seasonal signal in the U (offshore) component was only observed at the CPT. It is not surprising that the V component is always negative as this indicates a predominantly northward flow that is consistent with the flow due to the Benguela current. The wind stress used to drive the model has a positive northerly component throughout the year, and it is encouraging to note that the calculated U and V components coincide with the behaviour of the wind stress patterns above. The U component at the inshore at the surface of the CPT is almost always positive indicating a flow approximately towards the Southwest. A flow in this direction would generally enhance upwelling and it orientation, as well as the nature of the seasonality, is what was expected. At the CCT and ORET the U components show a pattern that is contrary to what is expected from an area that is affected by Upwelling. At these transects, the U component is always, or almost always negative throughout the year indicating a flow directed towards the coast, that would suppress upwelling.

In the offshore regions, the U component at all three transects remain relatively close to zero indicating that there is no constant onshore or offshore flow at the surface. The V component however shows that at the CCT and ORET, there is a nett negative longshore flow (ie: towards the north) while the CPT shows that the nett longshore flow is zero. Table 10, summarises the major factors seen in the U and V components at the surface

Transect Name	Variable	Region	Approximate Mean Velocity ($m.s^{-1}$)	Approximate Velocity Range ($m.s^{-1}$)	Seasonal Cycle	Mesoscale Activity
CPT	U	Onshore	0.15	0.31	Moderately detectable	Moderate
CCT	U	Onshore	-0.02	0.06	Not detectable	Moderate
ORET	U	Onshore	-0.15	0.13	Hardly detectable	Moderate
CPT	U	Offshore	-0.02	0.27	Not detectable	High
CCT	U	Offshore	-0.05	0.23	Not detectable	High
ORET	U	Offshore	0.00	0.30	Not detectable	High
CPT	V	Onshore	-0.25	0.40	Easily detectable	Moderate
CCT	V	Onshore	-0.20	0.25	Easily detectable	Moderate
ORET	V	Onshore	-0.25	0.37	Easily detectable	Moderate
CPT	V	Offshore	0.00	0.40	Hardly detectable	High
CCT	V	Offshore	-0.07	0.22	Hardly detectable	High
ORET	V	Offshore	-0.07	0.13	Not detectable	High

Table 10: *Estimated characteristics of Water circulation as seen from point sources at the surface.*

The climatology and anomaly observed at the surface of the CPT for the U component (Figures 52 and 53) show that the offshore-flowing water occurring at the coast is indeed moving at its fastest during the summer months of the year. It also shows that this phenomenon decreases in speed as it moves further offshore. The only noticeable period where westerly moving waters occur at the surface is during the month of July and located between 50 and 200 km from the start of the transect. The range of the anomalies, which is roughly double the range of the climatology, reveals that there is much interannual variability between years, which in turn would make the climatology calculation difficult for such a short dataset. The anomalies are however visibly larger in the offshore region, which is understandable due to the presence of rings and filaments from the Agulhas current, being located there.

The motion along the V direction (Figures 68 and 69) was also seasonal, particularly from the starting point of the transect up to a point ~150km from there. The image shows that near the start, water movement is quite intense (reaching up to 0.4m.s^{-1} during Summer and easing off to between 0.0 and 0.1 cm.s^{-1} during Winter), and towards the northwest on average. The waters offshore move mainly towards the southeast (at around 0.15m.s^{-1}) throughout the year except during June when a northwesterly flow of around 0.3m.s^{-1} was observed. The range of the anomalies show that the V component is also subject to a high level of variability, as the range is about twice as large as the range of the climatologies. The largest anomalies were noticed in the offshore region.

Along the surface of the CCT, the climatology and anomalies of the U component (Figure 54 and 55) show that there is a distinct zone, up to 100km from the start of the transect, where a relatively constant and often quite intense (up to 0.3m.s^{-1}) onshore flow occurs. Offshore, the flow along the xi axis remains close to zero throughout the year. The anomalies, range between ±0.65m.s^{-1} and occur with equal positive and negative magnitude throughout the transect. The V climatology and anomalies (Figures 70 and 71) show that, over the whole transect, the flow is either approximately zero or slightly to the north, with more negative values being observed during summer. However, during summer in the area between 70km and 140km, the Northward flow intensity increases to ~0.6m.s^{-1}. The relatively large anomalies (±0.81 m.s^{-1}) reveal that the V component is also subjected to high variability.

The U climatology and anomalies of the ORET transect (Figures 56 and 57) show that there is a zone of onshore-flowing water located from the coast up until about 20km from there. This occurs mainly in summer and loses most of its signature during winter. Over the transect, the average flow if directed offshore, except for a bit of onshore flow during the winter months in the far offshore region (~200km). The range of the associated U anomalies is larger than the

range of the climatology and falls between ±0.55m.s^{-1} indicating high levels of interannual activity. The climatology and anomalies of the V component shows a seasonal signal that has more positive values during winter (~0.00 m.s^{-1}) and large negative values (~0.4 m.s^{-1}) during summer, with little difference between the onshore and offshore areas. The anomalies fall within the range of ±0.8 m.s^{-1}, and are noticeably larger in the offshore region. Close to the coast, they are almost zero.

At a depth of 200m the timeseries of the climatology of the U component at the onshore locations (Figure 58) showed no noticeable seasonal signal. The range and scale of the U component in the subsurface waters were much less than those observed at the surface. At the offshore locations (Figure 59), there was no noticeable difference in either the seasonality, the range, or the scale between the U component at the surface and subsurface layers. The amplitude of the seasonal signal of the V component at 200m at the onshore location (Figure 74), was observed to decrease towards the north (ie: from the CPT towards the ORET). This was observed during April, May and June, but for the rest of the year, the V component remained roughly equal at all transects. When compared to the surface, it was observed that the V component at 200m deep peaks roughly 2 months before the peak is observed at the surface. At the onshore locations, the most notable factor is that the mean velocity is positive at 200m while it is negative at the surface for all transects. This would result in a net southward flow being observed along the 200m isobath while a net northward flow is observed at the surface. The table below summarises the main characteristics of the water circulation at 200m as seen from an onshore and offshore point source.

Transect Name	Variable	Region	Approximate Mean Velocity (m.s^{-1})	Approximate Velocity Range (m.s^{-1})	Seasonal Cycle	Variability
CPT	U	Onshore	0.01	0.05	Not detectable	High
CCT	U	Onshore	0.00	0.05	Hardly detectable	High
ORET	U	Onshore	0.01	0.07	Not detectable	High
CPT	U	Offshore	-0.01	0.20	Not detectable	High
CCT	U	Offshore	-0.04	0.15	Not detectable	High
ORET	U	Offshore	-0.03	0.14	Not detectable	High
CPT	V	Onshore	0.05	0.20	Easily detectable	High
CCT	V	Onshore	0.03	0.12	Hardly detectable	High
ORET	V	Onshore	0.02	0.07	Hardly detectable	High
CPT	V	Offshore	0.00	0.39	Not detectable	High
CCT	V	Offshore	-0.06	0.20	Hardly detectable	High
ORET	V	Offshore	-0.08	0.15	Not detectable	High

Table 11: ***Estimated characteristics of Water circulation as seen from point sources at 200m below the surface.***

The Hovmuller Plot of the U climatology at the CPT at 200m (Figure 60) shows that there is a complex picture regarding the flow along the xi axis, even though the seasonal signal is still

noticeable. More positive U values were observed in the summer months (November – February) while more negative values, that sometimes reached –0.14 $m.s^{-1}$, were observed during the winter months (July – August). In the onshore region (less than 45km from the start of the transect), the climatology showed comparatively little variation and values fell between 0.00 and 0.05 $m.s^{-1}$. The anomalies (Figure 61) fell in the range ±0.53 $m.s^{-1}$, showed that the onshore variability is significantly less than that observed offshore. A concentration of large negative anomalies in the offshore area was observed during the first three years. It is interesting to note that the climatology and anomalies closely resemble what was observed for the same location at the surface (Figures 52 and 53).

The Hovmuller plot of V climatology at a depth of 200m along the CPT (Figure 76) shows an equally complex picture. The flow along the eta axis throughout the transect can be divided up into 3 categories. In the region <50km from the start of the transect, the flow is V component was almost always positive indicating a flow towards the southeast. The flow here intensified during the first half of the year and reached a peak during April and May. In the region between 50km and 175km from the start of the transect, a seasonal pattern can clearly be seen. In this zone, there is a negative flow along the eta axis between October and April, while a positive flow occurred between May and September. This shows that there was a flow towards the NW between October and April, while the flow is directed towards the SE between May and September. In the region further than 175km from the start of the transect, the flow pattern resembles that in the region less than 50km from the start. The only difference is the intense negative flow (towards the NE) that occurs. The anomalies fall in the range between ±0.67 $m.s^{-1}$ and show, once again, that there is greater variability in the offshore region. A glance at the image reveals that the intense positive anomalies occurred within the first three years and the intense negative anomalies occurred within the final five years. With the exception of the southeast flow observed in the climatology that extends to 20km away from the starting point of the transect between January and May, both the climatology and anomalies of the V component resemble what the behaviour was at the surface (Figures 68 and 69).

At 200m deep along the CCT, the climatology of the U component is largely positive in a zone between 80km and 120km from the start of the transect (Figure 62). This shows an overall offshore flow of water at that depth and is in good agreement with the climatology of the U component seen at the surface immediately above. Further offshore (more than 160km from the start of the transect), the seasonal signal becomes apparent and can be observed as a negative U component from September to March and a positive U component from April to July. The anomalies (Figure 63) roughly match what was seen in the area immediately above (Figure 55). The range of the anomalies (±0.32 $m.s^{-1}$) was smaller than that observed at the

surface but still quite larger than the range of the climatology. The climatology of the V component at 200m along the CCT (Figure 78) shows that there is a considerable southward flow of water occurring within the closest 25km to the shelf, particularly during the first half of the year and exhibiting a peak in April. Not much structure could be seen from the data along the rest of the transect. The anomalies (Figure 79) fall within the range of ± 0.4 m.s^{-1}, and roughly match in terms of orientation, what was seen at the surface (Figure 71).

At the ORET, the climatology of the U component at 200m (Figure 64) show a tendency for the locations near the shelf to exhibit an offshore flow while an onshore was observed at areas further than 170km from the start of the transect. This appears to be relatively constant throughout the year and there is only a faint hint of a seasonal cycle. The anomalies in the U component are again, in general agreement with those experienced at the surface (Figure 65). The climatology of the V component (Figure 80) shows a seasonal signal similar to what was observed at the surface, reaching approximately the same positive value (southward flow of around ~0.1 m.s^{-1}) during summer, but a negative value (northward flow of ~0.1 m.s^{-1}) that is much smaller in magnitude. This shows that water at the surface travels faster (and towards the north) during the summer months than it does at 200m deep. This is an indication that the Benguela current may be seasonal in its strength.

From these characteristics we can see that the climatological flow is a complex one. It should be noted that the range of the anomalies was, in most cases, much larger than the range of the climatologies. This shows that there is a large amount of variability in the U and V components. The reliability of the climatology can be questioned as it was calculated from only eight years of data. Some surprises emerged that are in contrast to what was previously known for this region. Nevertheless, certain characteristics that were expected were confirmed.

It was generally observed that the range of the seasonal cycle in the V component was larger than that in U component. This is most probably due to the barrier imposed by the subcontinent that caused most of the flow to be directed along the isobaths. The U component did however exhibit some seasonality at the locations close to the coast in the surface layers and to a lesser extent, at 200m. At the CCT, it was observed that the area less that 80km from the start of the transect showed a relatively strong onshore flow at the surface. This pattern is thought to be due to the nearby presence of Cape Columbine. The seasonal signal could be observed in the V component at all transects and at both depths. The northward flow at the surface was at its most intense during the summer months and slowed down during the winter months. At 200m deep, a positive V component (southward flow) was observed within 25km

of the shelf between January and July at the CPT and all through the year at CCT and ORET. This coincides with the observations of the poleward undercurrent. There was also a noticeable increase in the flow at the surface in the vicinity of the shelf break. This suggests that the topography may affect the U and V components throughout the water column in the model.

Figure 82 sums up the average flow pattern over 6 months at the surface, and at a depth of 200m. The summer average was calculated as being the average flow from November to April inclusive, while the winter average was calculated to be the average flow from May to October. The red vectors on the offshore edge of each transect are scale vectors indicating a speed of $0.2 m.s^{-1}$ and directed at an angle of 45° to both the eta and xi axes. This was done to ensure that the rotation of the axes was correctly applied when being superimposed on the background map. This image shows the circulation pattern as calculated by the numerical model. The stick vectors on the diagram show largely what is expected, both in terms of magnitude and direction, from the circulation of the area. A northward flow is observed over much of the region at both depths. A small amount of flow towards the southeast was observed at the offshore edge of the CPT during summer and at both depths. Though this particular area is about 4° north of where the Agulhas Retroflection is presumed to be, it may still be under the influence of this feature.

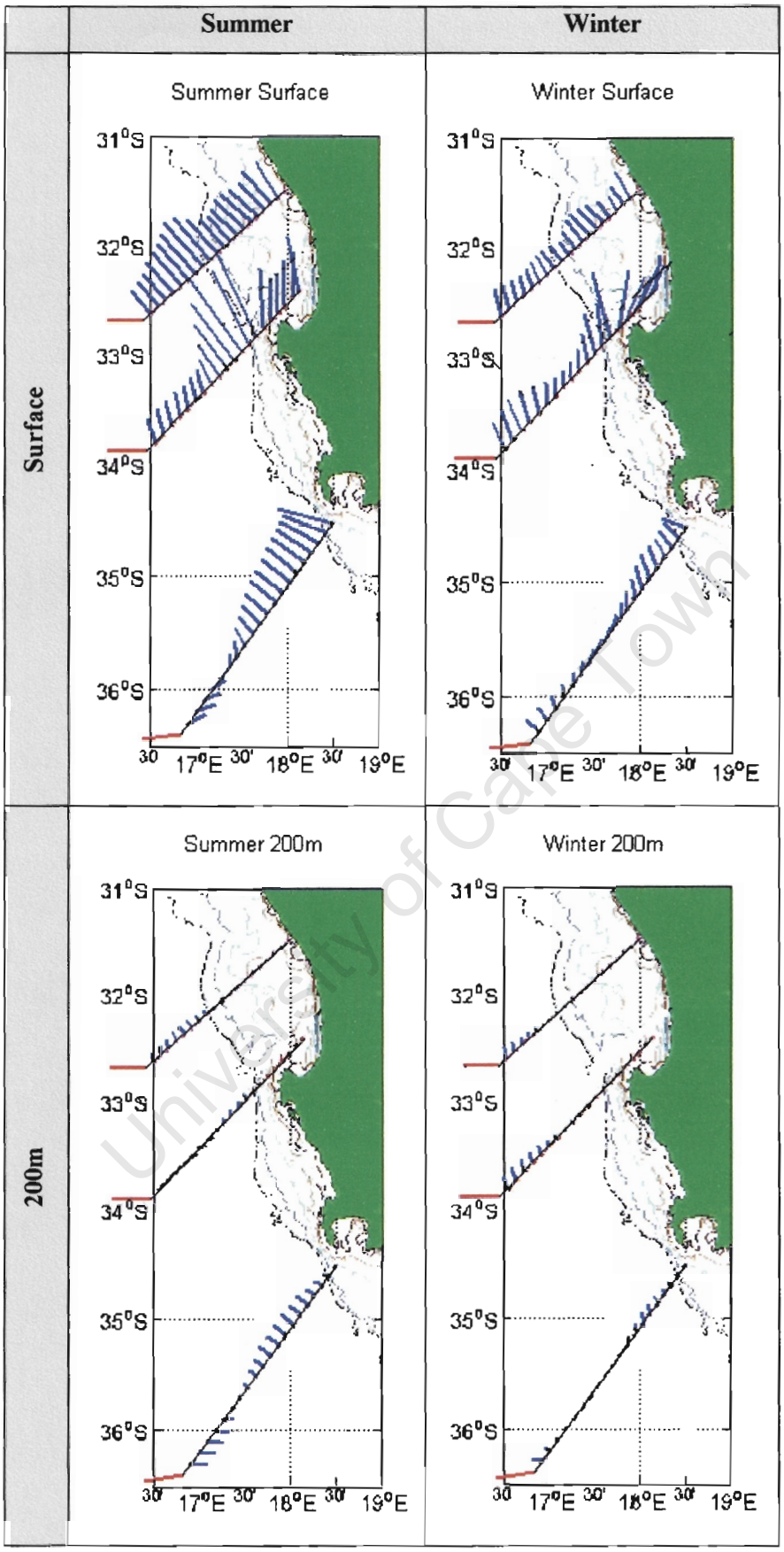

Figure 82: *Stick vector plots of the 6-month average flow patterns at the different transects.*

6.4 SUMMARY

This work has made an attempt to answer certain questions pertaining to the model. This section summarises how these questions were answered.

Upwelling does exist in the model, and can be easily seen from the Temperatures and Salinities. A mechanism has been identified that may drive the upwelling process, but it is difficult to isolate this as the major cause in the 3-dimensional situation. It was difficult to see Upwelling occur by looking directly at the U and V component climatologies. The vertical structure of Upwelling could however be seen by carefully looking at the climatology of the Temperature and Salinity data. A tabular summary of the structure was given in Tables 6 and 9. As Upwelling tends to cause a decrease in the vertical temperature gradient, an alternate method of comparing upwelling intensity is by looking at the difference between the mean temperature at the surface, and the mean temperature at 200m. In this manner, we have seen that the upwelling intensity is lowest at the CPT, and increases towards the north. This is in agreement with what is known about the Benguela Region.

The water circulation pattern is complex due to the high amount of variability. Figure 82 shows that intensity of the Benguela Current, is seasonal and reaches a peak during summer. In winter the average flow is slower and the onshore flow increases. The poleward undercurrent was previously observed in the Hovmuller plots of the V component at 200m and can be seen according to scale in Figure 82 in the vicinity of the shelf break.

7 REFERENCES

1. AGENBAG, J.J. (1992): A procedure for the computation of sea surface advection velocities from satellite thermal band imagery, with applications to the south east Atlantic Ocean. PhD Thesis. University of Cape Town, Cape Town.

2. ANDREWS, W.R.H., HUTCHINGS, L. (1980): Upwelling in the southern Benguela Current. *Progress in Oceanography Vol 9(1)*, pp81.

3. BAKUN, A, NELSON, C.S. (1991): The seasonal cycle of wind-stress curl in subtropical eastern boundary current regions. *Journal of Physical Oceanography, Vol 21.* Pp 1815-1834.

4. BANG, N.D., ANDREWS, W.R.H. (1974): Direct Current Measurements of a shelf-edge frontal jet in the southern Benguela System. *J. Mar. Res. 32(3)*, pp 405 – 417.

5. BARNIER, B, MARCHESIELLO, P, PIMENTA DE MIRANDA, A, MOLINES, J.M., COULIBALY A, (1998): A Sigma Coordinate primitive equation model for studying the South Atlantic. Part 1: Model configuration with error estimates. *Deep Sea Research, Vol 45*, pp 543-572.

6. BIASTOCH, A, KRAUß, W (1999): The Role of Mesoscale Eddies in the Source Regions of the Agulhas Current. *Journal of Physical Oceanography Vol 29*, pp 2303-2317.

7. BIRCH, G.F., ROGERS, J. (1973). The South African Shipping news and fishing industry review. Volume XXVIV, No 7, July.

8. BOYD, A.J. (1987): The Oceanography of the Namibian shelf. PhD Thesis. University of Cape Town, Cape Town.

9. BOYD, A.J., TAUNTON-CLARK, J, OBERHOLSTER, G.P.J. (1992): Spatial features of the near-surface and midwater circulation patterns off western and southern South Africa and their role in the life histories of various commercially fished species. *S. Afr. J. Mar. Sci 1.* pp 189 – 206.

10. BOYD, A.J., SHILLINGTON, F.A. (1994): Physical forcing and circulation patterns on the Agulhas Bank. *S. Afr. J. Mar. Sci. 90.* pp 114 – 122.

11. BOYD, A.J., OBERHOLSTER, G.P.J. (1994): Currents off the west and south coasts of South Africa. *S. Afr. Shipping News and Fishing Ind. Rev 49,* pp 26-28.

12. CHAPMAN, P., SHANNON, L.V. (1985): The Benguela ecosystem 2: Chemistry and related processes. *Oceanography and Marine Biology: An annual review 23.* University Press, Aberdeen, pp 183 – 251.

13. DA SILVA, A.M., YOUNG, C.C., LEVITUS, S. (1994):, Atlas of surface marine data 1994, Vol1: Algorithms and Procedures pp 74, NOAA, USA.

14. DE MIRANDA, A.P. (1995): Application d'un modèle numérique de circulation générale océanique permettant la generation de turbulence méso-échelle à l'étude de l'Atlantique Sud, Ph.D thesis. Université Joseph Fourier, France.

15. DUNCOMBE-RAE, C.M., SHILLINGTON, F.A., AGENBAG, J.J., TAUNTON-CLARK, J., GRÜNDLINGH, M.L. (1992): An Agulhas Ring in the South Atlantic Ocean and its interaction with the Benguela Upwelling Frontal System. *Deep-Sea Res. 39(11/12),* pp 2009 – 2027.

16. DURAND, M.H., CURY, P., MENDELSSOHN, R., ROY, C., BAKUN, A., PAULY, D. (1998): Global versus local changes in upwelling systems. Editions ORSTOM, Paris, pp 558.

17. GARZOLI, S.L., FORDON, A.L., PILLSBURY, D. (1994): BEST: Benguela Soure and Transport. *The South Atlantic: Present and Past Circulation, Bremen, Germany 15-19 August 1994,* Universität Bremen, Germany, pp 52 – 167.

18. GORDON, A.L., LUTJEHARMS, J.R.E., GRÜNDLINGH, M.L. (1987): Stratification and circulation at the Agulhas retroflection. *Deep-Sea Res. 34(4A)* pp 565 – 599.

19. GORDON, A.L., HAXBY, W.F. (1990): Agulhas eddies invade the South Atlantic: evidence from Geosat altimeter and shipboard. Conductivity-Temperature-Depth survey. *J. Geophys. Res 95(C3),* pp 3117 – 3125.

20. GORDON, A.L., WEISS, R.F., SMETHIE, W.M., WARNER, M.J. (1992): Thermocline and intermediate water communication between the South Atlantic and Indian Oceans. *Journal Geophys. Res. 97(C5)* pp 7223 – 7240.

21. GORDON, A.L., BOSLEY, K.T., AIKMAN, F. (1995): Tropical Atlantic Water within the Benguella Upwelling System at 27°S. *Deep-Sea Res. 42*, pp 1 – 12.

22. GUASTELLA, L.A-M. (1992): Sea surface heat exchange at St. Helena Bay and implicationd for the southern Benguela system. *S. Afr. J. Mar. Sci. 12,* pp 61 – 70.

23. HAIDVOGEL, D.B., ARANGO, H.G., HEDSTRÖM, K.S., BECKMANN, A., MALANOTTE-RIZZOLI, P., SHCHEPETKIN, A.F. (1991): Model Evaluation experiments in the North Atlantic Basin: Simulations in nonlinear terrain-following coordinates. *Dyn. Atm. Oceans, 32* pp 610 – 619.

24. HANEY, R.L. (1991): On the Pressure force over steep topography in sigma coordinate Ocean models. *Journal of Physical Oceanography Vol 21*, pp 610-619.

25. KLIEM, N., PIETRZAK, J.D. (1999): On the Pressure Gradient Error in sigma coordinate ocean models: A comparison with a laboratory experiment. *Journal of Geophysical Research*, Vol 104, pp 781-799.

26. LARGE, W.G., MCWILLIAMS, J.C., DONEY, S.C. (1994): Oceanic vertical mixing: a review and a model with a nonlocal boundary layer parameterization. *Rev. Geophys 32*, pp 323-403.

27. LARGIER, J.L., CHAPMAN, P., PETERSON, W.T., SWART, V.P. (1992): The western Agulhas Bank: Circulation, stratification, and ecology. *S. Afr. J. Mar. Sci. 12* pp 319 – 339.

28. LEVITUS, S. (1982): Professional Paper 13. *Climatological Atlas of the World Ocean*. Pp 173, NOAA, USA.

29. LUTJEHARMS, J.R.E., SHILLINGTON, F.A., DUNCOMBE-RAE, C.M. (1991): Observations of extreme upwelling filaments in the Southeast Atlantic Ocean. *Science 253(5021),* pp 774 – 776.

30. MARCHESIELLO, P., MCWILLIAMS, J.C., SHCHEPETKIN, A. (2000): Open boundary conditions for long-term integration of regional oceanic models. *Ocean Modelling*.

31. MOROSHKIN, K.V., BUBNOV, V.A., BULATOV, R.P. (1970): Water circulation in the eastern South Atlantic Ocean. *Oceanology 10(1)*, pp 27 – 34.

32. NELSON, G., HUTCHINGS, L. (1983): The Benguela Upwelling Area. *Progress in Oceanography, Vol12* pp 333-356, Pergamon Press.

33. NELSON, G. (1985): Notes on the physical Oceanography of the Cape Peninsula upwelling system. *South African Ocean Colour and Upwelling Experiment*, Sea Fisheries Research Institute, Cape Town, pp 63 - 95.

34. NELSON, G. (1989): Poleward motion in the Benguela area. *Poleward flows along Eastern Ocean boundaries*, Springer-Verlag, New York, pp 110 – 130.

35. NELSON, G. (1991): An equatorward jet west of Cape Town. *Abstract IAPSO Proceedings XX Assembly Vienna 1991*, pp 189.

36. OLSON, D.B., EVANS, R.H. (1986): Rings of the Agulhas Current. *Deep-Sea Res. 33(1A)*, pp 27 – 42.

37. PALMA, E.D., MATANO, R.P. (1998): On the implementation of passive open boundary conditions for a general circulation model: The barotropic mode. *Journal of Geophysical Research 103*, pp 1319 – 1341.

38. PEDLOSKY, J. (1987): Geophysical Fluid Dynamics 2nd Edition. Springer-Verlag, New York.

39. PENDUFF, T. (1998): Ètude de la dynamique de l'Atlantique Nord-Est à l'aide d'un modèle numérique regional, Ph.D thesis. Université de Bretagne Occidentale, France.

40. PENVEN, P. (2001): A numerical study of the Southern Benguela circulation with an application to fish recruitment. PhD Thesis. University of Bretagne, France.

41. POND, S., PICKARD, G.L. (1983): Introductory Dynamical Oceanography 2nd Edition. Pergamon Press, Oxford.

42. PRESTON-WHYTE, R.A., TYSON, P.D. (1988): The Atmosphere and Weather of Southern Africa. Oxford University Press, Cape Town, pp 375.

43. RAYMOND, W.H., KUO, H.L. (1984): A Radiation boundary condition for multi-dimensional flows. *Quart. J.R. Met. Soc. 110* , pp 535 – 551.

44. REID, J.L. (1989): On the total geostrophic circulation of the North Atlantic Ocean: Flow Patterns, tracers and transports. *Prog. Oceanogr 33*, pp 1 – 92.

45. SHCHEPETKIN, A.F., MCWILLIAMS, J.C. (1998): Quasi-monotone advection schemes based on explicit locally adaptive dissipation. *Monthly Weather Reviews 126* pp 1541 – 1580.

46. SHANNON, L.V. (1966): Hydrology of the south and west coasts of South Africa. *Investl Rep Div Sea Fish S. Afr 58* Cape Town.

47. SHANNON, L.V., NELSON, G., JURY, M.R. (1981): Hydrological and meteorological aspects of upwelling in the southern Benguela Current. *Washington DC; Coastal and Estuarine Sciences. 1: Coastal Upwelling,* American Geophysical Union, Washington DC, pp 146 – 159.

48. SHANNON, L.V., ANDERSON, F.P. (1982): Applications of satellite ocean colour imagery in the study of the Benguela Current System. *S. Afr. J. Photogramm Remote Sens. Cartogr. 13(3)* pp 153-169.

49. SHANNON, L.V. (1985), The Benguela Ecosystem. 1: Evolution of the Benguela, physical features and processes. *Oceanography and Marine Biology, An Annual Review 23.* Aberdeen, University Press, pp 105 – 182.

50. SHANNON, L.V., HUNTER, D. (1988): Notes on Antartic Intermediate Water around southern Africa. *S. Afr. Jour, Mar. Sci 6* pp 107 – 117.

51. SHANNON, L.V., AGENBAG, J.J., WALKER, N.D., LUTJEHARMS, J.R.E. (1990): A major perturbation in the Agulhas retroflection area in 1986. *Deep-Sea Res. 37(3)*, pp 493 – 512.

52. SHANNON, L.V., NELSON, G. (1996): The Benguela: Large Scale Features and Processes and System Variability. *The South Atlantic: Present and Past Circulation*. Springer-Verlag, Berlin Heidelberg, pp 163-210.

53. SHELTON, P.A., HUTCHINGS, L. (1982): Transport of Anchovy, *Engraulis capensis* Gilchrist, eggs and early larvae by frontal jet current. *J. Cons. Perm. Int, Explor. Mer. 40*, pp 185 – 198.

54. SHILLINGTON, F.A., PETERSON, W.T., HUTCHINGS, L., PROBYN, T.A., WALDRON, H.N., AGENBAG, J.J. (1990): A cool upwelling filament off Namibia, southwest Africa: preliminary measurements of physical and biological properties. *Deep-Sea Res. 37(11A)*, pp 1753 – 1772.

55. SHILLINGTON, F.A. (1998): The Benguela Upwelling System off southwestern Africa. *The Sea Vol 10.* Wiley and Sons, New York.

56. SIEFRIDT, L. (1994): Validation des données de vent ERS-1 et des flux de surface du CEPMMT dans le contexte de la modélisation des circulations océaniques à l'échelle d'un basin, Ph.D thesis. Université Joseph Fourier, France.

57. SIESSER, W.G., SCRUTTON, R.A., SIMPSON, E.S.W. (1974): *The Geology of Continental Margins*. Springer-Verlag: pp 641-654.

58. SKOGEN, M.D. (1998): Numerical modelling of the Benguela System: Some preliminary results. *Tech. Rep.*, pp 17, Institute of Marine Research, Norway.

59. SONG, Y. (1998): A general pressure gradient formulation for ocean models. Part 1: Scheme design and diagnostic analysis. *Monthly Weather Reviews 126*, pp 2313-3230.

60. SONG, Y., HAIDVOGEL, D. (1994): A Semi-implicit ocean circulation model using a generalized topography-following coordinate system *Journal Comp. Physics Vol 115*, pp 228 – 244.

61. STRAMMA, L., PETERSON, R.G. (1989): Geostrophic Transport in the Benguela Current Region. *J. Phys. Oceanogr 19,* pp 1440 – 1448.

62. TYSON, P.D.(1986): Climate Change and Variability in Southern Africa. Cape Town; Oxford University Press.

63. VALENTINE, H.R., LUTJEHARMS, J.R.E., BRUNDRIT, G.B. (1993): The water masses and volumetry of the South Agulhas Current Region. *Deep-Sea Res. 40(6).* Pp1285 – 1305.

64. VAN BALLEGOOYEN, C., GRÜNDLINGH, M.L., LUTJEHARMS, J.R.E. (1994): Eddy fluxes of heat and salt from the south west Indian Ocean into the southeast Atlantic Ocean: A case study. *J. Geophys. Res. 99(C7),* pp 14053 – 14070.

65. VAN FOREEST, D., BRUNDRIT, G.B. (1982): A two-mode numerical model with an application to Coastal Upwelling. *Progress in Oceanography, Vol 11* pp 329-392, Pergamon Press.

8 APPENDIX A: LIST OF VARIABLES

#	Variable Short Name	Variable Long Name	Units of Measurement
1	ntimes	Number of Long Timesteps	N/A
2	ndtfast	Number of Short Timesteps	N/A
3	dt	Size of long Timesteps	seconds
4	dstart	Time Stamp assigned to model initialisation	days
5	nhis	Number of timesteps between history records	N/A
6	nrst	Number of timesteps between restart records	N/A
7	ntsavg	Starting timestep for accumulation of time-averaged fields	N/A
8	navg	Number of timesteps between time-averaged records	N/A
9	tnu2	Laplacian mixing coefficient for tracers	m^2s^{-1}
10	visc2	Laplacian mixing coefficient for momentum	m^2s^{-1}
11	Akt_bak	Background vertical mixing coefficient for tracers	m^2s^{-1}
12	Akv_bak	Background vertical mixing coefficient for momentum	m^2s^{-1}
13	rdrg	Linear drag coefficient	$m.s^{-1}$
14	rdrg2	Quadratic drag coefficient	N/A
15	Zo	Bottom roughness	metres
16	Znudg	Free-surface nudging/relaxation inverse time scale	day^{-1}
17	M2nudg	2D momentum nudging/relaxation inverse time scale	day^{-1}
18	M3nudg	3D momentum nudging/relaxation inverse time scale	day^{-1}
19	Tnudg	Tracers nudging/relaxation inverse time scale	day^{-1}
20	rho0	Mean density used in Bousinnesq approximation	$kg.m^{-3}$
21	gamma2	Slipperiness parameter	N/A
22	spherical	Grid Type logical switch	N/A
23	xl	Domain length in Xi-direction	metres
24	el	Domain length in Eta-direction	metres
25	theta_s	S-coordinate surface control parameter	N/A
26	theta_b	S-coordinate bottom control parameter	N/A
27	Tcline	S-coordinate surface/bottom layer width	metres
28	hc	S-coordinate parameter, critical depth	metres
29	sc_r	S-coordinate at Rho-points	N/A
30	sc_w	S-coordinate at W-points	N/A
31	Cs_r	S-coordinate stretching curves at Rho-points	N/A
32	Cs_w	S-coordinate stretching curves at W-points	N/A
33	Lev	Output Levels	N/A
34	z_r	Depth at Rho-points	metres
35	h	Bathymetry at Rho-points	metres
36	f	Coriolis parameter at Rho-points	$seconds^{-1}$
37	pm	Curvilinear coordinate metric in Xi	$metres^{-1}$
38	pn	Curvilinear coordinate metric in Eta	m^{-1}
39	lon_rho	Longitude of Rho-points	°E
40	lat_rho	Latitude of Rho-points	°N
41	angle	Angle between Xi-axis and East	radians
42	mask_rho	Mask on Rho-points	N/A
43	mask_u	Mask on U-points	N/A

(Continued on next page)

(Continued from previous page)

#	Variable Short Name	Variable Long Name	Units of Measurement
44	mask_v	Mask on V-points	N/A
45	mask_psi	Mask on Psi-points	N/A
46	Znudgcof	Nudging coefficients for SSH	$second^{-1}$
47	Tnudgcof_temp	Nudging coefficients for temperature	$second^{-1}$
48	Tnudgcof_salt	Nudging coefficients for salinity	$second^{-1}$
49	visc2_r	Laplacian mixing coefficients for momentum	m^2s^{-1}
50	visc2_p	Laplacian mixing coefficients for momentum	m^2s^{-1}
51	diff2_temp	Laplacian mixing coefficients for temperature	m^2s^{-1}
52	diff2_salt	Laplacian mixing coefficients for salinity	m^2s^{-1}
53	ocean_time	Time since initialisation	seconds
54	zeta	Free-surface	metre
55	ubar	Vertically integrated u-momentum component	$m.s^{-1}$
56	vbar	Vertically integrated v-momentum component	$m.s^{-1}$
57	u	U velocity component	$m.s^{-1}$
58	v	V velocity component	$m.s^{-1}$
59	w	Vertical velocity component	$m.s^{-1}$
60	omega	S-coordinate vertical momentum component	m^3s^{-1}
61	temp	Potential temperature	Celsius
62	salt	Salinity	PSU
63	Hsbl	Depth of oceanic surface boundary layer	m
64	AKv	Vertical viscosity coefficient	m^2s^{-1}
65	AKt	Temperature vertical diffusion coefficient	m^2s^{-1}
66	AKs	Salinity vertical diffusion coefficient	m^2s^{-1}
67	shflux	Surface net heat flux	$Watts.m^{-2}$
68	swrad	Solar shortwave radiation flux	$Watts.m^{-2}$
69	sustr	Surface u-momentum stress	$N.m^{-2}$
70	svstr	Surface v-momentum stress	$N.m^{-2}$
71	dtfast	Size of short time-steps	seconds

Table 12: *Details of variables saved as output from the Plume Model*

9 APPENDIX B: GLOSSARY

9.1 MODEL CONFIGURATION

Bousinnesq Approximation

It approximates that the changes in density are very small when compared to the actual value of the density. ie $\Delta\rho << \rho$, therefore $\Delta\rho+\rho\approx\rho$

Hydrostatic Approximation

The water pressure on a given horizontal surface in the ocean is essentially equal to the weight of the water above that surface divided by the area of the surface.

Dynamic Pressure

The strict definition of dynamic pressure (p_d) is: $p_d = \frac{1}{2} \rho v^2$. It is the pressure caused by the movement of a fluid of density ρ, at a velocity v.

Forcing terms

Any external terms that force a change in a variable over time.

Dissipation Terms

Terms to account for the loss of a variable over time as it changes form. Eg: The transformation of kinetic energy to heat energy can be seen as a dissipation of kinetic energy.

Turbulent Mixing Coefficients

The Constant coefficients that govern the way mixing processes w.r.t turbulence at a specific velocity occur.

Equation of Continuity

For an incompressible fluid, the equation of continuity states that the volume enclosed in the domain must remain constant.

Finite Differences

In a finite-difference model, there is not an attempt to find the solutions of a particular variable at *any* point in the model domain, but rather to find values on a grid of points that are a given distance from a point where the solution is known.

First Radius of Deformation (Rossby Deformation Radius)

It's algebraic definition occurs in the application of the Burger Number, and is the distance over which the gravitational tendency to render a free surface flat is balanced by the tendency of the Coriolis acceleration to deform the free surface

Land/Sea Masking Technique

A technique that allows the model to distinguish between gridpoints that fall in the ocean from those that fall on land.

Arakawa C Grid

The horizontal discretisation scheme is the staggered Arakawa C grid. It refers to the face that all variables are not defined at the same point, but are staggered w.r.t. the locations at which they are defined.

Aliasing

Aliasing occurs when the nature of a signal is distorted due to an error in the sampling frequency.

Truncation Error

This error is defined as the difference between the true analytical solution and the solution that is derived by numerical calculation

Turbulent Cascades

The large-scale motion in the atmosphere and oceans contain a broad spectrum of turbulent motions that are fed to a considerable extent by the energy of the largest-scale flows. The turbulent fluctuations, embedded in the larger flow, tend to drain the large-scale flow of energy by a variety of mechanical processes and pass the energy to finer scales of motion. Thus the energy cascades into finer and finer scales.

Richardson Number

It is a useful number to help determine whether density variations would enhance or reduce turbulence.

Double Diffusion

Even though a water column may be statically stable, instability may occur due to the fact that heat and salt diffuse at different rates. So even if two water masses are of the same density but with different combinations of temperature and salinity, the double diffusion of these two properties may render the layers unstable.

9.2 METHODOLOGY

NetCDF

The Network Common Data Format (NetCDF) is a machine-independent format for representing arrays of data.

Free Surface

Models where the surface layer is allowed to deform and distort under stresses. This type of model is in contrast to the rigid lid approximations that do not allow any kind of distorting at the surface.

Momentum Components

Strictly defined, the component of momentum of an object in any direction is the product of the mass of that object and the velocity that it is travelling. For this study, object being studied is a volume of seawater of unit mass.

Vertically Integrated Momentum Components

The Vertically Integrated Momentum Components in any particular direction is given by the sum of the momentum components of that particular direction throughout the water column.

Surface Momentum Stresses

The Surface Momentum Stress is the amount of Force being transferred into the model at the surface due to the action of atmospheric dynamics (wind).

Climatology

The climatology of a variable (such as temperature) can be viewed as the average value of that variable taken over a certain period of time. In this work, what is referred to as "climatology" is actually the yearly climatology over a 2 day averaging interval, taken from 8 years of data.

Anomaly

The Anomaly of a variable at a particular time is the difference between the climatology at that time and the in-situ value of the variable.

Spline Interpolation Method

The cubic spline interpolation method is constructed using piecewise third-order polynomials which pass through the given datapoints.